IS-T--1559

DE91 016161

Experimental Studies of Long-range Atomic H Motion and Desorption in Hydrogenated Amorphous Silicon and Germanium

by

Wu, Xiao-Lin

PHD Thesis submitted to Iowa State University

Ames Laboratory, U.S. DOE

Iowa State University

Ames, Iowa 50011

Date Transmitted: July 11, 1991

PREPARED FOR THE U.S. DEPARTMENT OF ENERGY

UNDER CONTRACT NO. W-7405-Eng-82.

DISCLAIMER

This report has been reproduced directly from the best available copy.

AVAILABILITY:

To DOE and DOE contractors: Office of Scientific and Technical Information
P.O. Box 62
Oak Ridge, TN 37831

prices available from: (615) 576-8401
FTS: 626-8401

To the public: National Technical Information Service
U.S. Department of Commerce
5285 Port Royal Road
Springfield, VA 22161

Experimental studies of long-range atomic H motion and desorption in hydrogenated amorphous silicon and germanium

Xiao-Lin Wu*

Under the supervision of Joseph Shinar
From the Department of Physics and Astronomy
Iowa State University

Long-range H motion and desorption in low hydrogen concentration undoped hydrogenated amorphous silicon (a-Si:H) and germanium (a-Ge:H) was studied by deuterium secondary ion mass spectrometry (SIMS) depth profiles and IR absorption of a-Si:H/a-Si:(H,D)/a-Si:H and a-Ge:H/a-Ge:(H,D)/a-Ge:H. SIMS monitors deuterium motion (assumed similar to that of H), while IR yields information on hydrogen content and bonding. The diffusion constant was found to be dispersive with time, and depended on H content C_H, diffusion length L, and microvoid content, at temperatures $T \leq 400$ °C for a-Si:H and $T \leq 310$ °C for a-Ge:H. It exhibited a power-law $D(t) = D_{oo}(\omega t)^{-\alpha}$ relation in both systems. In a-Si:H, α generally deviates from the $1 - T/T_o$ dependence on the temperature T expected from a multiple trapping mechanism. The diffusion constant at constant diffusion length $D(t_L)$ then deviates from an Arrhenius dependence on the temperature. The "apparent" activation energy E_a and prefactor D_o, defined by the linear

---

* DOE Report IS-T-1559. This work was performed under contract No. W-7405-Eng-82 with the U.S. Department of Energy.

best-fit of $\ln D(t_L)$ vs $1/T$, strongly increase with L at low C_H. The Meyer-Neldel relation (MNR) $D_o = A_{oo}\exp(E_a/T_o')$, where $A_{oo} \simeq 3.1\times10^{-14}$ cm^2/s and $T_o' \simeq 730$ K, holds for all $1.3 \leq E_a \leq 2.4$ eV and $2.5\times10^{-5} \leq D_o \leq 3100$ cm^2/s.

In a-Ge:H, α is essentially temperature and composition independent, but increases with microvoid content. The activation energy E_a ranges from 0.7 to 1.2 eV among the various films. The Meyer-Neldel relation is observed, with $A_{oo} \simeq 5.5\times10^{-16}$ cm^2/s and $T_o' \simeq 530$ K. These values are lower than the corresponging values in a-Si:H. Hydrogen desorption temperature is as low as 180 °C. Yet the significance of the MNR is questionable in both a-Si:H and a-Ge:H.

The diffusion results for both a-Si:H and a-Ge:H are discussed in relation to the microstructure of the films. The nature of the microvoid-induced deep H-trapping sites is also discussed. Finally, a possible relation between the dispersive diffusion and a percolation model is presented.

TABLE OF CONTENTS

I. INTRODUCTION

A. Research Motivation

Research on amorphous semiconductors has drawn considerable attention over the last two decades. Among them, hydrogenated amorphous silicon (a-Si:H) and its alloys have been the subject of intensive studies due to their applications as opto-electronic materials.

The most important aspect of semiconductors is their "structure-sensitive" nature. Specifically, the introduction of dopant atoms of the order of ppm into a rigid crystalline network produces excess free carries (holes or electrons, depending on the doping elements), thus enabling p-n control of the conduction process in the material. On the other hand, in amorphous semiconductors, efforts to control the Fermi energy from near the conduction-band-mobility edge to near the valence band by doping were not successful until 1975, when n- and p- type doping was demonstrated in glow discharge a-Si:H by Spear and LeComber at the university of Dundee.[1] Prior to this breakthrough, it was generally believed that disordered systems such as amorphous semiconductors could not be doped, since the local valency requirements could be satisfied by bond rearrangements.[2,3] This crucial discovery of valency controllability opened up a wide variety of potential applications of amorphous semiconductors in electronics and

opto-electronics. Carlson and Wronski demonstrated the first application by fabricating an a-Si:H solar cell in 1976.[4] Some unique physical properties and remarkable advantages of a-Si:H alloys as new opto-electronic materials emerged:

(a) High optical absorption and large photoconductivity in the visible region. Unlike crystalline Si, which has an indirect bandgap, the gap of a-Si:H (and microcrystalline Si (μc-Si:H)) is effectively direct. It has been shown[5] that the absorption coefficients of a-Si:H and μc-Si:H are more than one order of magnitude larger than that of a single crystal silicon near the maximum solar photon energy region of 5000 Å. Moreover, a-Si:H has excellent photoconductivity in the visible photon energy region. The ratio of photoconductivity to dark conductivity σ_{ph}/σ_d is 10^5 to 10^7, and σ_d is of the order of 10^{-9} to 10^{-11} $(\Omega\ cm)^{-1}$.

(b) The existence of valency electron controllability: Another noticeable property of these tetrahedrally bonded hydrogenated amorphous semiconductors is that the valence electron can be controlled by doping of the substitutional impurity atoms.

(c) Low cost material: A systematic calculation based upon the opto-electronic properties of various solar cell materials indicated[6] that the optimum thickness of the active layer in a-Si solar cells is much smaller than the corresponding thickness in single-crystal silicon solar cells.

(d) Due to its amorphous structure, large area cell can be deposited on various substrate materials at relatively low temperatures (200 to 300 °C). Moreover, because a-Si:H can be deposited directly from a vapor phase growth onto noncrystalline sustrates, mass production of large area solar cell and fabrication of large thin film transistor arrays is possible.

In light of these advantages, intensive research led to impressive progress in the basic scientific understanding of the materials as well as film growth technology and device fabrication processing. Applications spread to photosensors, imaging devices, photoreceptors, and thin film transistor arrays.

The motivation for studying hydrogenated amorphous germanium (a-Ge:H) is that the optical energy gap of a-Si:H is too large for the significant low-energy portion of the solar spectrum. This led to the development of tandem-type amorphous solar cells consisting of a-Si:H and a-$Si_{1-x}Ge_x$:H. It has generally been reported that the overall opto-electronic properties of a-$Si_{1-x}Ge_x$ are inferior to those of optimized films of a-Si:H. Such poor behavior, however, is not unique to a-$Si_{1-x}Ge_x$:H alloys, and has been reported for other alloys, such as a-$Si_{1-x}C_x$:H[7] and a-$Si_{1-x}Sn_x$:H.[8] W. Paul et al.[9] reported a preference ratio in excess of 5 for the attachment of H to Si over Ge during the formation of such alloys. It thus

appears that a higher density of defect states is associated with Ge. Indeed, Electron spin resonance results show that the ratio of Ge dangling bonds to Ge atoms increases drastically with increasing Ge percentage.[10] However, if this was the source of the inferior properties, then the predicted magnitudes of the photoconductivity and the photoluminescence would be much smaller in a-Ge:H than the actual experimental results obtained by von Roedern.[11] Paul et al.[9,11] suggested the existence of weakly bonded hydrogen in a-Ge:H and in a-$Si_{1-x}Ge_x$ alloys with a high Ge content, which could perturb the film structure resulting in a heterostructure responsible for the observed properties.

Many problems remain to be solved, such as the optimal conditions for producing good a-$Si_{1-x}Ge_x$:H. a-Ge:H in particular needs to be studied more throughly since it does not involve problems such as preferential attachments, which plague the a-$Si_{1-x}Ge_x$:H system.

B. Spatial and Electronic Structure of Tetrahedrally Bonded Amorphous Semiconductors

In crystalline materials, it is justified to assume a periodic potential because of the periodic positioning of the atoms. Bloch's theorem and appropriate boundary conditions yield the allowed energies for electrons in a given potential. This yields energy bands E(**k**) where **k** is the electronic wave vector. The concept of periodicity of atoms is thus vital to

this property. In crystalline semiconductors, bands of allowed energies are thus separated by forbidden energy gaps. In amorphous materials, however, the periodic lattice as well as the reciprocal lattice are lost. Thus, the wave vector **k** is no longer a good quantum number.

Although the long-range periodicity is lost in amorphous semiconductors, a high degree of short-range order (SRO) is retained due to the chemical bonding. Hence, the nearest neighbor separation, i.e., bond lengths, are nearly equal, as in the corresponding crystalline case. The bond angles, on the other hand, suffer a variation of about 10%.

Extensive macroscopic observations as well as microscopic structural characterizations of a-Si:H have been made by many groups in the past ten years. These included X-ray diffraction,[12] small-angle neutron scattering,[13] TEM (morphology),[14], infrared absorption (bonded hydrogen),[15] proton NMR (spatial distribution of hydrogen),[16] Raman-scattering spectroscopy (local structural order),[17] and ESR (defect spin density).[18]

X-ray and neutron diffraction,[19,20] have been used to determine the radial distribution function (RDF) J(r), which is widely used to characterize these materials. Defined as

$$J(r) = 4\pi r^2 \rho(r) \qquad 1.1$$

where $\rho(r)$ is the atomic density at distance r from an

arbitrarily chosen atom, it is deduced from the Fourier transforms of the diffraction data and gives the one-dimensional description of the atomic distribution. From the results of Temkin et al.,[20] shown in Fig. 1.1, the following conclusions can be drawn. The width of the first peak in the amorphous solid is evidently very similar to that of the crystalline case. Since the peak width corresponds to the spread in nearest neighbor distance, the bonding interactions responsible must be nearly identical. In both cases, the coordination number, $z = 4$, is determined by integrating the area under the first peak. Furthermore, the second nearest neighbor coordination is retained in the amorphous case but the absence of long-range order is obvious since the peaks beyond the second nearest neighbor are very broad and overlapping. The difference in the width and area under the peak indicates a bond angle distribution width of about 10°, or about a 10% variation in bond angles around 109.5°, the crystalline tetrahedral bond angle. The variation in bond lengths, on the other hands, is usually about 1 to 2%. Hence, in amorphous tetrahedral semiconductors, although the number of atoms associated with the nearest neighbors are the same, there is nevertheless a variation in the bond angles that rapidly leads to a loss of medium range order and ultimately to the absence of long range order.

The structure can thus be described as a continuous

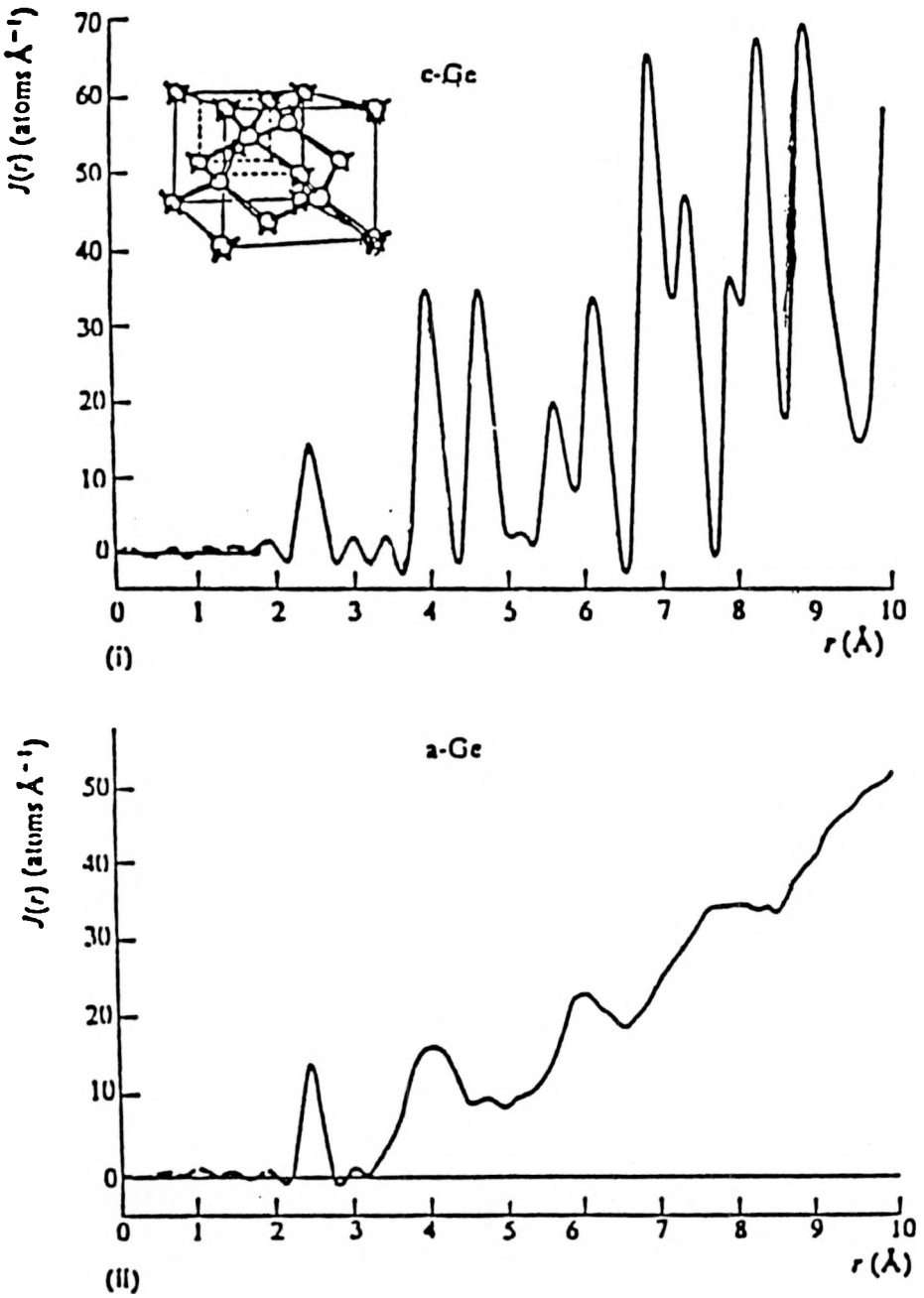

Fig. 1.1 X-ray derived RDFs for (a) crystalline Ge (with inset of diamond lattice, and (b) amorphous Ge films (from Ref. 20)

random network (CRN) appropriate to the structure of covalent type materials. A model built by Polk[21] first demonstrated the possibility of building an expanded CRN with the coordination number z = 4 without developing excessive bond length strain but allowing for a spread in bond length (~ 1%) can lead to a smaller bond angle distortion (± 7%). The small increase in bond length distortion energy can be compensated by a large decrease in bond angle distribution energy. The spatial fluctuations cause the conduction and valence bands to extend into the band gap region giving rise to the tail states, the extent of which depends upon the amount of inherent disorder. Fig. 1.2 is an illustration of a CRN.

The absence of periodicity in amorphous materials dictates that there can be no reciprocal space. In this case, electron states cannot be described by a band structure of the form $E(\mathbf{k})$. The quantity still valid as a description of electron states for both crystalline and amorphous solids is the density of states (DOS) N(E), which is defined as the number of electron states per unit volume in the energy range E to E+dE. Both theoretical calculations and experimental data have demonstrated the existence of band gaps which are analogous to those of crystalline semiconductors, though they are less well defined. Typical experimental techniques are photoemission, visible optical absorption and photoconductivity measurements. Several important

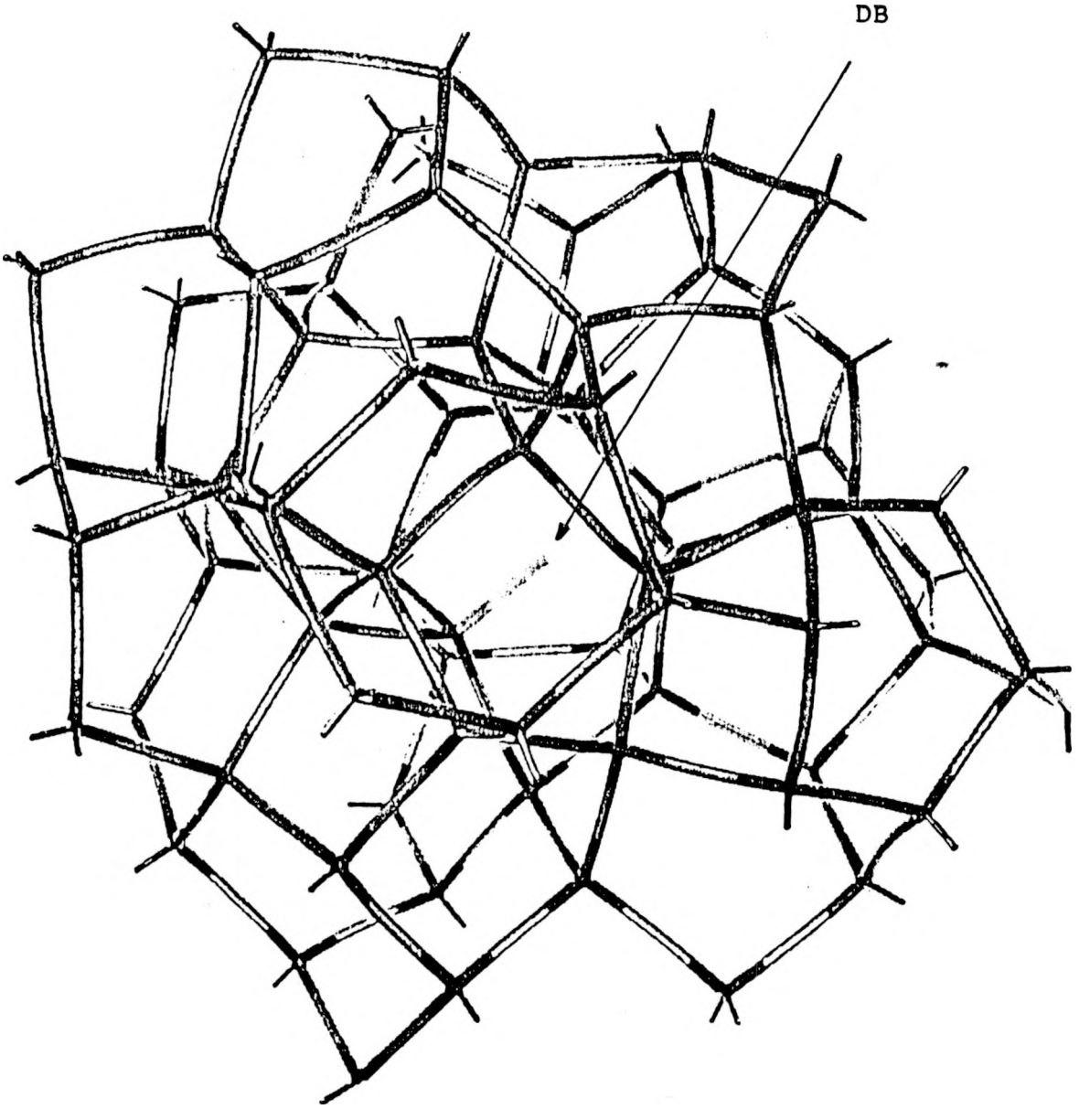

Fig. 1.2 A continuous random network (CRN) model of amorphous Ge (or Si) containing a dangling bond

consequences of disorder are worth mentioning. As depicted in Fig. 1.3,[22] in the crystalline solids, the electron states are spatially extended throughout the sample as the result of the periodic potential. In the amorphous case, due to disorder, they are spatially confined or localized in the vicinity of a single atomic site ("Anderson localization", see ref. 22). Mott[23] suggested that the states remain localized up to a precise energy E_c, the "mobility edge", beyond which they are extended and approximately similar to Bloch states. The mobility gap is then defined as the difference in energy between the mobility edges of the valence and conduction bands.

C. Defects and Hydrogen Passivation

Unlike other amorphous materials, tetrahedrally bonded amorphous semiconductors can not be formed by quenching from the liquid. However, they can be prepared in the form of thin films deposited on a substrate, usually from chemical vapor or sputter deposition. The films are thus grown under non-equilibrium conditions and are therefore metastable. This fact, combined with the rigidity of the tetrahedral bonding which tolerates only limited bond-length and bond-angle deviations, leads to the formation of a large number of structural defects. The simplest possible defect that would be present is the isolated dangling bond, which is simply a

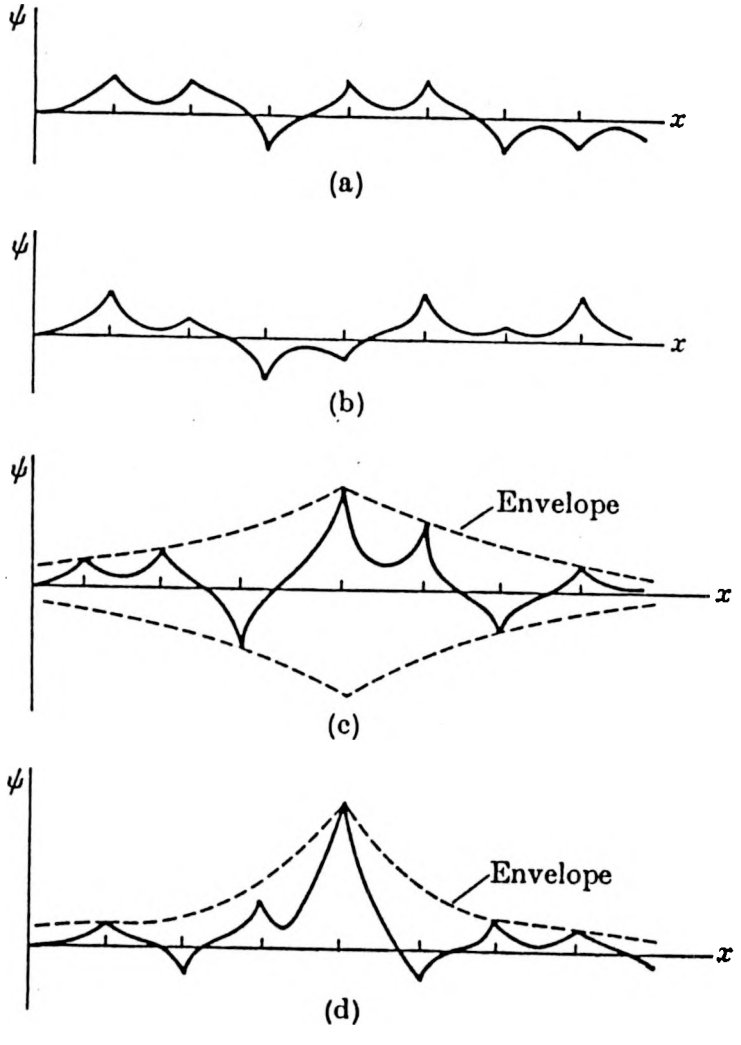

Fig. 1.3 Form of the wavefunction in the Anderson localization model: (a) non-localized states; (b) barely non-localized ($E \geq E_c$); (c) barely localized ($E \leq E_c$); (d) strong localization (from Ref. 22)

three-fold coordinated Si or Ge atom with an unpaired orbital. The energy levels of these states may be discussed in terms of a simple molecular orbital picture. In Si, the four outer shell electrons have an atomic electronic configuration of $3s^2 3p^2$. These four atomic levels hybridize to form four sp^3 molecular hybrids. The interaction between Si atoms splits them into bonding (lower energy) orbitals and antibonding (higher energy) orbitals. The solid state interactions then broaden these molecular levels into bands separated by a band gap, as shown in Fig. 1.4. A dangling bond, or non-bonding orbital, containing a single electron, will reside neither in bonding nor in antibonding energy levels. Instead, the energy state corresponding to this sp^3 orbital lies approximately midway between the conduction and valence bands. Thus, dangling bonds are expected to introduce electron states deep in the gap, which is otherwise empty. Hence a dangling bond is a sp^3 orbital resulting from an undercoordinated atom. The resulting density of states is shown in Fig. 1.5. The dangling bond states are denoted by T_3^C, where T represents tetrahedral bonding, the subscript denotes coordination number and the superscript C the charge state. The three charge states are 0, and ±1. T_3° has one electron in its orbital. Since this electron is not paired, it has an ESR signal with g = 2.0055. Unhydrogenated amorphous Si and Ge exhibit large ESR signals (10^{19}-10^{20} cm^{-3}). The large magnitude of densities

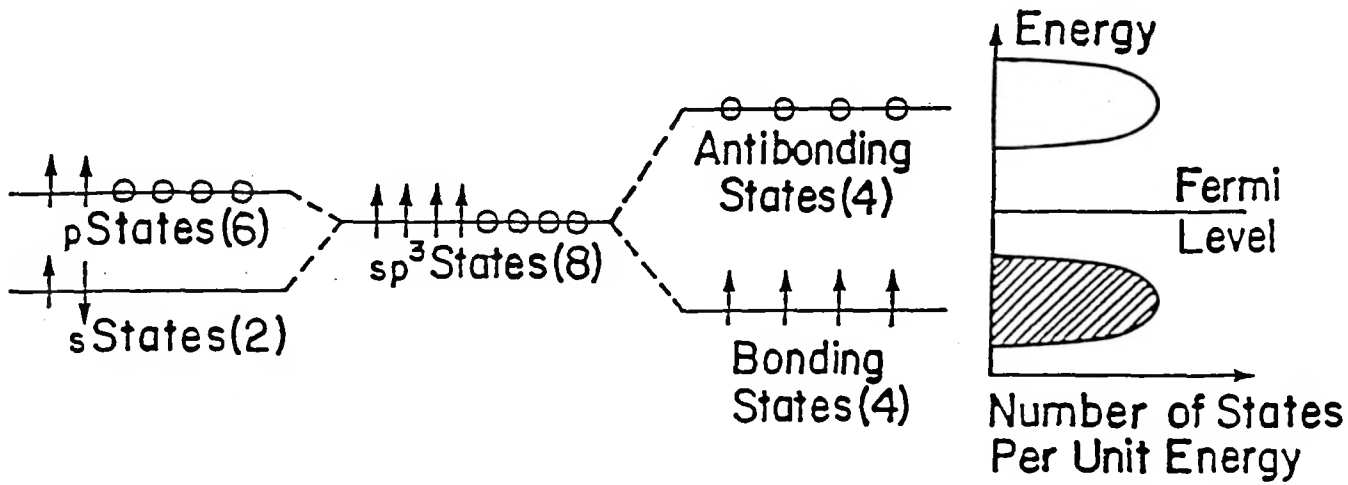

Fig. 1.4 On the right is the electronic structure of silicon as determined by a band model. On the left is the electronic structure of silicon as determined by nearest neighbor bonds (from Ref. 72)

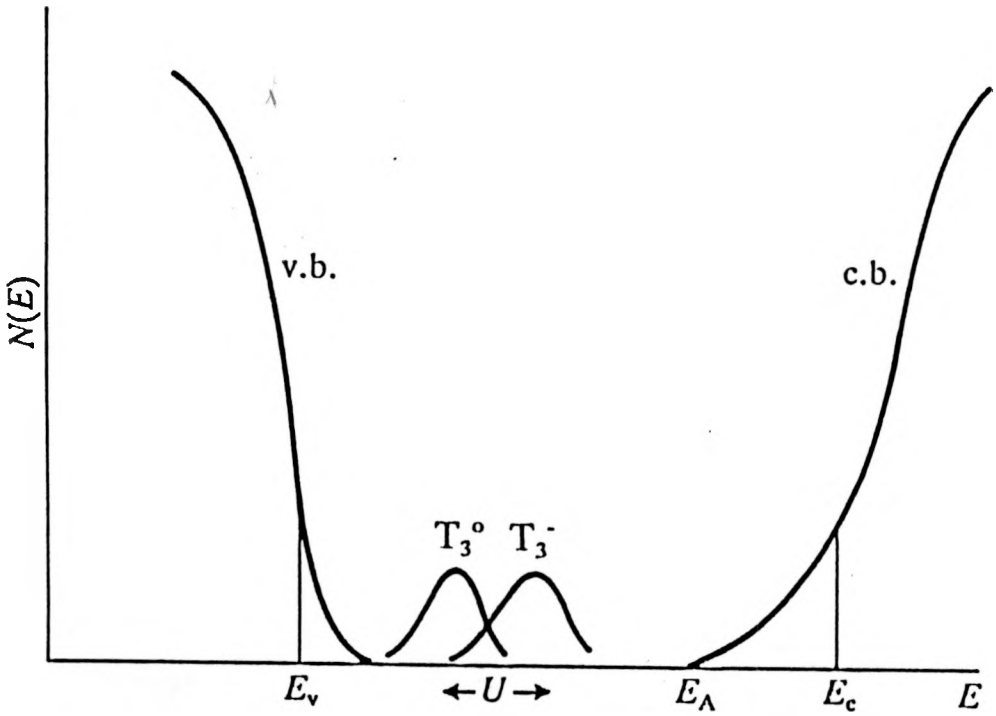

Fig. 1.5 Schematic density of states in amorphous silicon or germanium. E_c, E_v are the mobility edges in the conduction band (c.b.) and valence band (v.b.), respectively, E_A is the bottom of the conduction band, and T_3°, T_3^- are dangling bond states for the first and second electron to occupy the state (from Ref. 22)

of gap states in these samples explains the observation that they cannot be doped. A dopant atom will donate (or accept) an electron to (or from) the defect gap states. But the high density of states prevent the Fermi level E_F from shifting significantly, and thus they cannot be doped. The charged dangling bonds $T_3^{\pm}$ are double occupied or empty and can not be detected by ESR. Since the energy needed to add the second electron, called the correlation energy U, is positive,[24] the T_3^- state is located higher in energy than T_3°. The T_3^+ state has no electron in its orbital, and is in principle at the same energy level as T_3°. There exist some controversies on the exact locations of dangling bond states and the polarity of the correlation energy U.[25,26] Only the fraction of dangling bonds that are neutral can be detected by ESR, and they depend on the position of the Fermi level E_F, which shifts toward the gap center as more dangling bonds are created.

Some native defects in a-Si:H have been suggested, such as weak Si-Si bonds,[27] charged under-coordinated Si atoms (T_3^+, T_3^-) with negative correlation energy,[25,28] and the five-fold over-coordinated Si "floating bond".[29,30]

In the "floating bond" model, Pantelides[29,30] suggested that an over-coordinated Si atom is just as likely a candidate for a defect in the amorphous network as an under-coordinated Si atom (dangling bond). Since the central atom has only four

valence electrons to be shared in bonds with five nearest neighbors, the missing electron can be thought of as "floating" among the five bond sites (i.e. the wave function is distributed over five sp^3 hybrids). By analogy with the dangling bond, he called this state a "floating bond" (FB). When it is neutral, this state has an electron and is thus ESR active. Using the previous nomenclature, floating bonds are denoted as T_5°.

Although experimental evidence favors dangling bonds, the identification of the dominant defect in a-Si:H as 'dangling bond (DB)' or 'floating bond (FB)' is not entirely established. ESR hyperfine[31,32] and electron-nuclear double resonance (ENDOR)[33] studies have been interpreted both as a DB with backbond weakening[31] or a FB with significant localization on one of the atoms.[32,33] Recently, Stutzmann and Biegelsen[34] found that the underlying defect wave function is mostly localized on one Si atom and has almost pure p character. Hence the g = 2.0055 defect is incompatible with FB, since calculations[35,36] show that an FB wave function has much less weight on any Si atom than DB state.

By using concepts from crystal defect physics such as equilibrium defect densities and defect formation energies, we may gain some insight about DB and FB. If they are mutually independent, their densities will depend exponentially on the formation energy. Hence, a few kT less in associated

formation energy will lead to drastic changes in the density. If they are created in pairs, however, their densities would obviously be equal, following the analogy of vacancy/interstitial pairs (Frenkel defects). Several theoretical calculations have been published. Biswas, Grest, and Soukoulis[37] reported the generation of generally equal numbers of FB and DB from their molecular dynamics simulation of amorphous silicon prepared by quenching liquid silicon. Pantelides[38] suggested formation energies of 0.6 eV and 0.8 eV for FB and DB, respectively. Kelires and Tersoff[39] simulated a-Si, formed by rapid quenching of the liquid, and obtained mean formation energies of 0.3 eV and 0.6 eV, respectively.

The electrical, optical and opto-electronic properties of amorphous semiconductors are greatly improved upon incorporation of hydrogen. The incorporated H atoms terminate dangling bonds (hydrogen passivation), and relieve strains by breaking weak Si-Si bonds to form stronger Si-H bonds. They thus drastically reduce the defect state density at midgap and the density of conduction and valence band tail states. This reduction in the density of midgap states is manifest by a sharp drop in the ESR signal.[40] Since these states are the dominant carrier recombination-trapping centers, their elimination leads to a remarkable improvement of the opto-electronic properties.[41] The incorproation of hydrogen also reduces the disorder of the network and results in both an

increase of the optical bandgap (1.4 to 2.0 eV for a-Si:H, 0.9 to 1.2 eV for a-Ge:H), and a decrease of the Urbach tail energy E_o.[42,43] Since the number of electronically active defect gap states is drastically reduced, a-Si:H can be doped p-type or n-type via incorporation of group III or group V elements.

D. Stability and Hydrogen Motion

Stability is one of the most important issues in the physics and technology of a-Si:H. Reversible light induced metastable defect generation, known as the Staebler-Wronski effect (SWE), was discovered in 1977. They observed that both the photoconductivity and dark conductivity decreased following intense illumination of a thin film of a-Si:H at room temperature. They noticed that the effect could be completely removed by annealing the film above 150 °C.[44] Obviously, this light-induced creation of defects limits the usefulness of a-Si:H in solar cells. Since then additional metastable changes in other properties of a-Si:H have been observed, such as luminescence,[45] electron spin resonance,[46,47] gap state density,[48] and sub-gap absorption.[49] The changes in charge carrier trapping and recombination kinetics due to light exposure have been interpreted as the results of metastable changes in the density or occupancy of the defect states near mid-gap. The

metastable effects in a-Si:H apparently are all closely related. Furthermore, these metastable defect changes can be induced by means other than illumination, such as charge injection,[50] doping,[51] electron bombardment,[52] X-rays[53] and thermal generation.[54] It thus appears that the metastable defects are generated during the recombination of carriers rather than by photogeneration.[55] Experiments on the stability of a-$Si_{1-x}Ge_x$:H by Nakamura et al.[56] show that the Staebler-Wronski effect is relatively small in that system. However, the density of photo-induced states is similar to that in a-Si:H. They suggest that the large density of states created by Ge dangling bonds masks the light-induced defect generation process.

There is general agreement that the density of deep gap states increases with light soaking and the Fermi level moves toward the gap center. Also, their ESR signature is the same as that of DB. However, significant disagreement still exists on the types, densities and energies of these light-induced defects. Despite many efforts, the nature of the metastable defect remains to be established.

The incorporation of hydrogen leads to many beneficial effects, as we discussed above. However, hydrogen motion has been suggested to be related to metastable defect generation and annealing. Two popular models for the generation of metastable defects are briefly outlined in the following.

In the charge redistribution model by Adler,[57,58] different kinds of Si dangling bonds are formed when a-Si:H is made. During illumination, the defects convert from one type to the other: electrons trapped by T_3^+ centers convert T_3^+ into T_3° and holes trapped by T_3^- centers convert T_3^- into T_3° centers. Hence, the population of all the dangling bonds is redistributed due to the redistribution of charges. The concentration of T_3° increases, while that of T_3^+ and T_3^- decreases. In other words, the number of T_3° dangling bonds increases without the need to break any bonds. Hydrogen may be needed to lower the energy barriers hindering interconversion, but its presence is otherwise not essential.

In the second model,[45,59] weak Si-Si bonds are associated with the bonding states in the valence band tail and the antibonding states in the conduction band tail. When an electron is trapped in the antibonding tail state and recombines with a hole in the bonding tail state, the released energy may break the weak bond into two dangling bonds. A hydrogen is needed to stablize the new defects, and prevent them from repairing.

Moreover, Jackson[60] proposed a hydrogen motion model to account for the metastable effects in a-Si:H. He points out that, through dangling bond creation and destruction reactions, many metastable phenomena may either directly relate to hydrogen motion or the equilibration of the lattice

induced by hydrogen motion. The equilibrium defect and dopant density is governed by an equilibrium between these reactions both during growth and as a function of time. These reactions are the driving forces for hydrogen to diffuse through the material. It is suggested that the properties of hydrogenated amorphous silicon slowly change as the hydrogen finds lower and lower energy configurations in the network.

Hydrogen diffusion in a-Si:H has been characterized by a time-dependent dispersive diffusion constant $D_H(t)$.[61,62,63] $D_H(t)$ can be expressed as

$$D_H(t) = D_{oo}(\omega t)^{-\alpha} \qquad 1.2$$

where D_{oo} is the microscopic diffusion constant, ω is the attempt frequency, and α is the dispersion parameter. The "hydrogen glass" model, proposed by the Xerox group,[62,64,65] suggests that α is related to the annealing temperature T as

$$\alpha = 1 - T/T_o \qquad 1.3$$

where kT_o is the characteristic energy of the exponential distribution of multiple trapping (MT) sites, i.e., the density $N_H(E)$ of H trapping sites with barrier E is

$$N_H(E) = N_{Ho}\exp(-E/kT_o). \qquad 1.4$$

The MT model has been highly successful in explaining electronic transport phenomena in disordered systems, where the transport is dominated by frequent trapping into, and thermal release from, localized states.

Experimental evidence exists that the carrier-induced defect creation and dispersive H motion may be related. The Xerox group[62,66] found that excess band-tail carriers exhibit a characteristic "stretched-exponential" decay, according to the relation

$$N(t) = N(0)\exp[\ -(t/\tau)^{\beta}\ ] \qquad 1.5$$

where ß is the dispersion parameter. Equation 1.5 is the solution of rate equation

$$dN/dt = -\nu N \qquad 1.6$$

provided that $\nu \propto t^{-\alpha}$. This is thus the direct result of the dispersive diffusion with α related to ß as

$$\beta = 1 - \alpha = T/T_{o} \qquad 1.7$$

Another effect of hydrogen motion is desorption. The desorption and diffusion processes limit the thermal stability of hydrogen in a-Si:H and a-Ge:H, and further limit the stability of the devices made from these materials. It is thus important to study the mechanisms governing the release

of hydrogen from the amorphous network at elevated temperatures.

E. Scope of Thesis Work

H motion and desorption in rf sputter-deposited a-Si:H and a-Ge:H were investigated in this research. Infrared absorption was used to monitor the hydrogen bonding configuration and the Si- and Ge- bonded H content. Secondary ion mass spectrometry was used to obtain the depth profiles used to determine H diffusion. ESR and optical transmission were also used for sample characterization.

a-Si:H/a-Si:(H,D)/a-Si:H multilayers, prepared by rf sputtering, of varying H content and microstructure, and a glow discharge sample, were annealed at temperatures ranging from 270 to 400 °C. a-Ge:H/a-Ge:(H,D)/a-Ge:H multilayers with different hydrogen concentration were similarly prepared by rf sputtering and annealed at temperatures ranging from 180 to 310 °C. The Meyer-Neldel relation (MNR) between the prefactor D_o and the activation energy E_a, $D_o = A_{oo}\exp(E_a/kT_o')$, was observed for both systems. Yet the significance of the MNR is questionable, and probably results simply from the exponential form of the Arrhenius relation, and the limited temperature range of the measurements. Influence of structural relaxation processes and the microvoid-related deep H-trapping sites on H motion is discussed. The percolation model, which yields the

anomolous diffusion from a geometrical point of view, is also discussed.

II. SAMPLE PREPARATION

The samples studied in this work were thin films prepared by reactive radio frequency (rf) sputtering except for sample B, which was prepared by the glow-discharge (gd) process**. The amorphous silicon and germanium films were prepared in two sputtering systems. Schematic diagrams of the systems are shown in Figs. 2.1 and 2.2, respectively. Deposition of a thin film by rf sputtering is accomplished by bombarding a target of the material to be deposited with energetic (up to several keV) ions of an inert gas (Argon in this study). The inert gas is ionized and accelerated towards the target by the applied electric field. The ions then strike the target surface and knock out atoms of the target. These atoms then travel across the vacuum and deposit on a substrate.

a-Si:H/a-Si:(H,D)/a-Si:H multilayers 1 - 2 μm thick are deposited by either glow-discharge (gd) under standard conditions yielding device-quality films,[67] or by rf sputtering (sp) a Si target onto nominally unheated grounded substrates below the target. The target is a 6" diameter polycrystalline silicon disk, mounted on a water cooled stainless steel backplate located underneath the top plate of the chamber. Single crystal silicon wafer substrates are used

---

** The glow discharge film was prepared by R. F. Girvan at the Microelectronics Research Center, Iowa State University, Ames, Iowa 50011.

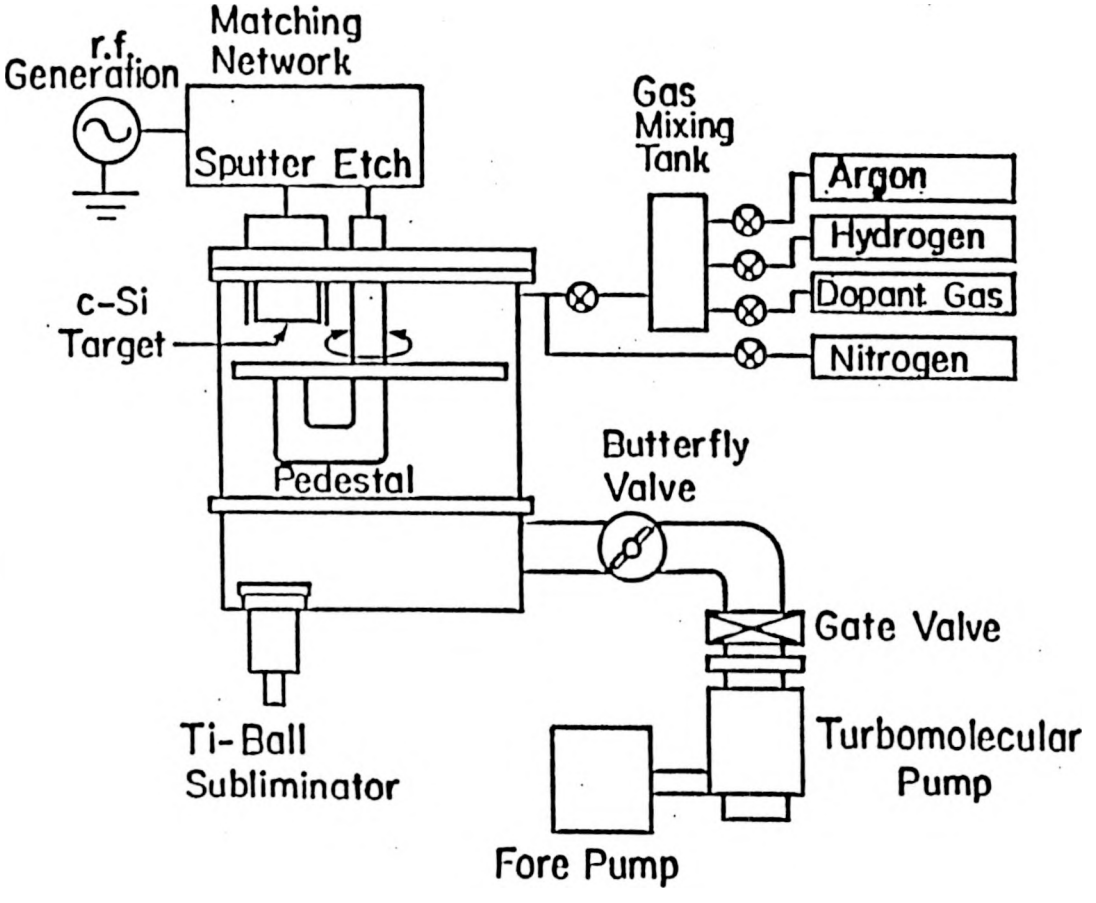

Fig. 2.1 Schematic diagram of the rf sputtering system used for deposition of a-Si:H

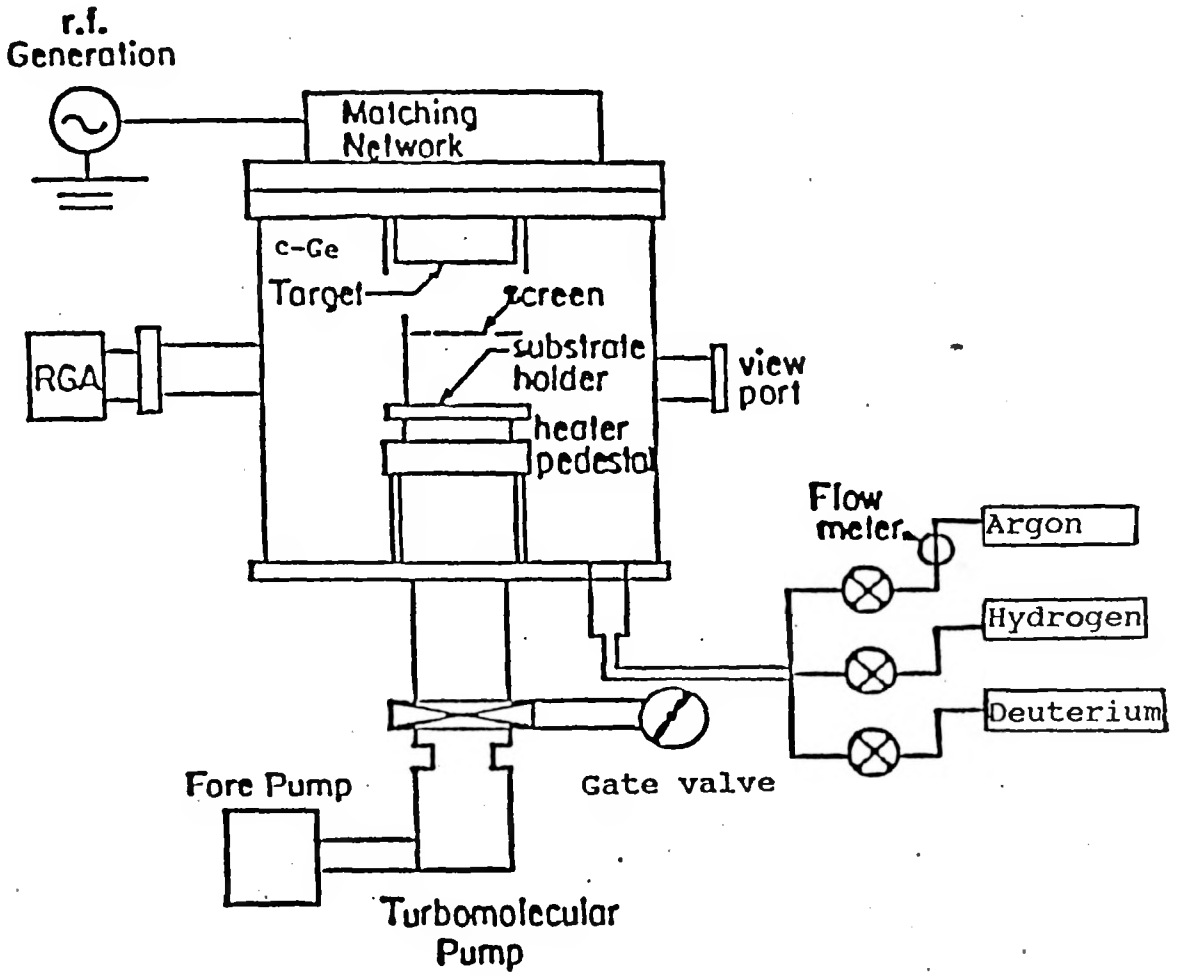

Fig. 2.2 Schematic diagram of the rf sputtering system used for deposition of a-Ge:H

for IR absorption and SIMS measurement, while Corning 7059 glass substrates are used for optical and ESR measurements. The rf power was from 100 to 550 W. The samples were annealed in evacuated pyrex tubes in the temperature range from 270 up to 400 °C. The target to substrate distance of the a-Si:H system was generally set at 1.25". The base vacuum pressure prior to film deposition was about $(3\pm1)\times10^{-7}$ torr. The gate valve is open to three turns to slow down the pumping rate. The gases are introduced according to their partial pressures. The gas of least partial pressure is introduced first while that with the highest partial pressure the last. The flow rates are controlled by micrometer valves. This chamber has a rotatable pedestal, which enables pre-sputter cleaning of the target.

The a-Ge:H/a-Ge:(H,D)/a-Ge:H multilayers studied in this work were all prepared by rf sp of a 6" diameter Ge target, onto nominally unheated grounded substrates located 3" below the target. The rf power is 300 W. The partial H_2 pressure vary from 0.1 to 1.5 mtorr, while the partial pressure of Argon is 8 mtorr during deposition of all of the films. The base pressure was $(4\pm1)\times10^{-7}$ torr, and the target-to-substrate distance was set to 3". Also, the chamber was equipped with an Ametek residual gas analyzer (RGA), which is used for monitoring the system vacuum and for thermal desorption measurements. The effective temperature at the film surface

during deposition is estimated to be ~ 100 °C. The samples were annealed in evacuated pyrex tubes in the temperature range from 180 up to 310 °C.

The sample structure of the multilayer a-Si:H (or a-Ge:H) and the corresponding ideal Deuterium SIMS depth profile is shown in Fig. 2.3. The top, middle and bottom layers were of equal thickness. The middle layer was deposited with up to 20% (partial pressure of hydrogen) deuterium added to the mix of hydrogen and Argon, which gave a deuterium concentration of no more than a few percent. It served as a probe for SIMS depth profiles. The D level was kept low to avoid perturbation of the microstructure and the IR spectra. Experimental evidence shows that this substitution does not significantly change the bonding configuration of the amorphous silicon film.[68] The differences between the diffusion of deuterium and hydrogen due to their mass ($m_D/m_H=2$) are negligible, and the diffusion mechanisms for them are expected to be identical, therefore the diffusion coefficients for deuterium and hydrogen are equivalent. Once the desired gas flow rates and pressures were achieved, an rf power, which is capacitively coupled to the target surface, is applied to the target and the grounded substrate holder. Charged particles are generated and accelerated and become more energetic in the induced field. Furthermore, these charged particles collide with other gas atoms, thus more atoms become

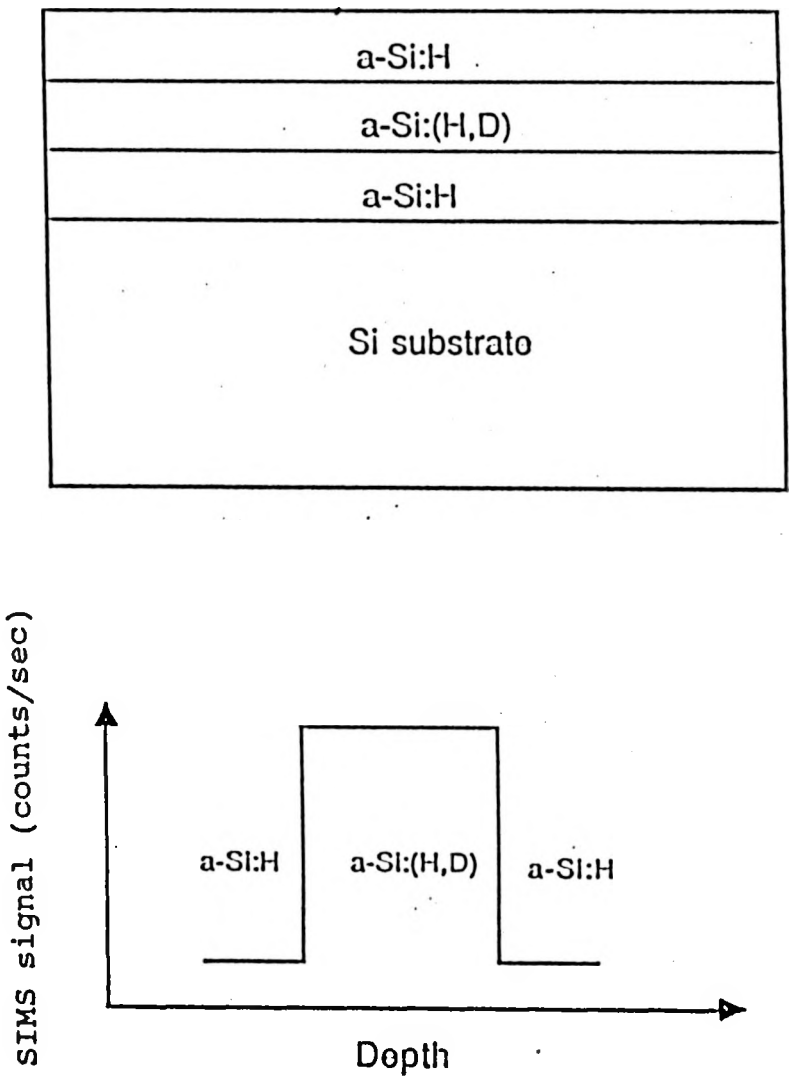

Fig. 2.3 Schematic illustration of the multilayer structure of the a-Si:H sample and the corresponding ideal Deuterium SIMS depth profile of an as-deposited sample

ionized. This process continues until a plasma is generated and sustained.

Figure 2.4 is a schematic diagram of the applied r.f. voltage and the effective target voltage. Instead of the actual sinusoidal waveform, a square wave is used here to simplify the discussion. During each positive half-cycle, the target attracts the electrons in the plasma. The target's positive potential is then effectively reduced as the electrons impinge on it. During the negative half-cycle, the positive ions are attracted to the target to reduce the negative bias voltage. However, since the mobility of electrons is much higher than that of ions in the plasma due to their great mass difference, more electrons than ions are attracted to the target surface in their respective half-cycle. As a result, an over-all negative self-bias $-V_{SB}$ is generated at the target and the plasma potential, V_p, is more positive than the potential of any electrode in contact with the plasma, due to the depletion of negative ions in the plasma near the positively biased electrode, as shown in the effective potential vs. distance relation (Fig. 2.5). Thus, after some time, the energetic positive ions are essentially attracted from the "glow region" of the plasma, and then accelerated passing the "dark region" to bombard the target surface by the negative bias potential rather than the rf potential. The ejected material from the target is then

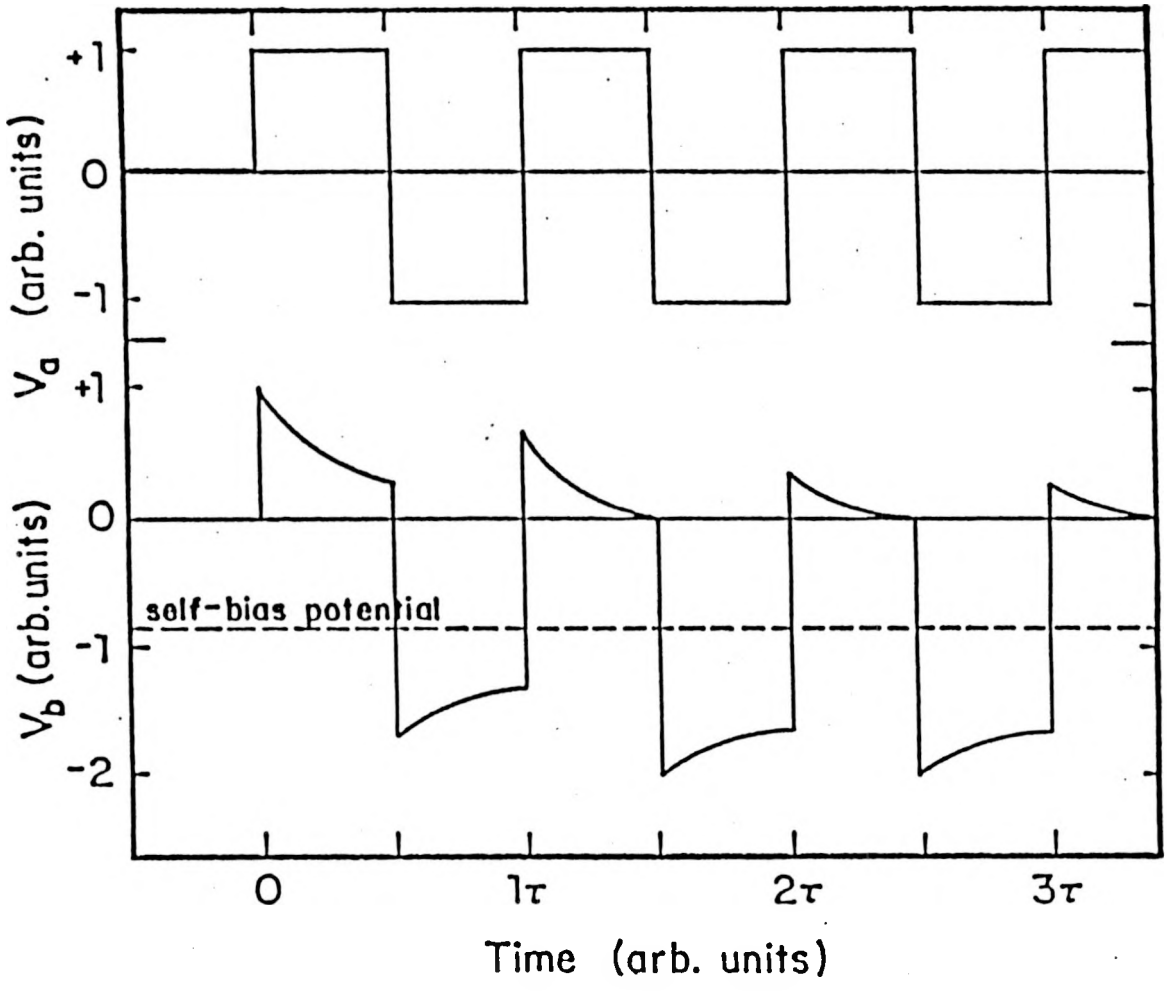

Fig. 2.4 Voltage vs time characteristics for the source, V_a, and the target, V_b, in an rf sputtering system. The period of the voltage source is τ (from Ref. 74)

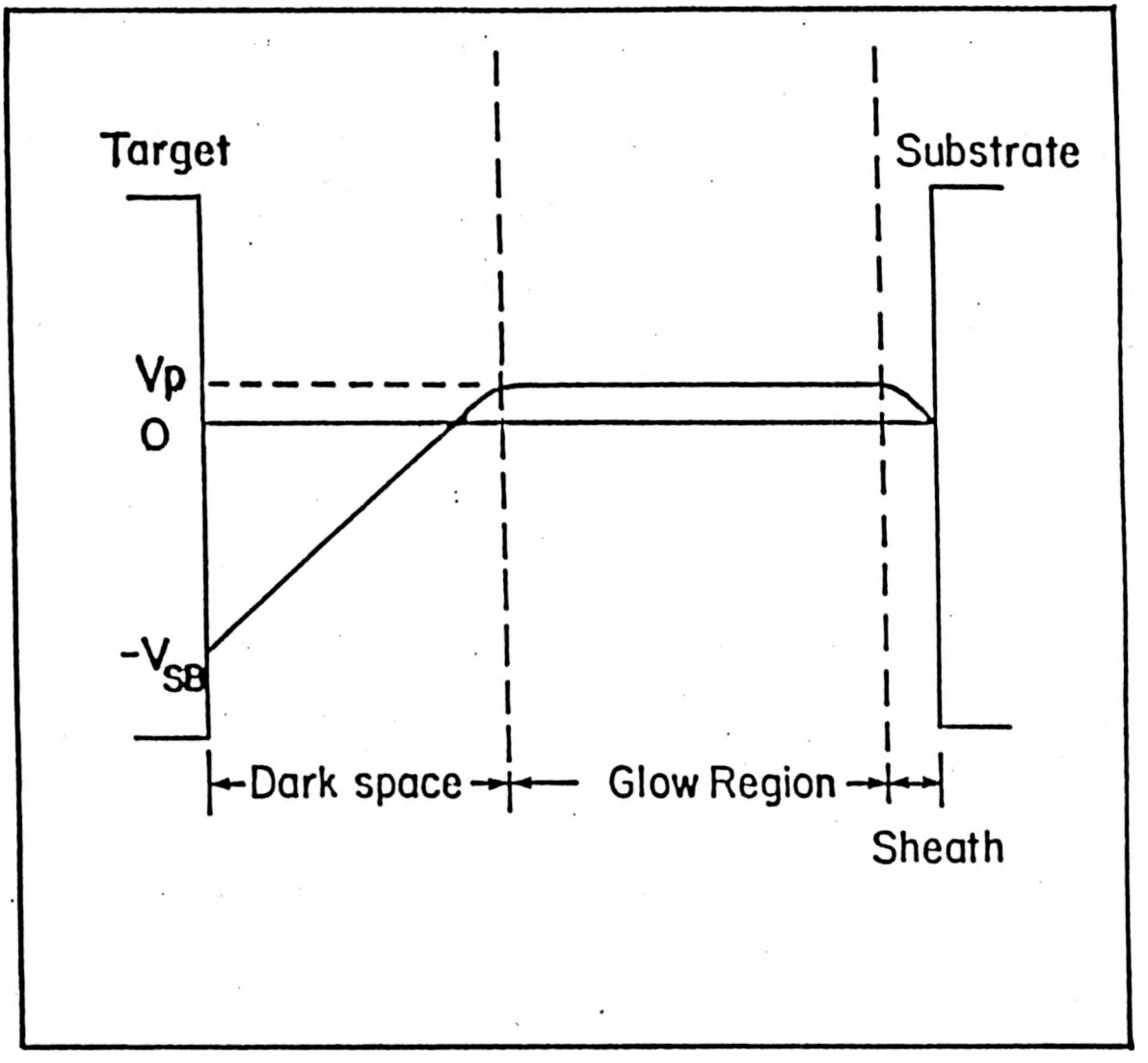

Fig. 2.5 Schematic diagram of the voltage distribution in an rf sputtering process. V_p is the sheath voltage between the plasma and substrate, and V_{sb} is the self-bias which is responsible for the sputtering of the target (from Ref. 74)

deposited on the substrate. Hydrogen introduced during the sputtering chemically reacts with the target material on the growing surface of the film, resulting in 'reactive' sputtering.

Voids and microstructure in sputtered films depend on the deposition conditions. Substrate temperature, gas partial pressure, sputtering power, and target-substrate distance are all significant parameters.

Before discussing these parameters, a brief treatment of the "thermalization" concept is useful. During the sputtering process, the majority of the particles have relatively low energy of a few volts. Yet some high energy (up to the incident ion energy) particles are present in the plasma. The bombardment by these energetic particles creates defects and thus degrades the film properties. Thermalization reduces the energy of the sputtered atoms before they reach the substrate, hence eliminating excessive bombardment and the defects they induce. From kinetic gas theory, the distance needed for the sputtered Si atoms to be thermalized before reaching the substrate, D_{th}, is given by[69]

$$D_{th}\ (cm) = P_{Ar}^{-1}\ 5.7\ \ln(E_i/E_t) \qquad 2.1$$

where P_{Ar} is the partial pressure of Argon (in mtorr), E_i is the initial energy of the sputtered atom, while E_t is the gas

thermal energy (kT). For a-Ge:H, eq. 2.1 becomes[70]

$$D_{th}\ (cm) = P_{Ar}^{-1}\ 8.1\ \ln(E_i/E_t). \qquad 2.2$$

For example, assuming E_t = 0.032 eV (substrate temperature ≈ 100 °C), and P_{Ar} = 10 mtorr, Si atoms of up to 1000 eV thermalize within a distance of 5.9 cm (2.3"). For Ge atoms, this distance is 8.4 cm (3.3").

Some deposition parameters were varied in order to study the dependence of hydrogen motion and desorption in a-Si:H and a-Ge:H on H content and film microstructure. The parameters were chosen to be near previously reported optimal conditions.

The Argon partial pressure used for a-Si:H sputtering was constant at 10 mtorr. Moustakas reported that higher pressure causes columnar morphology and microvoids.[71] For a-Ge:H, a partial pressure of 8 mtorr was used. This parameter has a direct impact on thermalization and thus should be considered when determining the target-to-substrate distance.

The hydrogen concentration can be changed by controlling the H_2 partial pressure in the plasma. A kinematic model for the incorporation of hydrogen in rf sputtered deposited a-Si:H was proposed by Moustakas et al.[72] They showed that under the assumptions that (a) there are no gas phase reactions between Si and H, (b) hydrogen incorporation arises from surface reactions only, and (c) there is no significant desorption of

bonded H, the hydrogen concentration in the film C_H is given by

$$C_H = C_{Hmax} [1 - \exp(-F\varphi\sigma/R)] \qquad 2.3$$

where C_{Hmax} is the maximum possible hydrogen concentration, F is the flux of hydrogen onto the film, φ is the sticking coefficient, σ is the capture cross section of the bonding sites for hydrogen, and R is the deposition rate of the growing film. From this relation, C_H would be expected to be a sensitive function of hydrogen flux, which is directly related to the hydrogen partial pressure. For a-Ge:H, considering that the mass is heavier and the bonding with H is weaker, the relation between hydrogen concentration and the sample preparation parameters may be different.

Increasing substrate temperature T_s usually produces denser amorphous films[73], a decrease of the internal stress, and a reduction of the ESR signal. During sputtering, the substrate is also heated by the bombardment of charged particles, such as Ar^+, H^+ and electrons.

III. SAMPLE CHARACTERIZATION

Many techniques have been used to characterize the electrical, optical and structural properties of amorphous semiconductors. Since hydrogen diffusion and its influence on the stability of the samples were our major concerns, the following standard characterization techniques were employed.

A. Thickness Measurements

A Sloan Dektak stylus profilometer (accuracy ± 1000 A) was used to measure the sample thickness. Corning glass substrates which are partially masked during the sputtering were used for this measurement.

B. Optical Measurements

In order to determine the optical band gap width and the absorption characteristics of the samples, a Cary model 14A spectrophotometer was used to measure the optical density in the 300 to 2,000 nm photon wavelength range. The Cary Spectrophotometer is a dual beam instrument. An incident beam of intensity I_o passes through the reference compartment while the transmitted light with intensity I travels through the sample compartment. The width of the entrance slits of these compartments is automatically adjusted to balance the intensities of the two exiting beams. The ratio of the two

slit widths gives the ratio of I_o to I. The optical density (O.D.) is defined as

$$O.D. = \log_{10}\left(\frac{I_o}{I}\right) . \qquad 3.1$$

The optical absorption coefficient α is defined as

$$I=I_o\exp(-\alpha d) \qquad 3.2$$

where α is the absorption coefficient and d is the sample thickness. Using the definition of transmission $T=I/I_o$, the relationship between transmission and O.D. immediately follows:

$$T=10^{-O.D.} \qquad 3.3$$

The light source for the Cary is a quartzline lamp. Wavelengths from 2000 to 300 nm are scanned by the monochromator of the Cray and the corresponding optical densities are measured and recorded on a strip chart recorder. The maximal optical density the Cary could measure is two, which corresponds to a transmission of 1% and an absorption coefficient on the order of 10^4 cm^{-1} for samples of 1 micron thickness.

The absorption coefficient can be determined from the optical density and the thickness. The relationship between

the absorption coefficient and optical density is deduced by solving a transverse electromagnetic wave traveling through an interface. When transmission and reflection effects are taken into account, T is given by[74]

$$T = \frac{(1-R_{01})(1-R_{12})\exp(-\alpha d)}{1+R_{01}R_{12}\exp(-2\alpha d)+2(R_{01}R_{12})^{1/2}\exp(-\alpha d)\cos(4\pi n_1 d/\lambda)} \qquad 3.4$$

where R_{01} and R_{12} are the reflection coefficients from the air/film and film/substrate interfaces, respectively. The reflection coefficient at the interface between medium A and medium B is given by

$$R_{AB} = \frac{(\mathbf{n}_A - \mathbf{n}_B)^2}{(\mathbf{n}_A + \mathbf{n}_B)^2} \qquad 3.5$$

where $\mathbf{n}_A = n_A + ik_A$ is the complex index of refraction of medium A.

Typical optical density vs. wavelength plots of a-Si:H and a-Ge:H are shown in Fig. 3.1 and Fig. 3.2 respectively. The $\cos(4\pi nd/\lambda)$ term in the denominator of equation 3.4 gives rise to interference fringes. As α increases, this term becomes smaller and eventually negligible. Obviously, the other term which is proportional to $\exp(-2\alpha d)$ can also be ignored. Then equation 3.4 reduces to

$$T = (1 - R_{01})(1 - R_{12})\exp(-\alpha d). \qquad 3.6$$

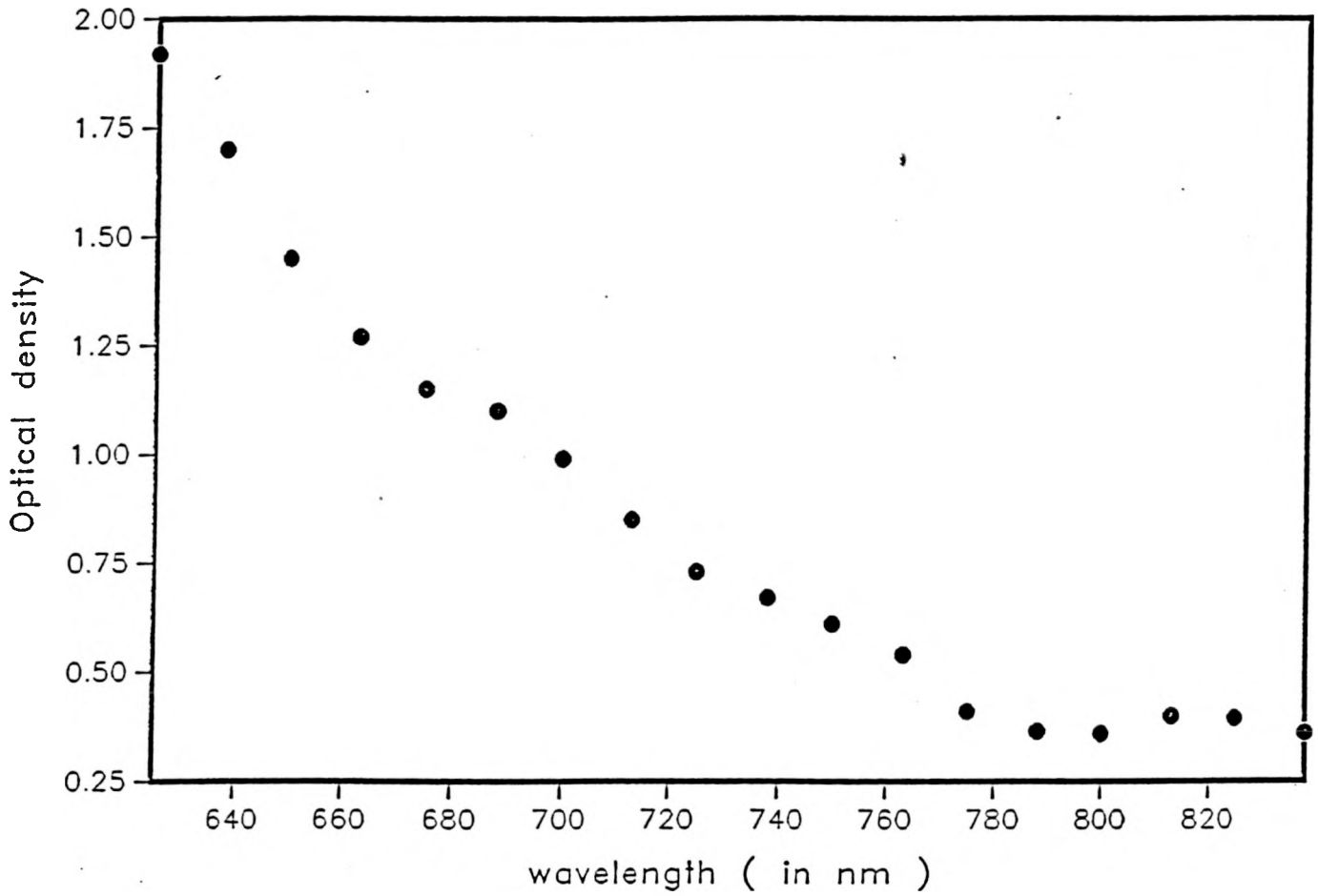

Fig. 3.1 A typical optical density vs wavelength spectrum for a-Si:H

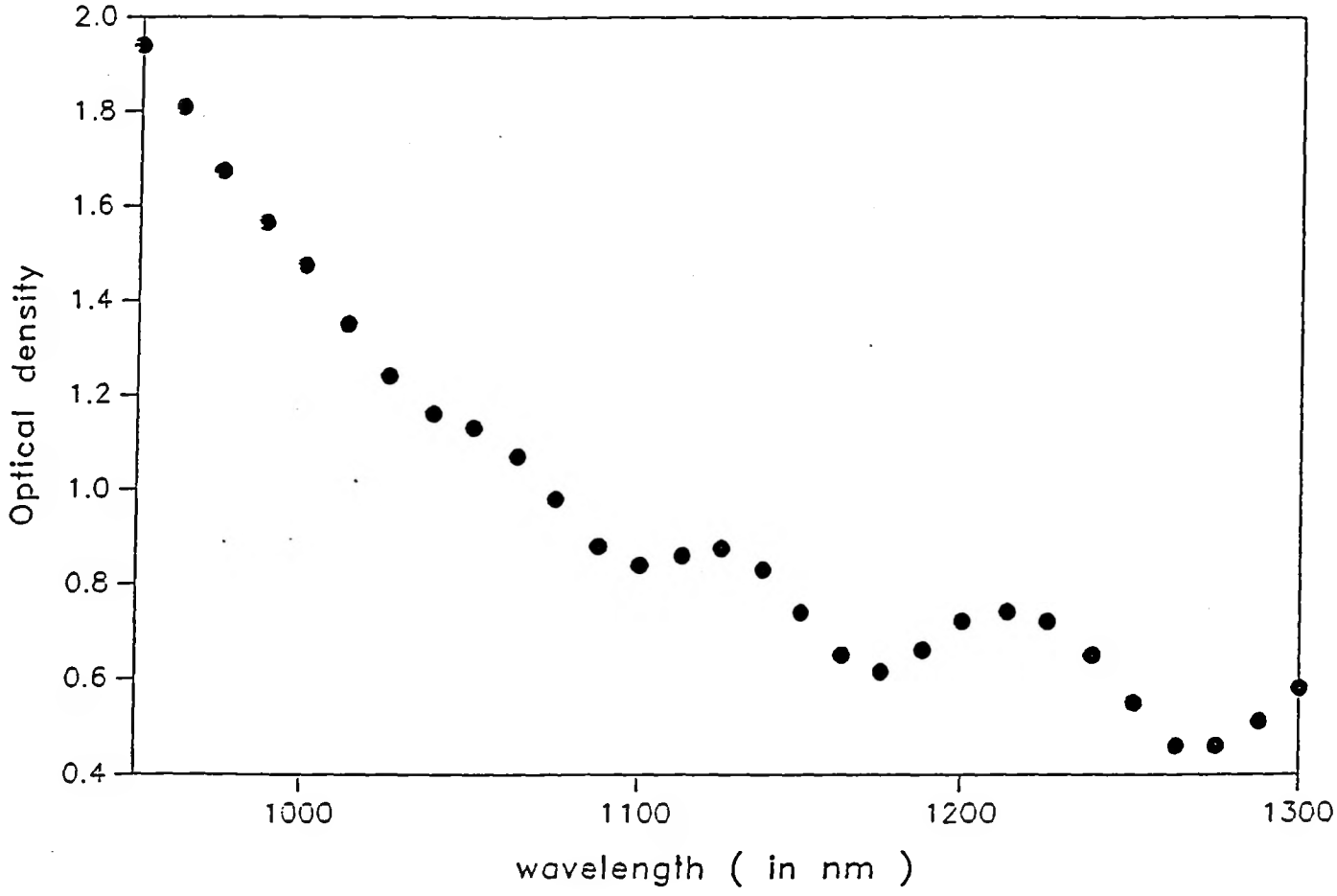

Fig. 3.2 .A typical optical density vs wavelength spectrum for a-Ge:H

The final expression for α is then given by

$$\alpha = -(\frac{1}{d})\ln[\frac{10^{-O.D.}}{T_g(1 - R_{o1})(1 - R_{12})}] \qquad 3.7$$

where T_g is the glass transmission used to compensate for absorption in the glass substrate. The glass was found to have a transmission of 0.97, independent of wavelength in the wavelength region of interest. From this equation, α is completely determined by the complex refractive index $\mathbf{n}_\lambda$ of the film since the sample thickness and the refractive indices of air and Corning 7059 glass are known (1.0 and 1.53 respectively).

Using the fact that for a typical 1 μm sample the maximum value of α that can be measured by the Cary is about 10^4 cm^{-1} at $\lambda \sim 500$ nm, from the relation $k_1 = \alpha\lambda/4\pi$ the estimated maximum value for k_1 is $\sim 10^{-2}$. Though n_1 is a function of wavelength, we can assume n_1 is a constant to simplify the calculation. n_1 is roughly 3.5 for a-Si:H and 4.5 for a-Ge:H. Since $k_1 << (n_1 - n_0)^2$, $(n_2 - n_1)^2$, the reflection coefficients can be simplified to

$$R_{o1} = \frac{(n_1 - 1)^2}{(n_1 + 1)^2} \qquad 3.8$$

and

$$R_{12} = \frac{(n_1 - 1.53)^2}{(n_1 + 1.53)^2} \qquad 3.9$$

Knowledge of sample thickness and eq. 3.7 then yield α.

The structural differences between crystalline and amorphous semiconductors have direct impact on their energy gaps. In a perfect intrinsic crystalline semiconductor, there are no allowed states in the energy gap. Therefore, photons with energies less than E_g can not cause electronic transitions across the gap, hence $\alpha(E) = 0$ for $E < E_g$. The energy needed to cause electronic transitions defines the energy gap E_g. For amorphous semiconductors, the optical energy gap E_g can be determined by using the relation suggested by Tauc et al.:[75]

$$(h\nu\alpha n)^{1/2} = B(h\nu - E_g) \qquad 3.10$$

where B depends on the density of states in the valence and conduction band tails. Typical Tauc plots for a-Si:H and a-Ge:H samples of this work are shown in Fig. 3.3 and Fig. 3.4.

In amorphous semiconductors the optical properties are characterized by the presence of a tail in the optical absorption. A typical absorption spectrum, showing three absorption regions, is depicted in Fig. 3.5. Absorption in region A is due to interband transitions similar to those which occur in crystalline solids. In region B, the optical

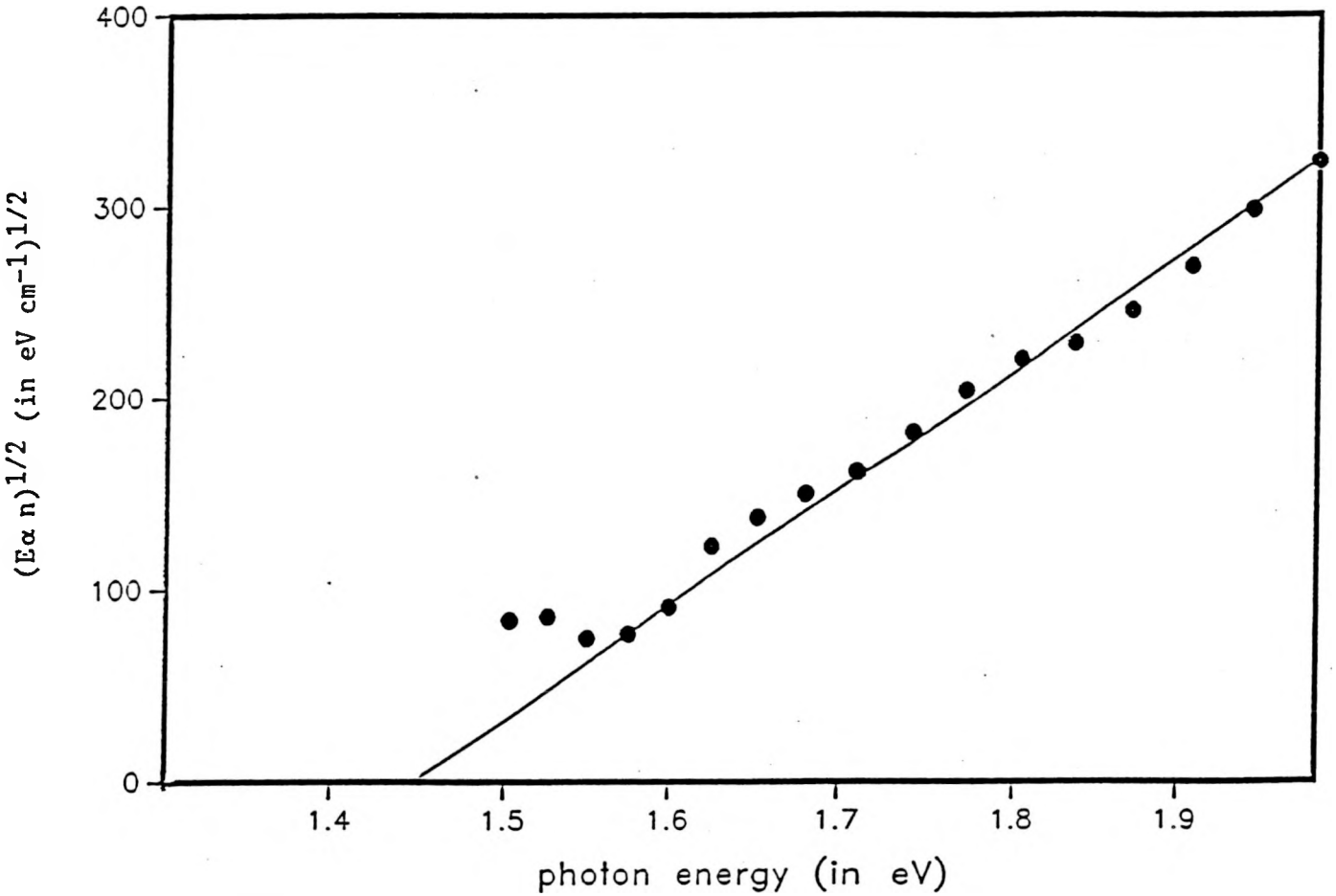

Fig. 3.3 A typical Tauc plot for a-Si:H

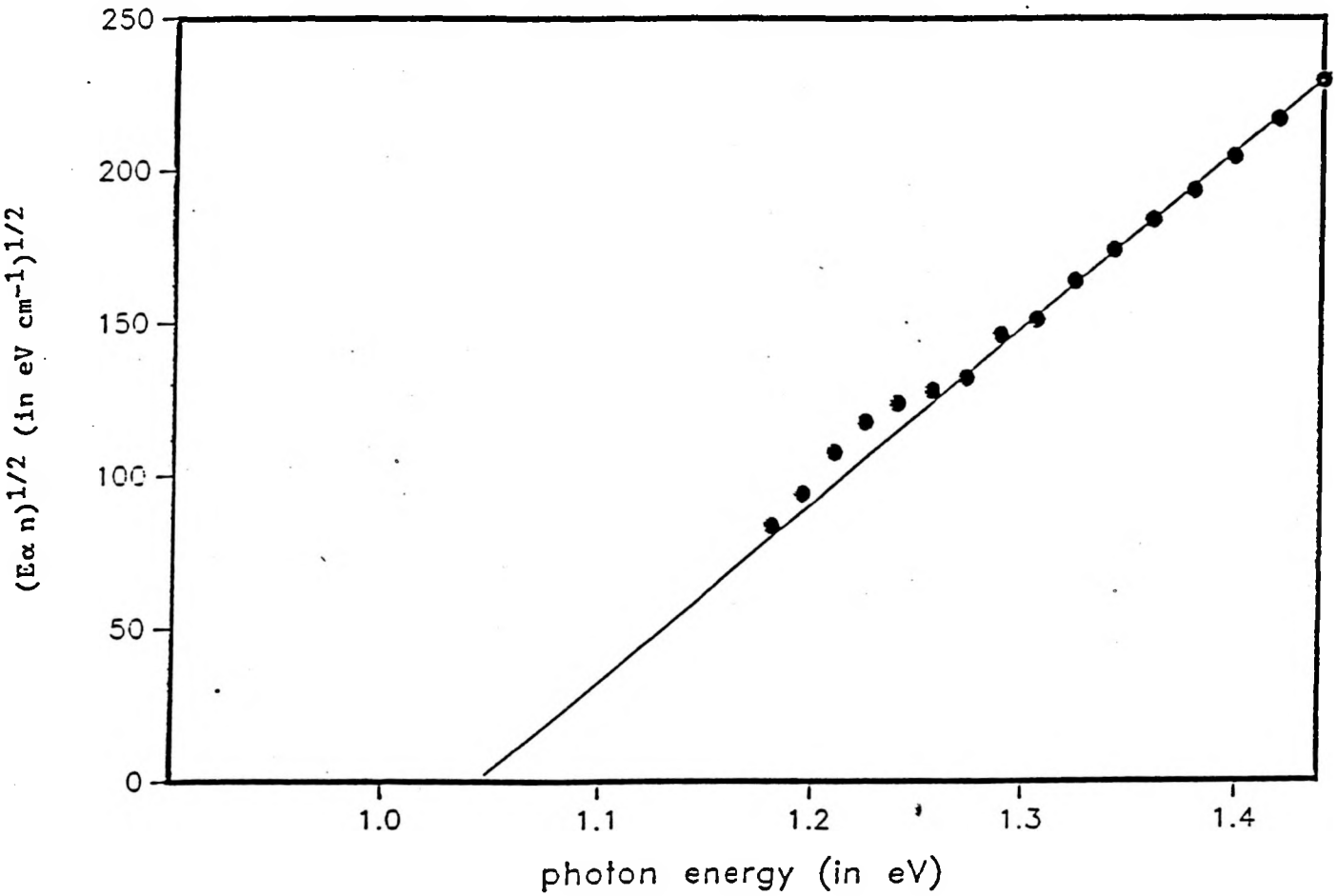

Fig. 3.4 A typical Tauc plot for a-Ge:H

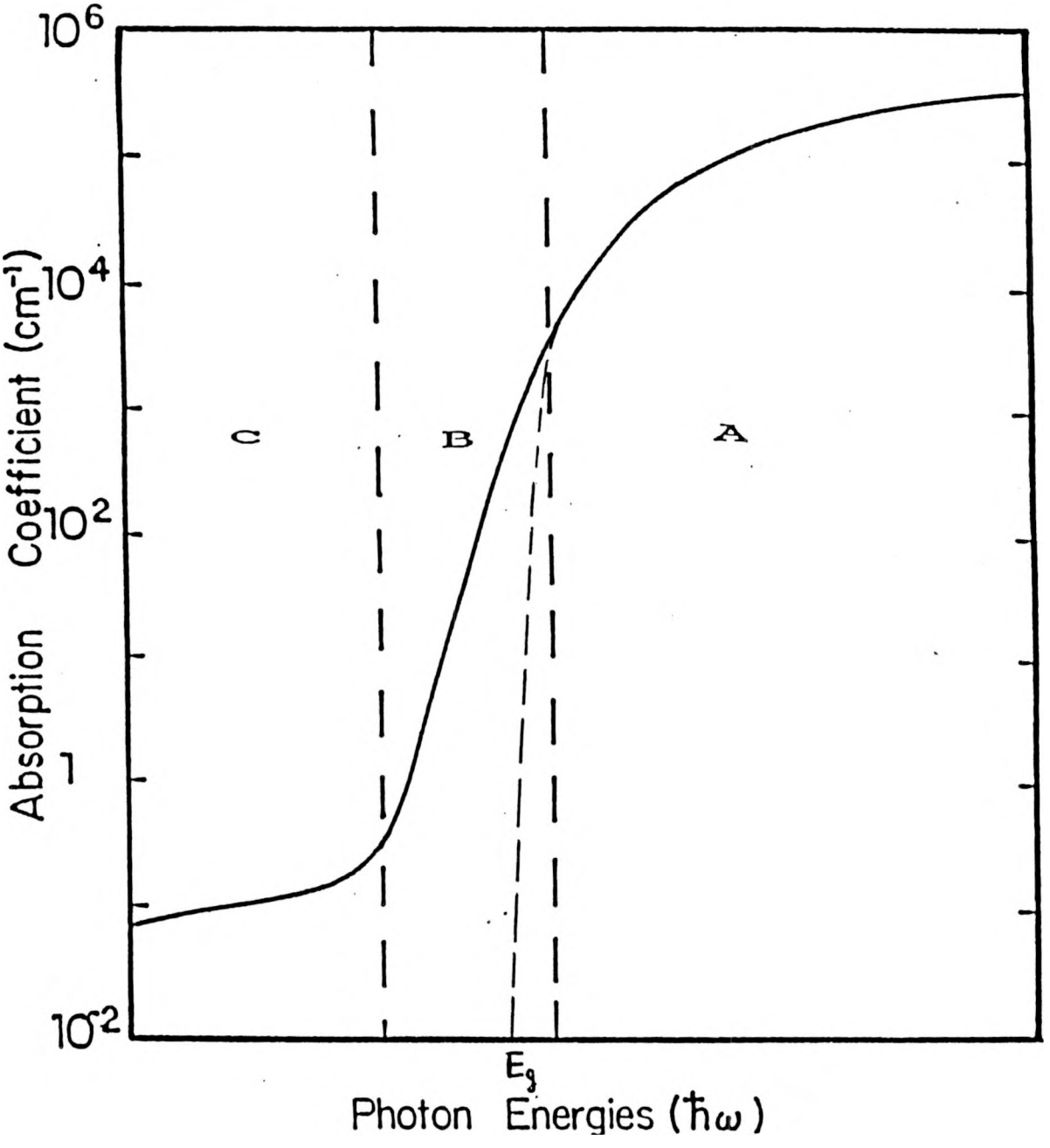

Fig. 3.5 Schematic diagram of a typical absorption edge in an amorphous semiconductor showing the onset of interband transitions (A), the Urbach tail (B), and the sub-gap absorption (C)

absorption decreases exponentially into the spectral region which is normally transparent in crystalline solid. The absorption in this region is dominated by band-tail to band-tail transitions and $\alpha(E)$ can be written as

$$\alpha(E) = \alpha_o \exp\{(E-E_1)/E_o\} \qquad 3.11$$

where α_o, E_1 and E_o are material dependent constants and E_1 has a value close to the optical gap. This absorption resembles the behavior first observed by Urbach[76] in ionic crystals, and is known as the "Urbach edge". E_o is called the Urbach coefficient, and is related to the valence band tail. For a-Si:H, E_o is usually between 0.04 to 0.1 eV. For rf sp a-Ge:H, Wu[68] found that E_o was between 0.2 - 0.3 eV. Large values of E_o imply a high density of tail states and hence greater local disorder. The absorption in the low absorption region C is believed to be caused by transitions involving defect states in the gap.

C. Electron Spin Resonance Measurements

The total number N_s of unpaired spins, due to non-bonding electrons on threefold-coordinated Si (Ge) atoms (i.e., dangling bonds), can be measured by using electron spin resonance (ESR) spectroscopy. N_s is one of the most direct measurement of film quality. Since dangling bonds create deep

states in the gap,[77] which serve as recombination centers, photoconductivity as well as photoluminescence efficiency decrease rapidly with increasing N_s.

ESR measurements were carried out on a Bruker ER220 DSR X-band spectrometer. A PC computer is interfaced with the spectrometer through a Metrabyte DASH-16 interface board, which controls the data acquisition. The samples are deposited on Corning 7059 glass substrates and then cut into strips of one-half inch by four millimeters. The reference used was a sample of DPPH with 1.2×10^{17} spins, which was determined by using a $Mn:CaF_2$ sample with a known number of spins.

The magnetic moment μ of an electron is related to its spin by

$$\mu = -g(e\hbar/2mc)s = -g\beta s \qquad 3.12$$

where ß is the Bohr magneton = 0.927×10^{-20} erg $gauss^{-1}$, and g is the spectroscopic splitting factor (g = 2.0023 for free electron). When an external magnetic field **H** is applied to the system, the interaction between the magnetic moment and the field is characterized by an interaction energy

$$E = -\mu H. \qquad 3.13$$

The energy difference between the two electron spin states is

$$\Delta E = E_{\uparrow} - E_{\downarrow} = g\beta H \qquad 3.14$$

Resonant transitions between these levels are induced if ΔE is matched by electromagnetic radiation with an angular frequency ω_o such that $\Delta E = \hbar\omega_o$. Thus

$$\omega_o = g\beta H_o/\hbar. \qquad 3.15$$

This resonance can, in principle, be detected by two approaches. In the first method, the magnetic field H_o is constant and the electromagnetic frequency ω is scanned until the resonance condition $\omega_o=g\beta H_o/\hbar$ is met. In the second method, the electromagnetic frequency is constant while the magnetic field H is swept over a range centered around the resonance field $H_o=\hbar\omega_o/g\beta$. The latter is by far the common one and also used in this work. The typical magnetic field used at the X-band frequency of 9.3 GHz was ~ 3340 gauss. The H sweeping range was 3340 ± 50 gauss for a-Si:H and 3340 ± 100 gauss for a-Ge:H.

The ESR measurements were performed by inserting the sample into a microwave cavity which was located between the centers of a large pair of magnetic pole pieces. A small modulation field (usually ≤ 1/3 of the width of the resonance

absorption peak) was applied at a frequency of 100 KHz and the resonance was phase sensitive lock-in detected by its effect on a balanced microwave bridge. Lock-in detection greatly enhances the sensitivity. Since the reference of the lock-in is a modulation of the swept quantity, the derivative dN/dH of the absorption is detected. Typical spectra of dN/dH vs. H are shown in Figs. 3.6 and 3.7 for a-Si:H and a-Ge:H, respectively. By comparing with the reference spectrum, the number of spins in a sample is given by[78]

$$N_s = N_r \frac{(\Delta H_{pp}^{\,s})^2\ (Y^s)\ (H_{mod}^{\,r})\ (P_w^{\,r})^{1/2}\ (G^r)\ (K_s^{\,r})\ (\Lambda^s)}{(\Delta H_{pp}^{\,r})^2\ (Y^r)\ (H_{mod}^{\,s})\ (P_w^{\,s})^{1/2}\ (G^s)\ (K_s^{\,s})\ (\Lambda^r)} \qquad 3.16$$

where the subscripts r and s represent the reference and sample, respectively. ΔH_{pp} and Y are the peak-to-peak width and amplitude of the resonance in the derivative mode. H_{mod} is the magnitude of the modulation field. P is the power, G is the lock-in gain, K_s is the number of scans, and Λ is the line shape factor. For the first derivative spectrum, Λ is 1.03 for standard Gaussian and 3.63 for Lorentzian lines.[79] The actual line shape factors are usually between these two extreme values.

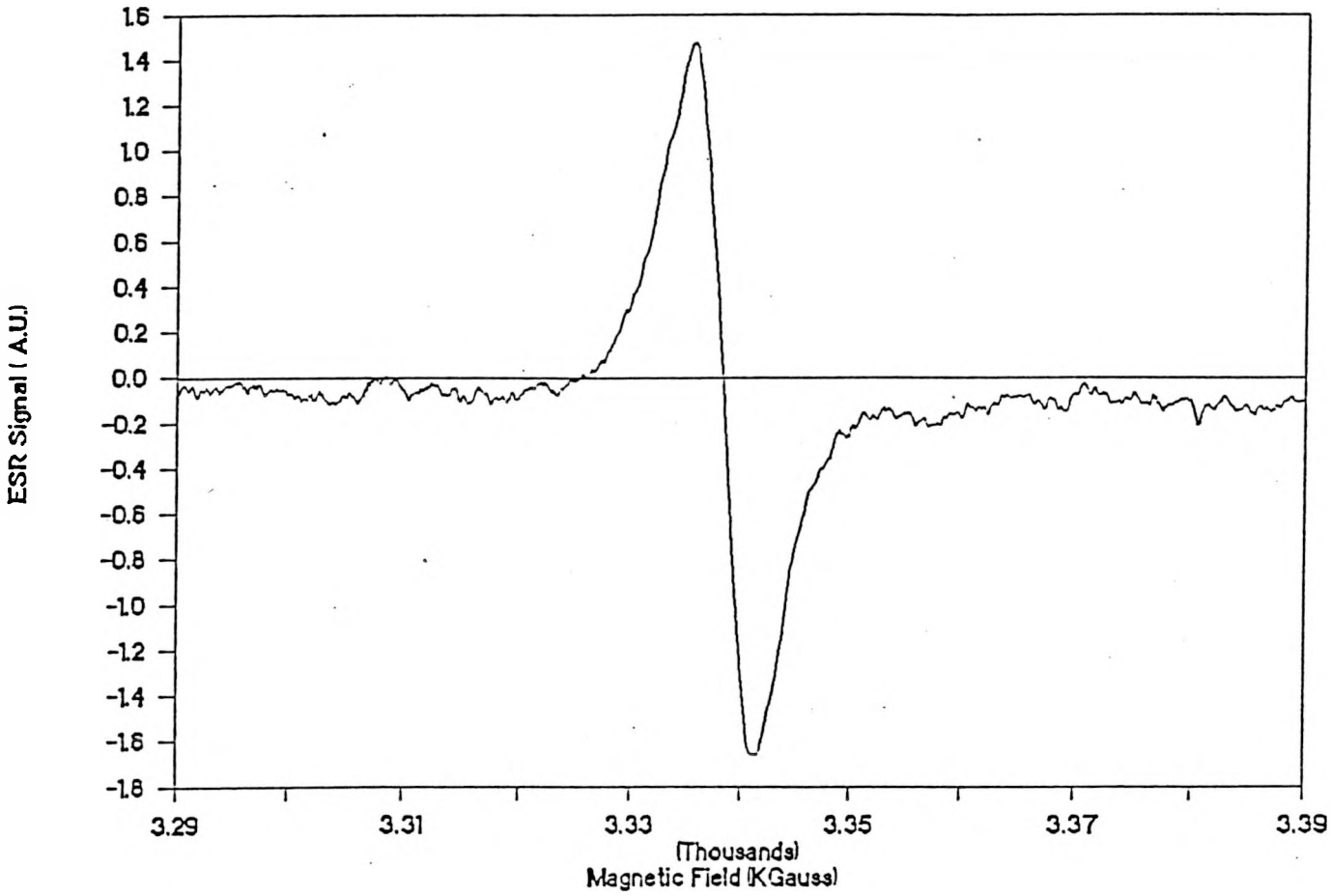

Fig. 3.6 An Electron Spin Resonance (ESR) room-temperature derivative spectrum of a typical a-Si:H film

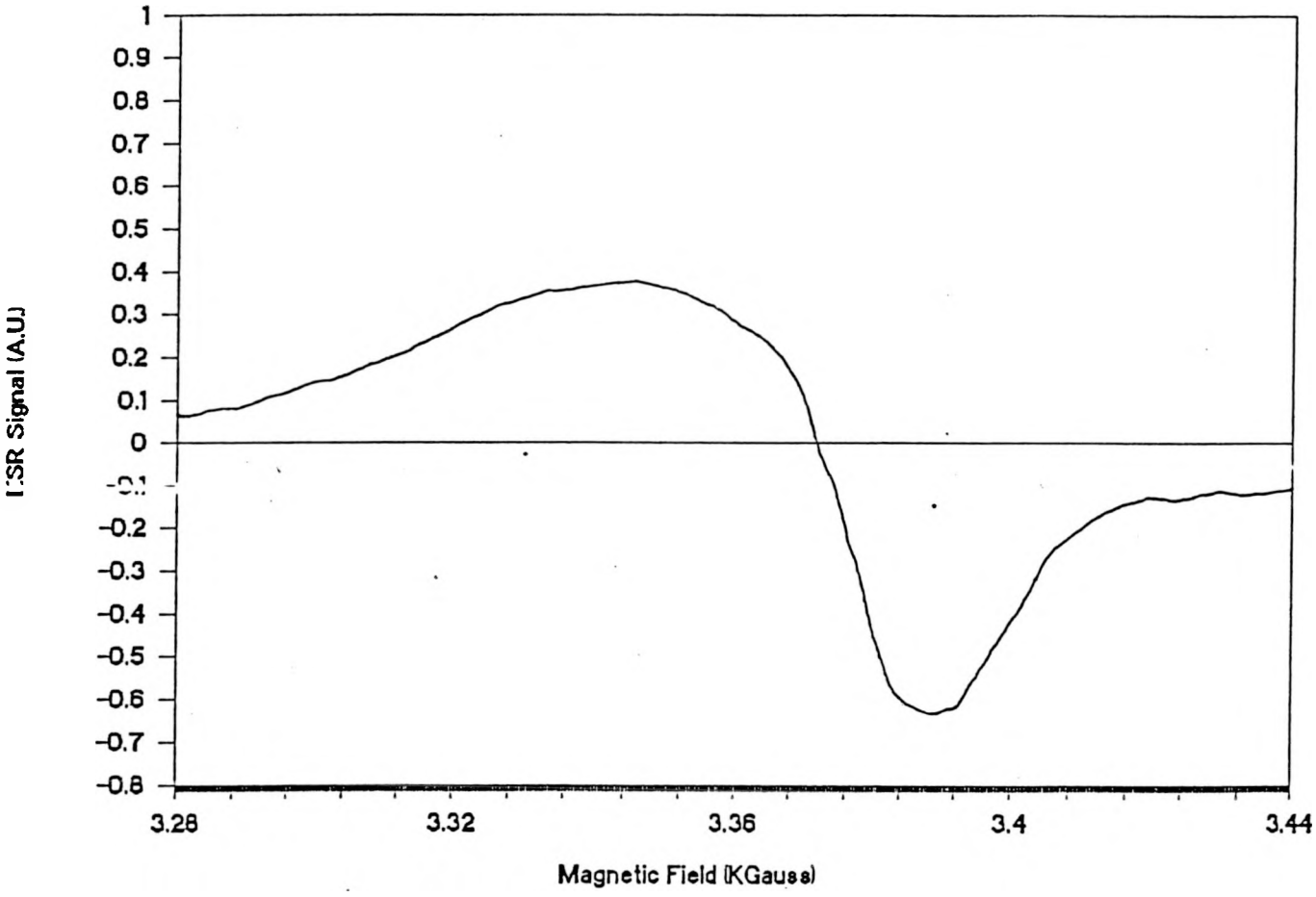

Fig. 3.7 An Electron Spin Resonance (ESR) room-temperature derivative spectrum of a typical a-Ge:H film

D. Infrared Measurements

Infrared (IR) absorption measurements of the vibrational modes yield important information on a-Si:H and a-Ge:H. The peak positions indicate the bonding configurations of the hydrogen atoms as well as oxygen or nitrogen impurity contamination. The integration over certain peaks yields information on the hydrogen concentration. A single beam Fourier Transform Infrared (FTIR) spectrometer, IBM model IR98, was used in our measurements. All samples used in the IR measurements were deposited on single crystal silicon. Other blank pieces from the same wafer substrate were used as reference.

Typical IR spectra of a-Si:H and a-Ge:H are shown in Figs. 3.8 and 3.9. A variety of vibrational modes are observed. The major vibrational modes for hydrogen in a-Si:H were identified by Brodsky et al.[80]. The corresponding bonding configurations are depicted in Fig. 3.10. The three modes are (1) the Si-H stretching mode (2000-2100 cm^{-1}), (2) the $Si-H_2$ and $Si-H_3$ bond bending scissors mode (840-890 cm^{-1}), and (3) the Si-H wagging mode (640 cm^{-1}). The absorption peaks in a-Ge:H are at slightly lower frequencies, mainly due to the higher atomic mass of Ge. They are at 1870-1970, 780, and 580 cm^{-1}, respectively. The deuterium-related peaks are similarly at lower frequencies. Since the content of D_2 was small, its influence on the IR spectra could be neglected. If the

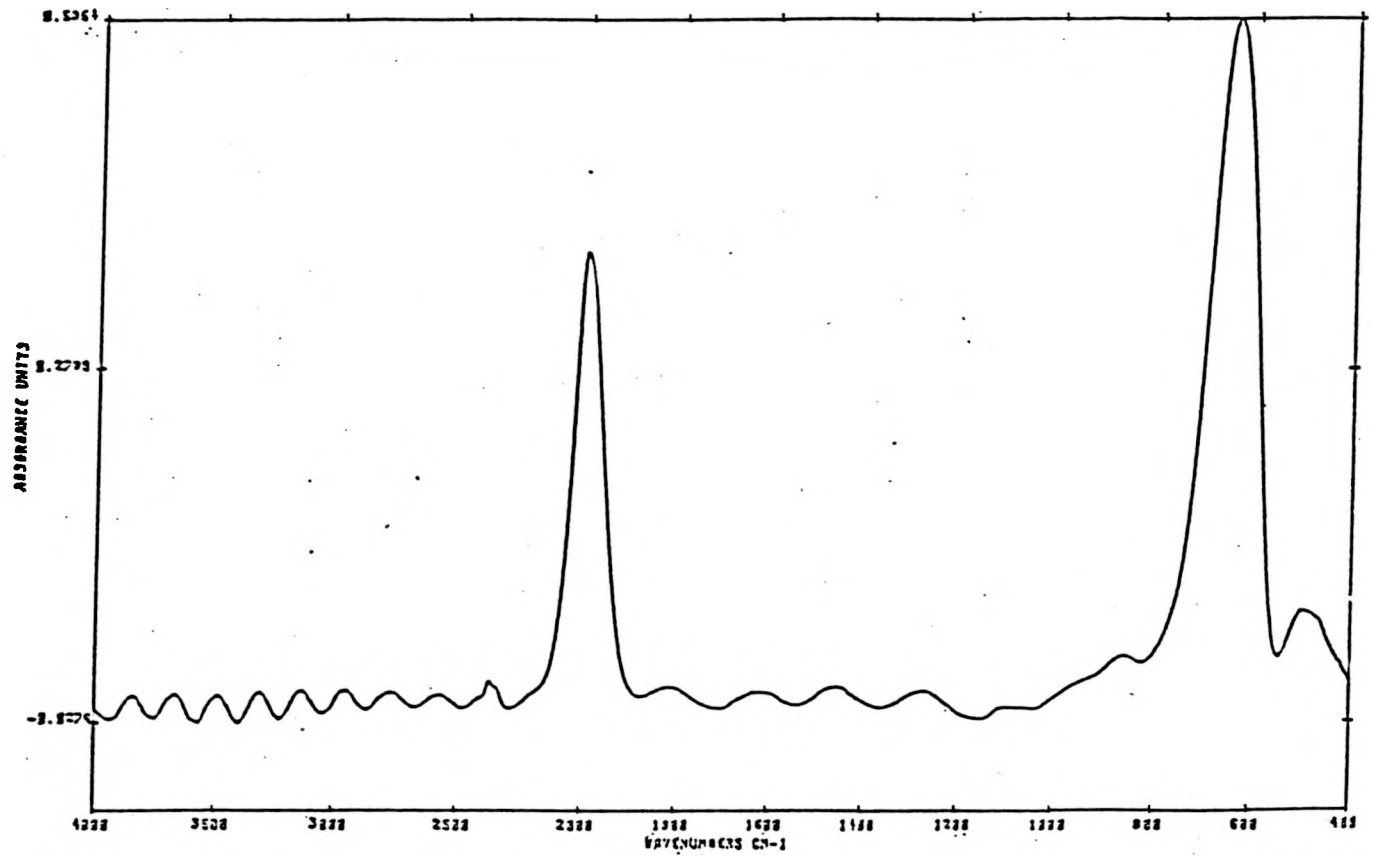

Fig. 3.8 The IR absorption spectrum of a typical a-Si:H film

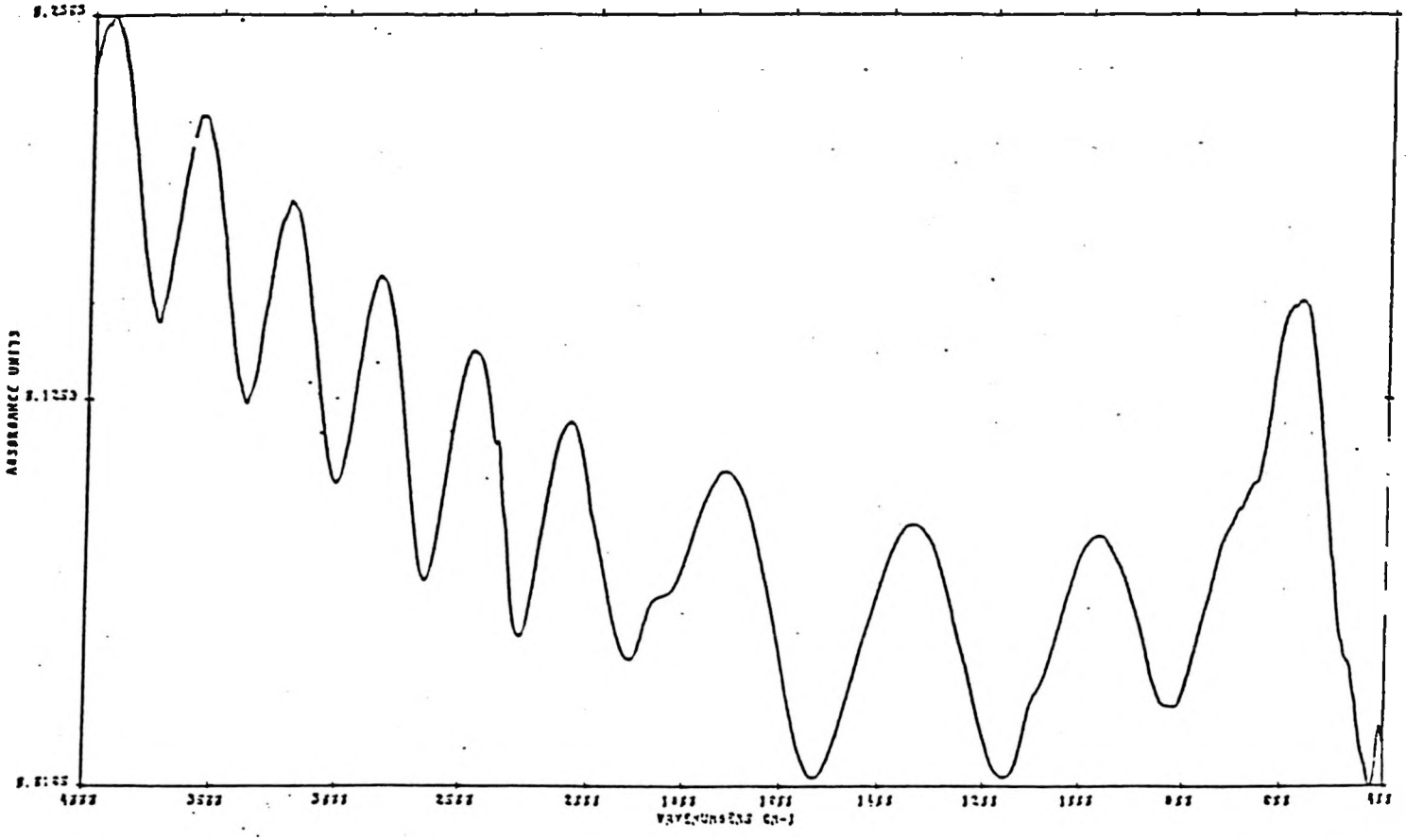

Fig. 3.9 The IR absorption spectrum of a typical a-Ge:H film

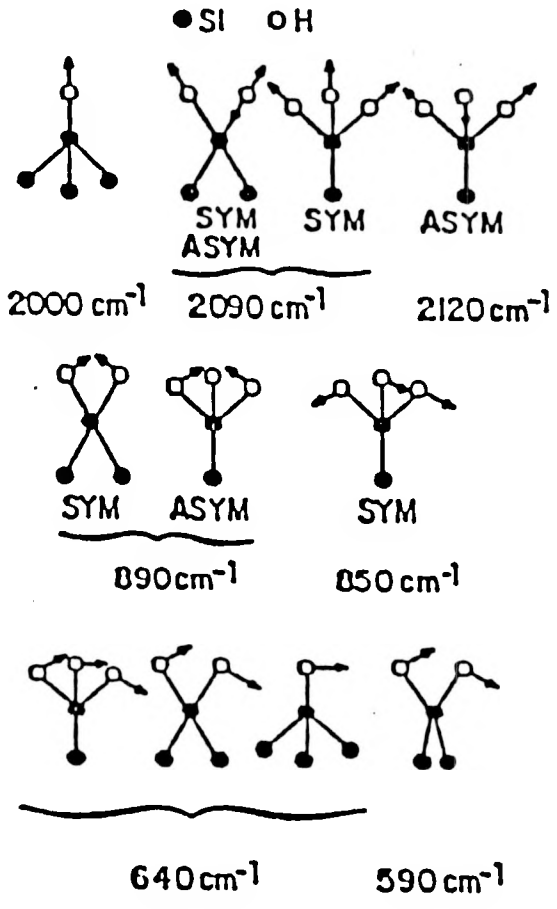

Fig. 3.10 Schematic illustration of the bond stretching (top row), bond bending (middle row), and bond wagging and rocking (bottom row) modes of SiH, SiH_2, and SiH_3. SYM and ASYM indicate symmetric and asymmetric modes respectively. The solid and open circles represent Si and H atoms respectively (from Ref. 80)

hydrogen content is low, the absorption intensity will usually be weaker than the interference fringes, which complicates the quantitative analysis.

The Si (or Ge) bonded H content is determined from the integrated intensity of the 640 (580) cm^{-1} wagging mode, using calibration coefficient provided by Shanks et al.[81] and Catherine et al.[82]. The coefficient was shown to be insensitive to the bonding configuration and microstructure in a-Si:H, and is believed to be similarly insensitive in a-Ge:H as well. The hydrogen content determined from this absorption peak is consequently believed to be reliable. The equation used to calculate the hydrogen content is given by Cardona[83,84]:

$$N_H = A \int [\alpha(\omega)/\omega] d\omega \qquad 3.17$$

where A is an experimentally determined constant, and $\alpha(\omega)$ is the absorption coefficient at frequency ω. The integral extends over the absorption band of interest. The values of A for the various vibrational modes in Si and Ge are listed in Table 3.1. The following expression gives the hydrogen concentration C_H in a-Si:H:

$$C_H(\text{at.}\%) = 1.125\ S_{640}/d \qquad 3.18$$

Table 3.1 The various vibrational modes of hydrogen in a-Si:H and a-Ge:H, their bonding configurations and the corresponding proportionality constant A (from Refs. 81, 82 and 84)

For a-Si:H

Wavenumber (cm^{-1})	640	840-890	2000	~2100	2100
Mode	Wag	Scissors	Stretch	Stretch	Stretch
Bonding	Si-H $Si-H_2$ $Si-H_3$	$Si-H_2$	Si-H (Isolated)	Si-H (clustered)	$Si-H_2$ $Si-H_3$
A (cm^{-1}) (10^{19})	1.6	20	2.2	17	9.1

For a-Ge:H

Wavenumber (cm^{-1})	565-575	760-825	1875-1895	1960-1970
Mode	Wag	Scissors	Stretch	Stretch
Bonding	Ge-H $Ge-H_2$	$Ge-H_2$	Ge-H	$Ge-H_2$
A (cm^{-2}) (10^{19})	1.1		5.0	14

where S_{640} is the area (in cm^{-1}) under the 640 cm^{-1} absorption peak and d is the thickness in microns. Similarly, for a-Ge:H

$$C_H(at.\%) = 1.0\ S_{580}/d \qquad 3.19$$

where S_{580} is the area (in cm^{-1}) under the 580 cm^{-1} absorption peak. The atomic percentage of Si in $Si-H_2$ and $Si-H_3$ is given by

$$N_d(at.\%) = 10.44\ S_{840}/d \qquad 3.20$$

and that of $Ge-H_2$ and $Ge-H_3$ is given by

$$N_d(at.\%) = 11.5\ S_{780}/d \qquad 3.21$$

We note, however, that since the films were deposited on polished Si wafers, the intensity of the GeH_2 scissors (bending) mode absorption at 780 cm^{-1} was much weaker than the interference fringes in the IR spectra. It was thus impossible to determine the dihydride and trihydride content of the a-Ge:H films.

The interpretation of the Si-H stretch peaks is problematic. Although the shape of the Si-H stretch mode absorption could be clearly determined, and generally yielded peaks at ~ 2000 and ~ 2100 cm^{-1}, the information it yields on

the bonding configuration and microstructure is ambiguous: A Si-H bond vibrating at 2000 cm^{-1} is assigned either to a H atom embedded in the bulk, or to an atom on the surface of a "compact" microvoid, where opposite surfaces are less than ~ 3 Å apart.[85,86] A Si-H bond vibrating at ~ 2100 cm^{-1} is assigned either to a SiH_2 (dihydride), SiH_3 (trihydride), or a monohydride centered on the surface of a larger microvoid (opposite surface more than ~ 4 Å apart). The above discussion should also be applicable to a-Ge:H, i.e., the 1850 - 1875 cm^{-1} peak is probably due to mono Ge-H in the bulk or in "compact" microvoids; the 1950 cm^{-1} is apparently due to $Ge-H_2$, $Ge-H_3$ or to Ge-H bonds at internal surface of larger microvoids. A simple dielectric screening model suggests that, as the void radius around the hydrogen increases to ~ 2 Å, the stretch frequency of a Si-H (monohydride) bond increases to ~ 2100 cm^{-1}.[84,87]

Oxygen contents above ~ 0.5 at.% in the samples can easily be detected from the Si-O and Ge-O stretch vibration bands. For a-Si:H samples, the 900 cm^{-1} peak is related to bulk Si-O bonds,[15] while the 1100 cm^{-1} is attributed to oxygen bonded at internal surfaces. In a-Ge:H films, the 850 cm-1 is assigned to the bulk Ge-O stretch vibration band.[88]

E. Secondary Ion Mass Spectrometry

Information on long range hydrogen (or deuterium) motion can be obtained from their depth profiles using secondary ion mass spectrometry (SIMS).*** During a SIMS measurement, atomic and molecular particles are sputtered off when the surface is bombarded by energetic ions (typical energy range from 0.5 to 20 keV). Secondary ions sputtered off the films are detected by a mass spectrometer. These ions may be emitted from the surface in the ionized state or they may be initially emitted as neutrals and ionized before analysis. The system is operated under ultra-high vacuum (UHV) conditions.

There are three operation modes. These are static, dynamic, and imaging SIMS. In the static mode, high surface sensitivity with minimum surface damage can be achieved by using very low primary ion current densities. The dynamic mode, which was employed in this work, involves a high flux of primary ions directed at the material surface in order to obtain a high yield of secondary ions. The surface is eroded and a well defined crater is created. Hence, a depth profile is generated by monitoring changes of elemental composition with depth. This technique is thus destructive since it relies on particle removal from a surface. In the imaging

---

*** The SIMS measurements were performed by Dr. Ruth Shinar at the Microelectronics Research Center, Iowa State University, Ames, Iowa 50011.

mode, a highly focused scanning ion beam is used to raster over the surface and the secondary ions generated at each point are collected and stored in a computer to form a chemical map of the surface.

A Perkin Elmer model PHI 6300 SIMS was used to depth-profile the films which were deposited on silicon wafer substrates. Fig. 3.11 is a block diagram of a SIMS system. The main components are the primary ion beam and the mass spectrometer. A primary beam of 4-6 keV positive cesium ions Cs^+, generated by surface ionization, was used to produce negative secondary ions. This beam has a diameter of 50 - 60 μm and strikes the sample surface at an angle of 30° to the surface normal. The raster size was 500x500 μm^2. The mass spectrometer consists of an energy and quadrupole mass analysers. The secondary ions are analyzed according to their mass to charge ratio (m/e). The electronegative ion D^- (m/e = -2) is used to detect deuterium, since it has a greater dynamic range than that of D^+ ion, which has the same mass to charge ratio (m/e = +2) as H_2^+. Thus, the interference from H_2^+ is avoided. Typical deuterium depth profiles of a-Si:H/a-Si:(H,D)/a-Si:H and a-Ge:H/a-Ge:(H,D)/a-Ge:H are shown in Figs. 3.12 and 3.13. The x axis corresponds to the sputtering time, which is proportional to the etching depth. The y axis is the secondary ion current intensity in units of counts/s. The sharp drop in the concentration is used to define the

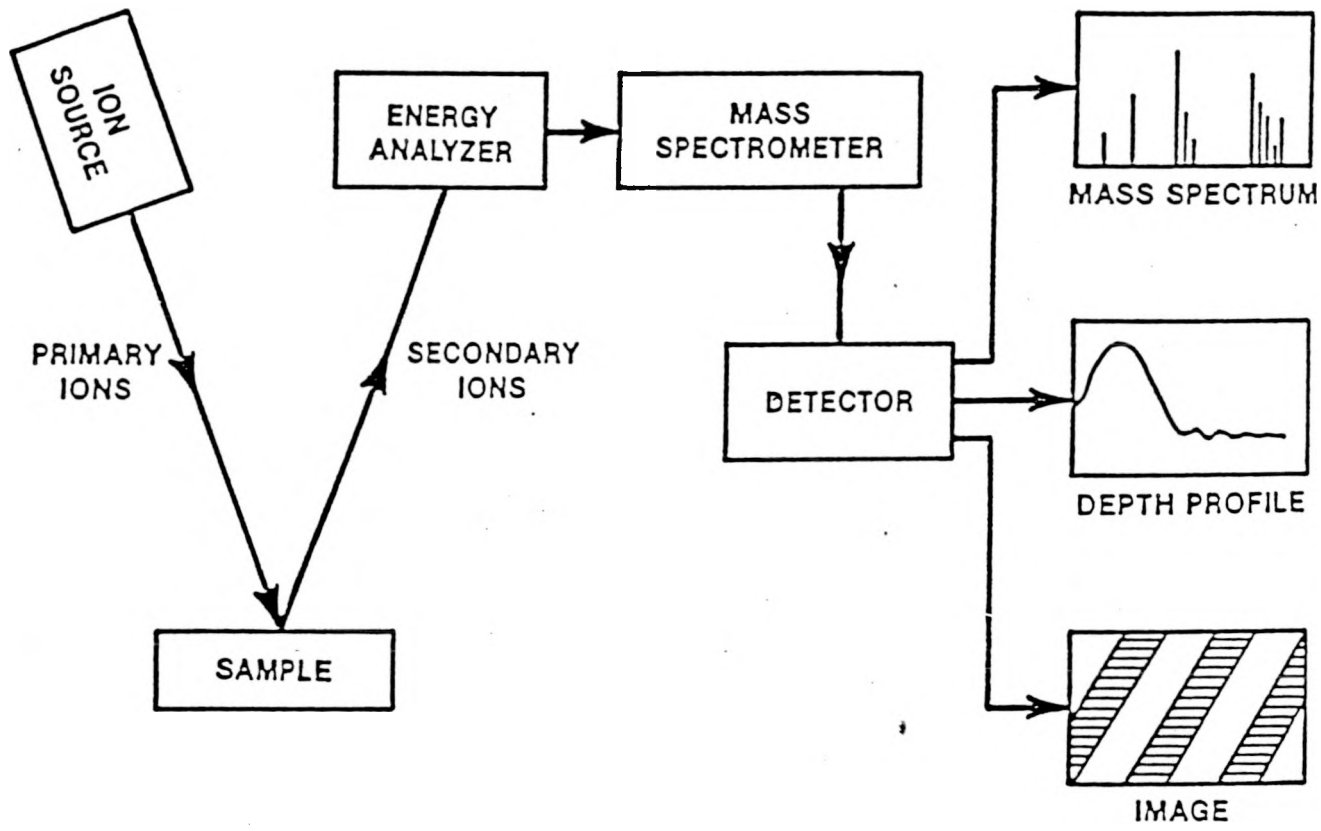

Fig. 3.11 SIMS technique block diagram

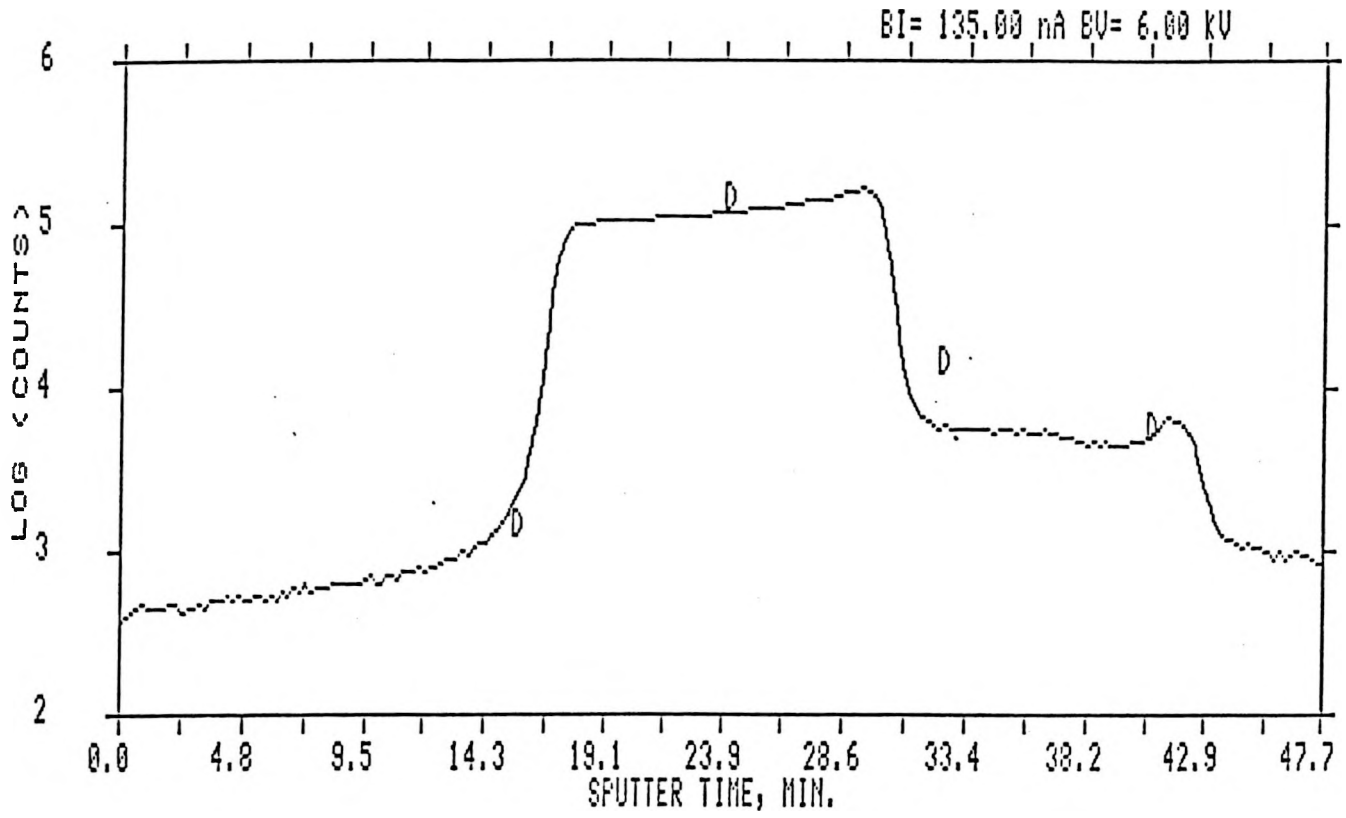

Fig. 3.12 SIMS depth profile of a typical a-Si:H film

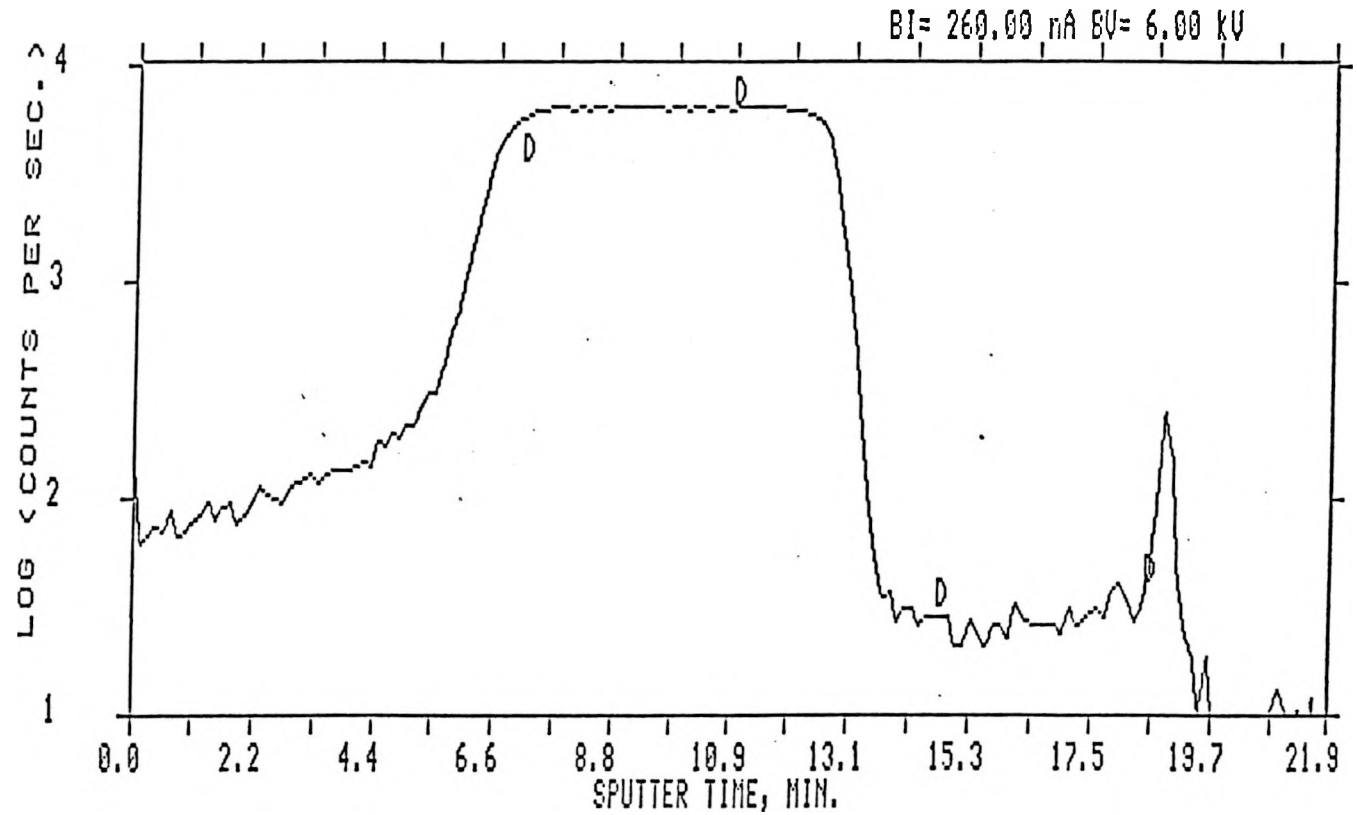

Fig. 3.13 SIMS depth profile of a typical a-Ge:H film

film/substrate interface. It also determines the depth resolution of the profiles, which is typically ~ 150 Å at the interface of a ~ 1.5 μm thick film.

Besides hydrogen and deuterium, other atomic species such as oxygen, carbon, silicon and germanium are also occasionally monitored to check homogeneity and contamination levels. This is achieved by simultaneously monitoring their corresponding (m/e) values. Since the quadrupole mass analyzer does not employ magnets, this peak switching process can be done quickly without hysteresis effects.

To obtain reliable SIMS profiles, some instrument parameters need to be chosen carefully. For accurate profile analyses, the properties of the analyzed materials as well as the physics of the sputtering process may significantly affect the resulting spectra.

It is very important to keep the bombardment uniform and the ion contribution from the crater wall minimized. The former can be realized by keeping the primary beam current and the ion impact energy constant during data acquisition. The primary ion current stability should be verified at the beginning and the end of the analyses. The sputtering rate should be decided after considering the available time, required depth resolution, detection limit, and profile shape quality. Generally, increasing the primary beam current will increase the beam size. Fig. 3.14 depicts the beam diameter

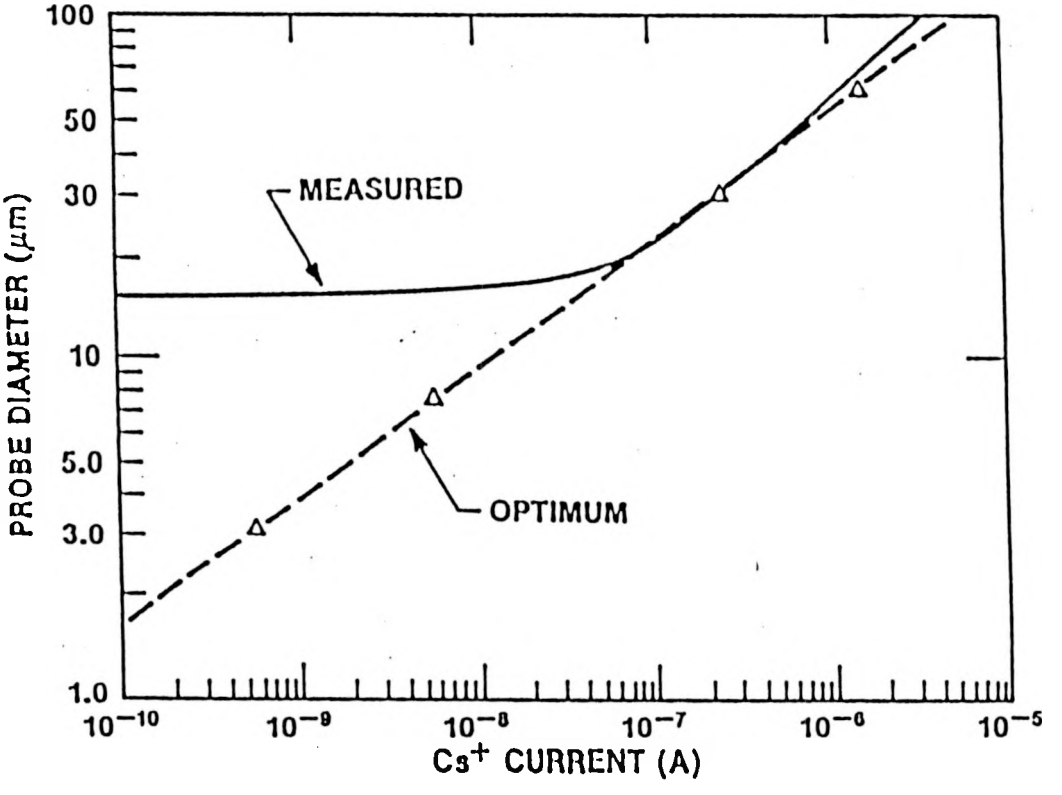

Fig. 3.14 Probe diameter relationship to Cs^+ ion current for Perkin Elmer PHI-6300 Cs source (from Ref. 89)

versus current of a Cs beam on a Perkin Elmer PHI-6300 source.[89] The beam currents for this work were maintaind between 500 nA to 700 nA, and yielded beam sizes of about 50 μm. The raster size cannot be too small, otherwise the profile quality will deteriorate due to crater side wall effect. For the same reason, not all the rastered area can be used for detection of secondary ions. On the other hand, the probability of nonuniform bombardment of the analysis area increases as the area is increased. Therefore, there is an optimal balance between the ion beam raster and the detected area so that the crater sidewall effects can be avoided and the sputtering rate and depth resolution can be optimized. A crater with a width three to five times that of the width of the detected area usually gives satisfactory results. In this work, electronic gating was employed so that the detected area was limited to 125x125 μm^2 about the center of the crater.

IV. RESULTS ON UNDOPED a-Si:H

A. Introductory Comment

As we discussed in chapter I, many metastable changes may be related to hydrogen motion. A good understanding of hydrogen motion may lead to knowledge on the nature of defects and defect dynamics.

The samples studied in this work are all in thin film form. Their geometry suggests that we can simplify the diffusion equation from its general form

$$\frac{\partial C}{\partial t} = D_{xx} \frac{\partial^2 C}{\partial x^2} + D_{yy} \frac{\partial^2 C}{\partial y^2} + D_{zz} \frac{\partial^2 C}{\partial z^2} \qquad 4.1$$

to the one-dimension form

$$\frac{\partial C(x,t)}{\partial t} = D \frac{\partial^2 C(x,t)}{\partial x^2} \qquad 4.2$$

where C(x,t) is the deuterium concentration at location x at time t, and D is the diffusion coefficient.

The closest form of boundary conditions for the multilayer structure is that of semi-infinite slabs in contact at the interfaces. Hence at the bottom D/H interface, the boundary conditions are:

$$C(x,0) = \begin{cases} 0; & x>0 \\ C_o; & x<0 \end{cases}$$

and $C(x,t) \rightarrow 0$ as x approaches to infinity at any t. If x is replaced by -x, the same boundary conditions are applicable for the top H/D interface.

The solution to the diffusion equation subject to the above boundary conditions has the form of a complementary error function[90]

$$C(x,t) = C_o/2 \ \mathrm{erfc}[x/(4Dt)^{1/2}] \qquad 4.3$$

where C_o is the deuterium concentration at the x = 0 boundary; t is the annealing time and D is the time-independent diffusion constant. For dispersive diffusion where D is time dependent, D(t) is replaced by

$$\theta = \int_0^t D(\tau)d\tau \qquad 4.4$$

Equation 4.2 can be transformed into

$$\frac{\partial C(x,\theta)}{\partial \theta} = \frac{\partial^2 C(x,\theta)}{\partial x^2} \qquad 4.5$$

By using the same boundary conditions, the solution in the right half plane is given by

$$\begin{aligned} C(x,\theta) &= C_o/2 \ \mathrm{erfc}[x/(4\theta)^{1/2}] \\ &= C_o/2\{1-\mathrm{erf}[x/(4\theta)^{1/2}]\} \end{aligned} \qquad 4.6$$

Hence, despite the time dependence of diffusion coefficient,

the deuterium depth profile still has an error function shape.

Using equations 1.2 and 4.4,

$$\theta(t) = \int_0^t D(\tau)d\tau = \theta_o\, t^{1-\alpha} \qquad 4.7$$

$\theta^{1/2}$ obviously has the dimension of length, and is related to the diffusion length L by:

$$L \equiv 2\theta^{1/2} \qquad 4.8$$

or

$$L^2 = 4\theta = 4 \int_0^{t_L} D(\tau)d\tau = 4\theta_o\, t_L^{1-\alpha} \qquad 4.9$$

thus,

$$D(t_L) = L^2(1-\alpha)/4t_L \qquad 4.10$$

where t_L is the time needed to diffuse a distance L. The hydrogen concentration profile falls to 1/e of its initial value at that point.

If $\alpha = 1 - T/T_o$, then equation 4.10 can be rewritten in the form

$$D(t_L) = D_o \exp(-E_{diff}/kT) \qquad 4.11$$

where

$$D_o = L^2\omega(1-\alpha)/4 \qquad 4.12$$

and

$$E_{diff} = kT_o \ln\{[L^2\omega(1-\alpha)]/(4D_{oo})\} \qquad 4.13$$

Thus, it can shown that

$$D_o = D_{oo} \exp(E_{diff}/kT_o) \qquad 4.14$$

This relation between the activation energy and the prefactor is known as the Meyer-Neldel relation (MNR).[64] Equations 4.11 - 4.14 demonstrate that the diffusion for a constant diffusion distance is thermally activated with an activation energy E_{diff}. As L increases, hydrogen becomes progressively trapped in deeper sites and the activation energy E_{diff} increases. Since the only assumption involved in the derivation is that the motion is power-law time dependent, and the dispersive motion is related to the multiple trapping (MT) model as $\alpha = 1 - T/T_o$, MNR follows from the MT model.[64] A MNR between E_{diff} and attempt frequency ν_o extending over 16 orders of magnitude in ν_o has been observed in annealing of various metastable defects in a-Si:H.[64] It has not been verified for H motion in a-Si:H, however. On the other hand, Kirchheim and Huang[91] have questioned its significance in many systems.

In another development, Shinar et al.[63] reported that an excessive microvoid content suppresses H motion in undoped rf sputter-deposited (rf sp) a-Si:H, i.e., $\alpha = 1$. This occurs even when a large fraction of the hydrogen remains bonded in a bulk-like mono-H configuration after annealing, as concluded from an IR stretch peak at 2000 cm^{-1}. In films of somewhat

lower microvoid content, $\alpha \simeq 0.75 \pm 0.15$ at $270 \leq T \leq 350$ °C, yielding an anomalously high $T_o \simeq 2300$ K. Since microvoids apparently remove floating and dangling bonds from the bulk,[92] these results appeared to be clearer within the framework of Pantelides's "floating-bond" model.[29,30,38] Recent measurements,[93] however, claim that the electron spin resonance (ESR) active defect, whether floating or dangling bond, of lower mobility and much lower density than hydrogen, cannot mediate the latter's motion. The role of microvoids and the MT model thus remained unsettled.

In this study, the dispersive diffusion was measured in undoped hydrogenated amorphous silicon of varying H content C_H, diffusion length L, and microvoid content.

The information on diffusion coefficients was obtained from measurements of concentration profiles by SIMS using the technique first employed on a-Si:H by Carlson and Magee[94]. The deuterium in the middle layer diffuses into the top and bottom layers and its profile was measured by SIMS. The information on the bonding configuration was monitored by Infrared absorption measurements.

IR spectra were taken before and after each annealing cycle in order to follow the peak positions and amplitudes of the bonding configuration. The IR stretch band of all a-Si:H studied in this work showed a single narrow peak at 2000 cm^{-1}, with a negligible tail at 2100 cm^{-1}, indicating almost

exclusive bulk-like mono-H bonding configurations.[84] The total Si-bonded H content C_H was determined from the 640 cm^{-1} wagging mode. It should be noted that C_H remained constant throughout all of the annealing steps, except following annealing of gd sample B for 8 hours at 360 °C.

The deuterium SIMS profiles for as-deposited rf sp sample A and gd sample B are shown in Figs. 4.1 and 4.2, respectively. Note that the interfaces were sharp since the substrate temperature was low during the deposition. Figs. 4.3 and 4.4 are deuterium depth profiles for samples A and B after annealing for different time periods. Clearly, the interfaces became smeared as the annealing time increased. After carefully choosing the interface positions, the fits were always good and usually excellent. The diffusion distance L taken for the measurement was typically 300 - 1500 Å. Longer distances would require prolonged annealing, which might cause complicated effects,[95] while shorter distances would fall below the limited spatial resolution of SIMS. Also, only values of L which did not require the extrapolation of the data points were included as the slope of $\log_{10}\theta(t)$ vs $\log_{10}t$ may change following prolonged annealing.[95]

B. Results and Discussion

The values of $\theta(t)$ (see eqs. 4.4 and 4.6) in rf sputtered sample A, where $C_H \simeq 2$ at.%, are shown in Fig. 4.5. Similar

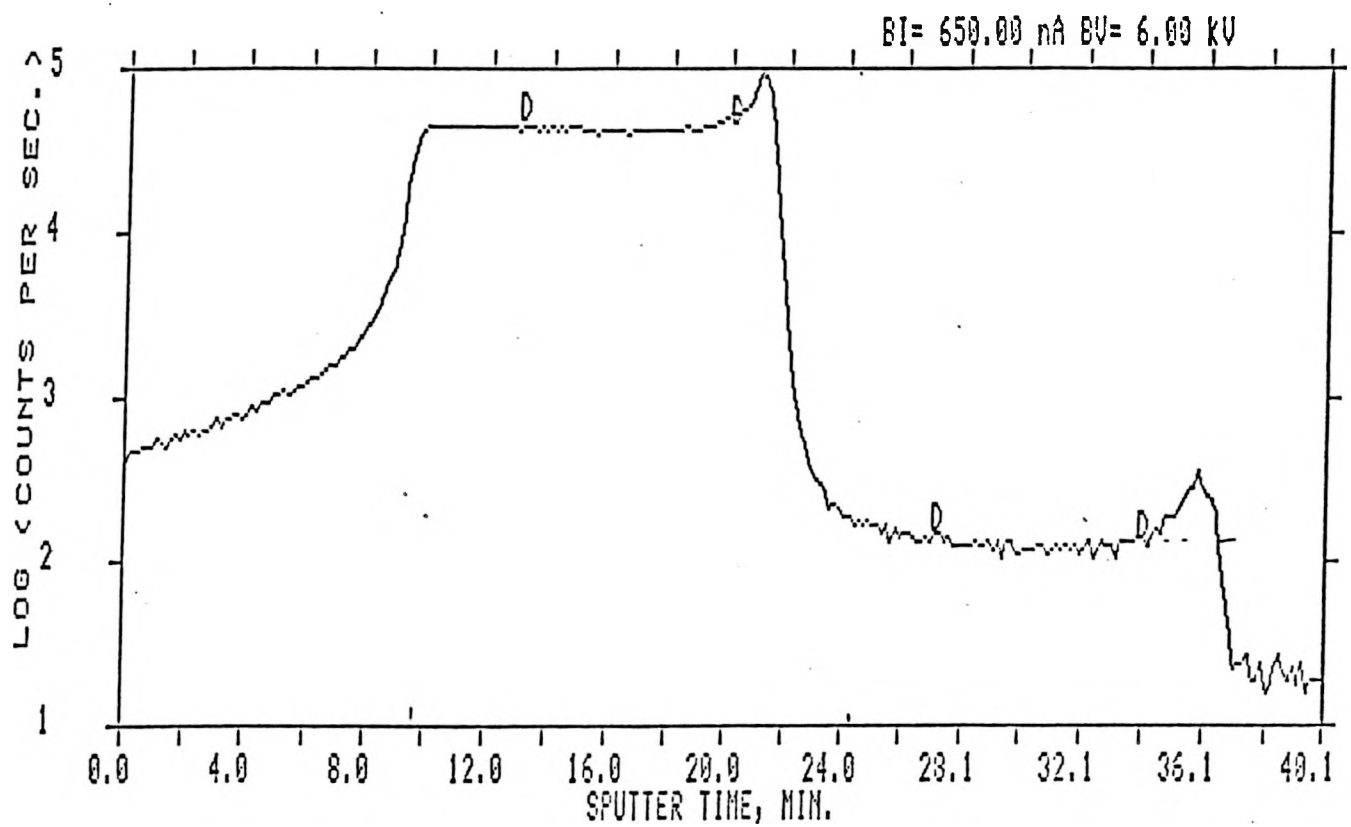

Fig. 4.1 Deuterium SIMS profile of as-deposited rf sputter-deposited sample A

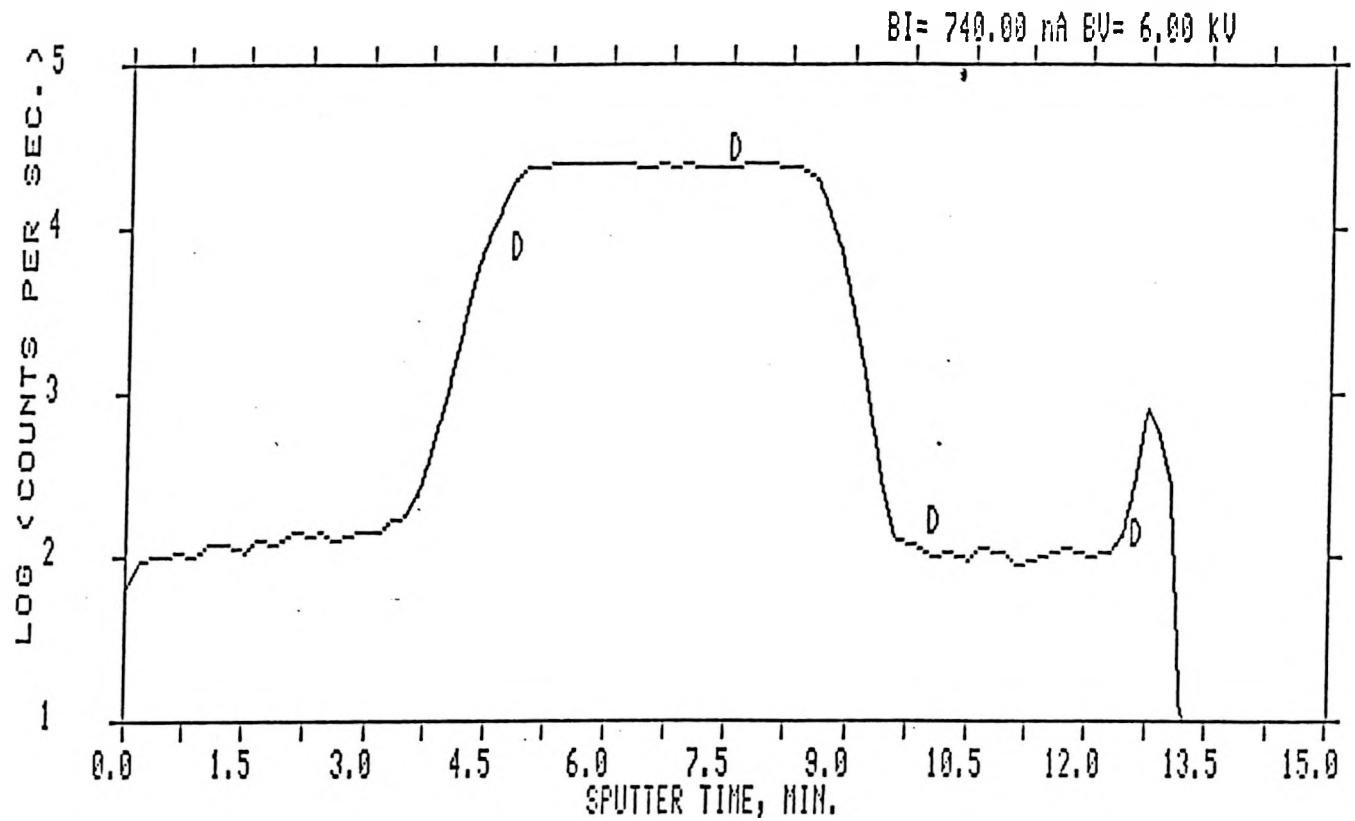

Fig. 4.2 Deuterium SIMS profile of as-deposited gd sample B

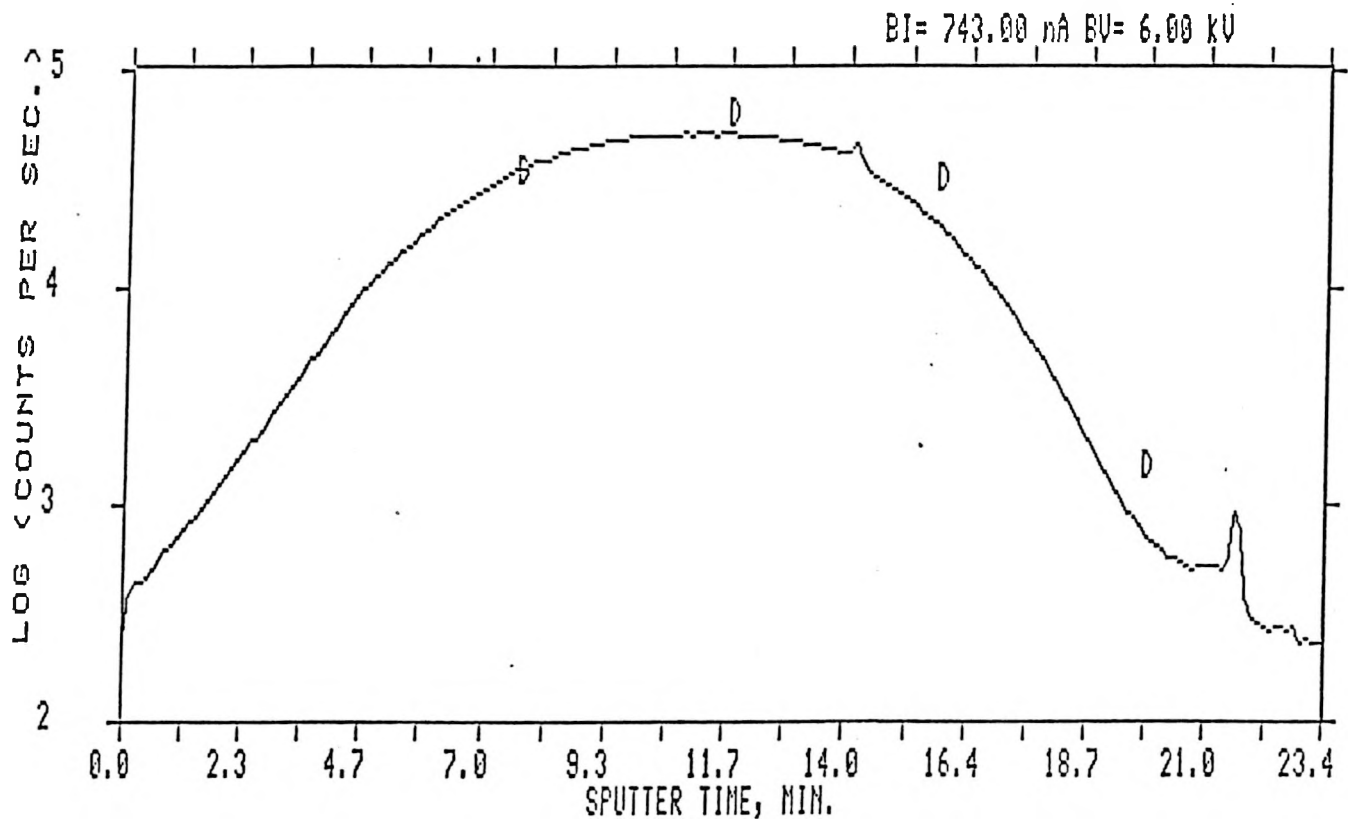

Fig. 4.3 Deuterium SIMS profile of sample A annealed at 400 °C for 24 hours

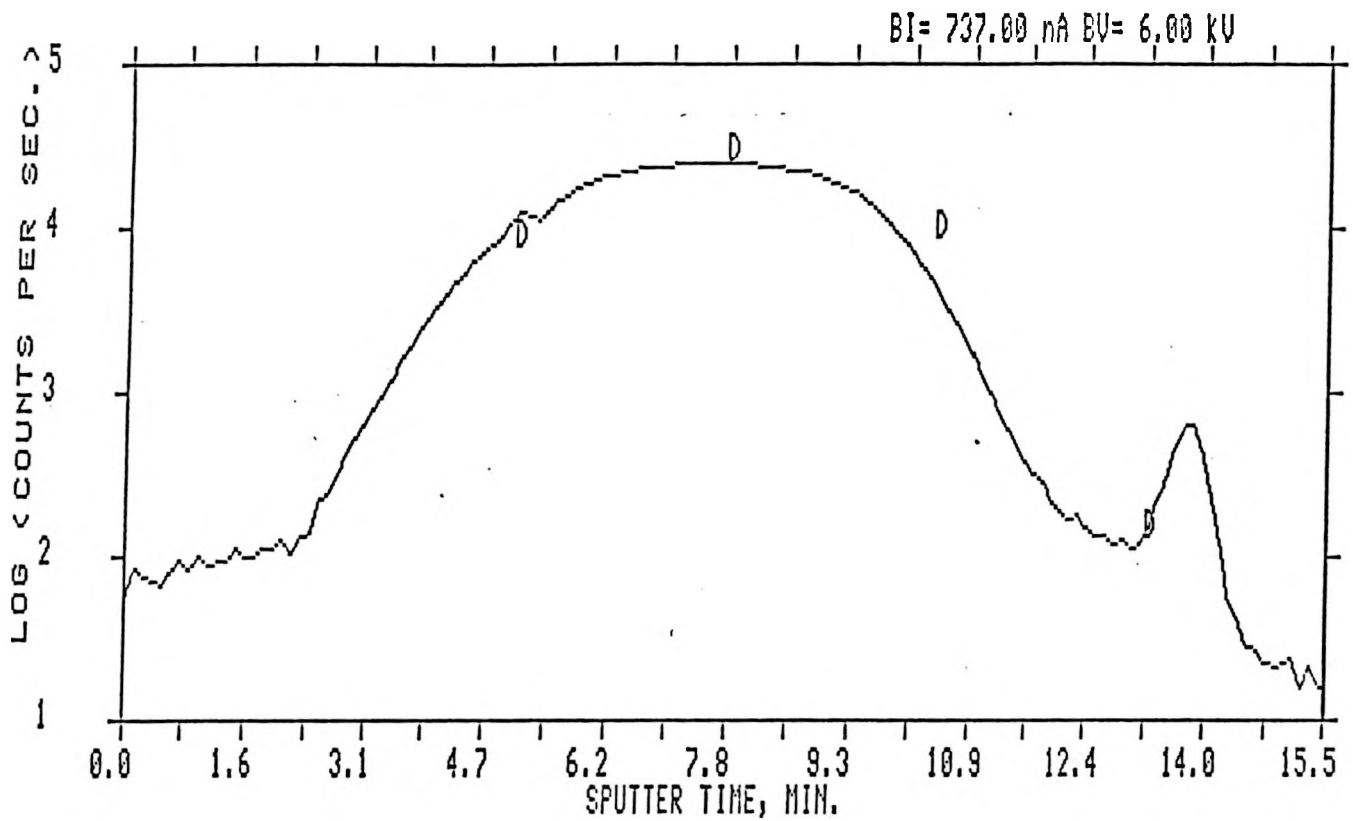

Fig. 4.4 Deuterium SIMS profile of sample B annealed at 360 °C for 1 hour

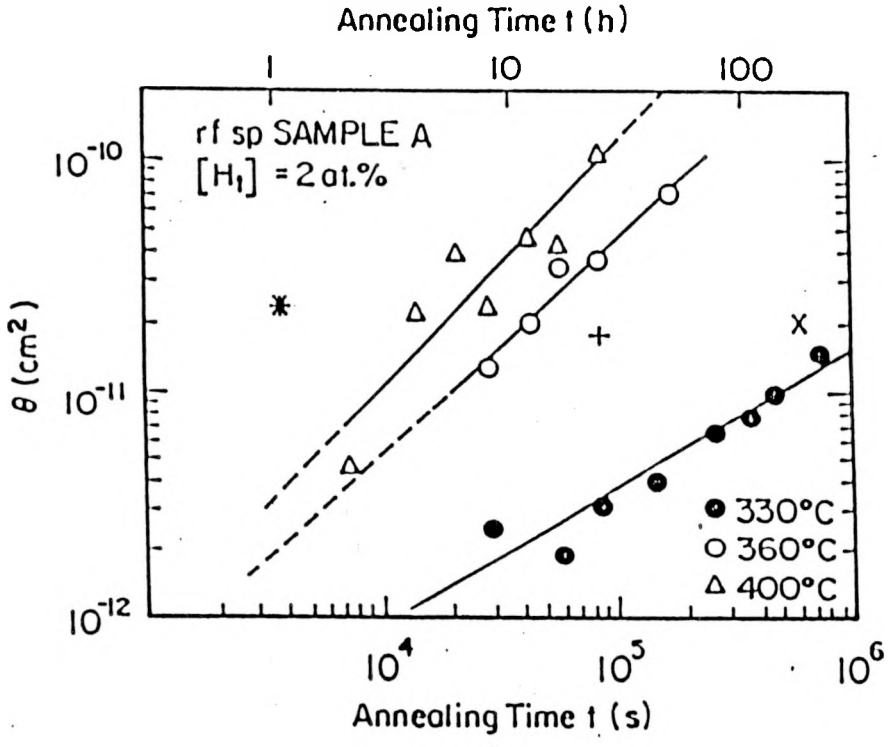

Fig. 4.5 Values of θ vs annealing time t, in rf sputter-deposited sample A. The values at 346 °C have been omitted to avoid clutter. The values of Dt, as measured by Carlson and Magee (Ref. 93) at 250 °C (x), 300 °C (+), and 350 °C (*), are also shown for comparison

results on gd sample B, where $C_H \simeq 9\pm1$ at.%, are shown in Fig. 4.6. The values of Dt in undoped a-Si:H, as first measured by Carlson and Magee (CM),[94] are also shown for comparison. As clearly seen, the diffusion in sample B is slightly slower than that measured by CM. The diffusion in rf sputtered sample A, however, is ~ 20 times slower at 350 °C, and no diffusion was observable at 300 °C. The measurements on sample A were thus restricted to the narrow temperature range of 330 - 400 °C.

The straight lines drawn in Figs. 4.5 and 4.6 are linear best fits of the data points to eq. 4.7. The values of α in samples A and B, at the various temperatures, are given in Table 4.1. The error in α is ± 0.1. We note that the error bars and scatter in the measurements of α as reported by others[61,62] and in a previous study by our group[63] are similar. The values of T_o resulting from eq. 1.3 are also given. As clearly seen, α generally decreases with increasing temperature, except in gd sample B at 360 °C (see below). Its behavior, however, is obviously at variance with eq. 1.3, beyond the experimental error, as seen from the varying values of T_o.

The diffusion constant

$$D(t) = \theta_o(1-\alpha)t^{-\alpha} \qquad 4.15$$

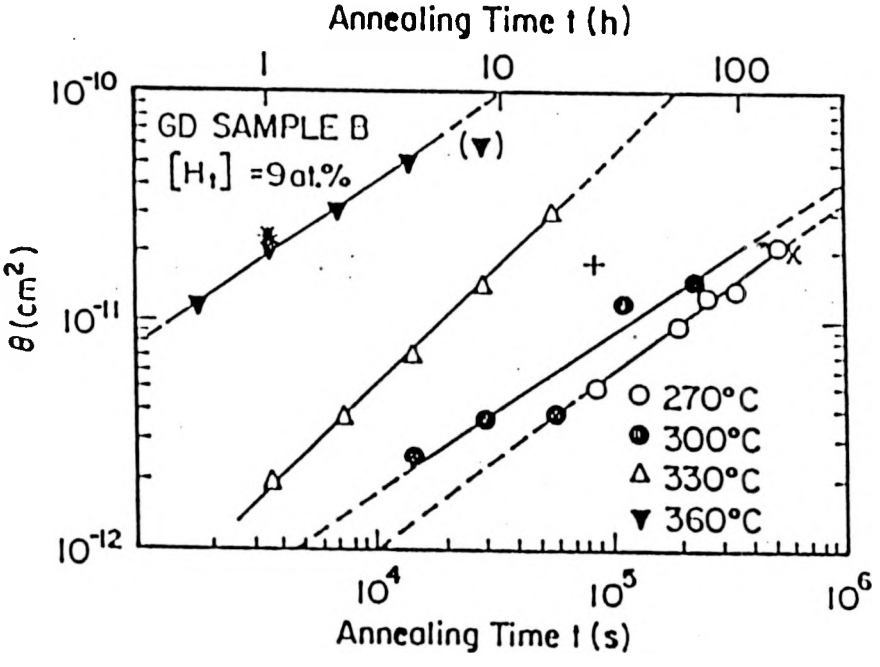

Fig. 4.6 Values of θ [see Eqs. 4.6 and 4.7] vs annealing time t, in glow-discharge sample B. For additional details see caption of Fig. 4.6. The value of θ following annealing for 8 h at 360 °C is given in parenthesis, since some of the hydrogen had evolved out of the film during that annealing

Table 4.1 The values of α, resulting T_o, and θ_o at the various annealing temperatures T in the rf sputter-deposited sample A (Fig. 4.5) and glow discharge deposited sample B (Fig. 4.6)

T (°C)	α (±0.1)	T_o (K)	θ_o ($cm^{-1}/sec^{1-\alpha}$)
		rf sp sample A	
330	0.39	990	3.3×10^{-15}
346	0.34	940	2.7×10^{-15}
360	0.07	680	9.9×10^{-16}
400	~ 0.0	670	7.2×10^{-16}
		GD sample B	
270	0.22	700	7.5×10^{-16}
300	0.32	840	3.5×10^{-15}
330	~ 0.0	600	5.3×10^{-16}
360	0.30	900	6.4×10^{-14}

in samples A and B was determined from the time derivatives (see eq. 4.7) of the $\theta(t)$ vs t lines shown in Fig. 4.7. The argument[64] that $D(t_L)$ (see eq. 4.10) is the quantity to be monitored as a function of T, is independent of the behavior of the dispersion parameter α. It simply means that the diffusion of the deuterium in a constant volume of the film (determined by L) is being monitored at different temperatures. Thus, if the diffusion process is activated and $\alpha = 1 - T/T_o$, then $D(t_L)$ vs $1/T$ should indeed yield E_a and D_o. Yet this is true only if the set of sites available for deuterium occupation is constant during this process. If, on the other hand, structural relaxation and defect generation processes occur, they modify the sites at different rates at different temperatures. Then the barrier heights for H motion cannot be determined or the activation energy should be interpreted to include quantities involved in these other processes. Indeed, evidence for effects of structural relaxation on diffusion in boron-doped multilayers annealed over prolonged periods of time were observed by deuterium SIMS profiles.[95] Roorda et al.[96] reported their differential scanning calorimetry observation of structural relaxation of a-Si. In addition, very recent elastic recoil detection analysis results of Tang et al.[97] show that in undoped gd a-Si:H, α <u>increases</u> with increasing T above 350 °C, and strongly so between 380 °C and 470 °C. These results are suspected to

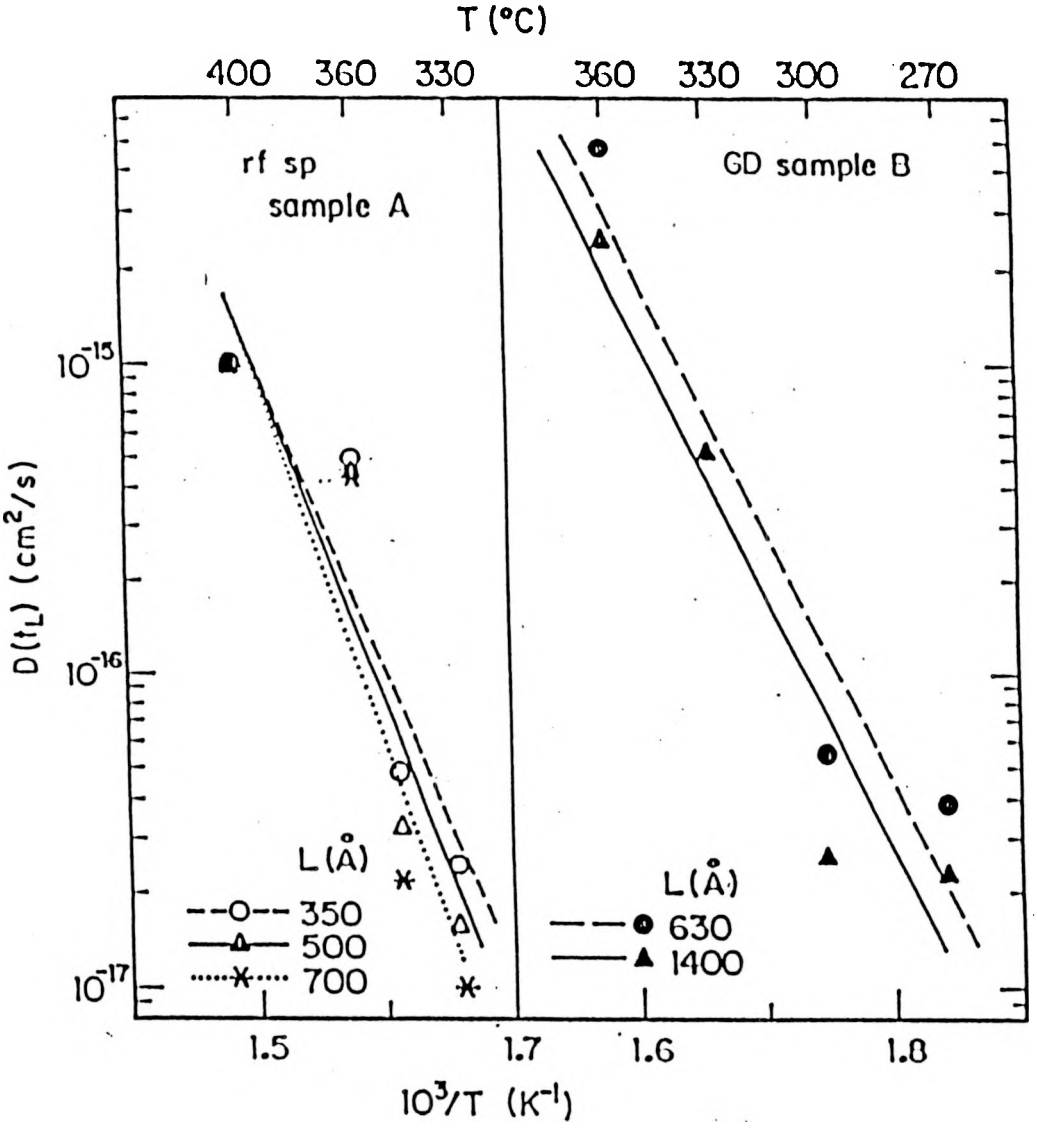

Fig. 4.7 Diffusion constant for constant diffusion length L, $D(t_L)$, vs the inverse temperature 1/T. Since the exponent α does not depend on T as $1-T/T_o$, $\ln D(t_L)$ is not linear in 1/T. The straight lines, determined by the linear best fits of the data, define "apparent" activation energies E_a and prefactors D_o, which clearly increase with L in the rf sp sample A

result from thermal defect generation and/or structural relaxation processes. We thus presently suspect that below 400 °C, deuterium motion actually proceeds mostly by thermally activated hopping out of multiple trapping sites, but structural relaxation and/or defect generation processes also occur. These processes would obviously affect the behavior of α, which would thus no longer depend on T as $1 - T/T_o$. As a matter of fact, even in the absence of structural relaxation and thermal defect generation processes, a $1 - T/T_o$ dependence would be expected only if the distribution of sites is exponential.[98] The observed departure of α from $1 - T/T_o$ may thus also be due to a nonexponential distribution.

The validity of the subsequent analysis of $D(t_L)$ vs 1/T is thus subject to the relative contributions of the activated hopping and structural processes in determining α. Since α does not obey eq. 1.3, E_a as determined from $D(t_L)$ is not independent of T (see eq. 4.13). Fig. 4.7 shows that for rf sputtered sample A and L = 350, 500, and 700 Å, $\ln D(t_L)$ is curved when plotted vs 1/T. "Apparent" values of E_a and D_o were then defined from the linear best fits of $\ln D(t_L)$, for constant $L = 2\sqrt{\theta}$, vs 1/T (Fig. 4.7). The apparent E_a and D_o in the rf sputtered film containing 2 at.% H strongly increase with L. This is a direct consequence of the sharp drop in α from 0.39 at 330 °C and 0.34 at 346 °C to ~0.07 at 360 °C and ~0 at 400 °C. The values of E_a and D_o are summarized in Table

4.2. They are also significantly larger than those in the gd film containing 9 at.% H (~ 1.65 eV) or a microvoid-rich rf sputtered film containing 18 at.% H previously studied (~ 1.3 eV).[63] This is obviously consistent with the observation that H diffusion in rf sputtered sample A is much slower than in the other samples. Note that the values of θ following annealing for 8 and 16 hours at 330 °C somewhat deviate from the linear best fit line. If these two data points are ignored, $\alpha \simeq 0.28$. When L increases from 350 to 700 Å, E_a and D_o then increase from 1.9 eV and 0.3 cm^2/s to 2.4 eV and 1600 cm^2/s, respectively. There is, however, no justification for ignoring any of these points. They both show clear smearing relative to the as-deposited film, although the smearing is similar for the two periods. This behavior is consistent with the relatively large value of α, which is also observed at 346 °C. The profile following annealing for 8 hours at 330 °C should exhibit a value of θ that is smaller by a factor of 2 to fit the line yielding $\alpha \simeq 0.28$. This deviation is beyond the error in the fitting procedure.

The obvious correlation between D_o and E_a seen in Table 4.2 should be viewed with caution. The differences between the samples, and in particular the slower diffusion in the film containing 2 at.% H, are believed to be significant. Yet the change of E_a and D_o with L in the latter is not well established experimentally, and may be subject to the

Table 4.2 The values of the "apparent" activation energy E_a and prefactor D_o, defined by the linear best fits of $\ln D(t_L)$ vs $1/T$, in rf sputter-deposited sample A and glow discharge sample B

L (Å)	E_a (eV)	D_o (cm^2/s)
	rf sputtered sample A	
300	1.94	0.48
500	2.18	33
700	2.44	3100
	GD sample B	
630	1.65	0.033
1400	1.67	0.044

criticism raised by Kirchheim and Huang.[91] In any case, however, Fig. 4.8 shows that this correlation extends to the rf sputtered samples containing ~18 at.% H and a significant microvoid content, described previously.[63] As clearly seen, it spans 8 orders of magnitude in D_o, as C_H increases from 2 to 18 at.%, and E_a and D_o decrease from 2.4 eV and 3100 cm^2/s to 1.3 eV and 2×10^{-5} cm^2/s, respectively. The values of $A_{oo} \simeq 3.1\times10^{-14}$ cm^2/s and slope $1/T_o'$ yielding $T_o' \simeq 730$ K are close to the predictions of the MT model, in which $D_{oo} \simeq 2\times10^{-15}$ cm^2/s and $T_o \simeq 650$ K.[64] Figure 4.8 thus suggests that hydrogen motion in virtually all undoped a-Si:H films obeys the MNR with these values of A_{oo} and T_o', regardless of microstructure, H content, or diffusion length.

Results on phosphorus-doped films from Ref. 64 are also inserted in Fig. 4.8. Their deviation from the MNR is in agreement with the role of band-tail carriers advanced by Jackson.[64,65] in enhancing H motion.

As mentioned above, Kirchheim and Huang[91] question the significance of the MNR when it results from the motion of the same atom in a varying matrix. Yet when the values of E_a and D_o were calculated for constant annealing times, clear deviations from the MNR appeared: Although a similar relation indeed exists for various annealing times in rf sputtered sample A, the values of D_o in gd sample B are too large by a factor of ~ 10 - 15. The deviations of D_o in the microvoid-

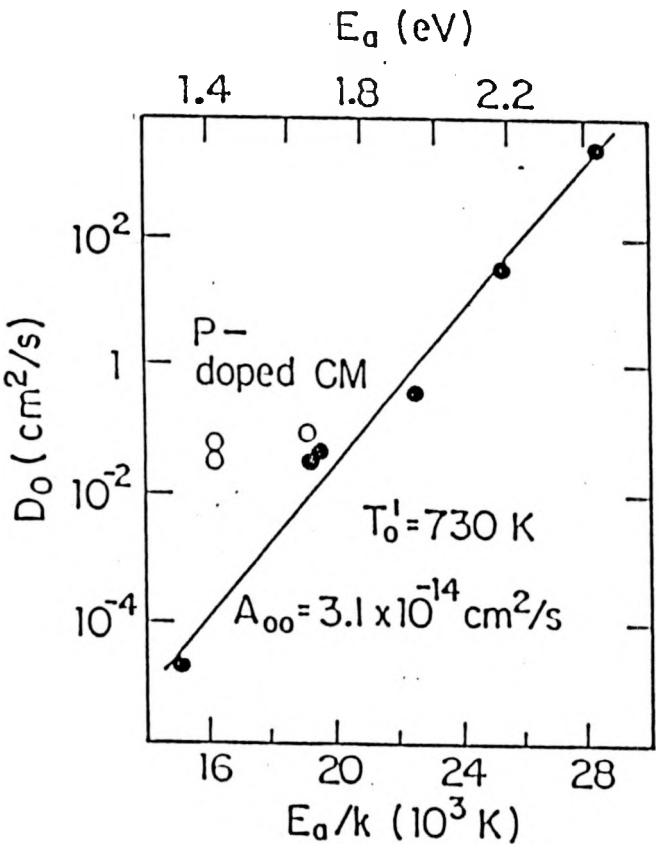

Fig. 4.8 The apparent prefactor D_o vs the apparent activation energy for H diffusiom E_a/k, in various undoped hydrogenated amorphous silicon films. These include (i) rf sp sample A, of initial H content C_{Ho} = 2 at.%, for diffusion lengths L=350, 500, and 700 Å (see table 4.2); (ii) gd sample B, where C_{Ho} ~ 9 at.%, for L=630 and 1400 Å; (iii) the sample studied by Carlson and Magee (CM; see Ref. 94), uncorrected for the time dependence of the diffusion constant (C_{Ho} ~ 10 at.%), and (iv) a microvoid-rich rf sp sample with C_{Ho} ~ 18 at.% (Ref. 63). Note that the value of D_o in some phosphorus-doped films, obtained from Ref. 64, are ~ 30 times higher than the corresponding undoped film of similar H content

rich rf sputtered sample of $C_H \sim 18$ at.% are much more impressive. In that sample, D_o is $\sim 10^6$ smaller than expected. It is thus suspected that the major process contributing to H motion is still thermally activated detrapping in the time and temperature range under consideration. The relatively slower diffusion with a strongly increased apparent E_a at low H content is then in qualitative agreement with a roughly exponential distribution of site energies: The hydrogen would then be primarily occupying the deep sites at the tail of this distribution.

The behavior of α obviously deserves special attention. Although it was observed to be very high (~ 0.75) in microvoid-rich rf sputtered films,[63] its dependence on microstructure in gd a-Si:H has only recently been determined. Tang et al.[97,99] have shown that α clearly increases as the deposition temperature T_s decreases. Since the microvoid content increases with decreasing T_s,[92] this result is in qualitative agreement with the results on the rf sputtered films.[63] As previously mentioned, they have also observed that in gd films deposited at $T_s \simeq 150$ °C, α increases slightly from 350 to $\sim$ 380 °C, and very strongly from $\sim$ 380 to 470 °C.[100] The increased value of $\alpha \simeq 0.3$ in gd sample A at 360 °C may be related to this behavior. Other measurements on boron-doped a-Si:H following prolonged annealing at 180 and 225 °C yield a complex dependence of α on annealing time.[95] That behavior is

consistent with structural relaxation that leads to changes in the doping efficiency.[101] All of these results indicate that structural relaxation and defect generation and/or annealing processes are not negligible at temperatures above 300 °C in undoped and 180 °C in doped films. Recent specific heat measurements of Roorda et al.[96] and magic angle ^{29}Si NMR of Shao et al.[102] on unhydrogenated a-Si also point to structural relaxation at relatively low temperatures. The results described in this work therefore clearly show that processes other than thermally activated detrapping contribute to, or inhibit, H motion in undoped a-Si:H above 300 °C. The apparent E_a and D_o calculated above thus provide only rough estimates of the true activation energies and prefactors in undoped a-Si:H.

The MT model treated by Jackson[64] yields $T_o' = T_o$. Indeed, in all cases except that of the microvoid-rich rf sputtered film, $600 \leq T_o < 1000$ K (see Table 4.1). That rf sputtered film, however, yielded $T_o \simeq 2300$ K.[63] It is believed that microvoid-rich films contain a significant density of deep traps, which render immobile H an D. These yield very high values of α and T_o.[63,97,99] Yet the values of E_a and D_o for constant diffusion length are determined by the mobile H and D. They would therefore be expected to obey the MNR relevant to the mobile atoms, with an unrelated slope yielding $T_o' \simeq 730$ K.

In spite of its importance, the nature of the microvoid-related traps has not been settled. As mentioned above, it was previously shown[63] that an excessive microvoid content suppresses long-range H motion in undoped rf sputtered films, even when a large fraction of the hydrogen remains bonded in a "bulk-like" mono-H configuration as evidenced by a significant stretch peak or shoulder at $\simeq$ 2000 cm^{-1}.[84] It therefore appeared that the deep microvoid-related traps are not located at the microvoid surfaces. Recent suggestions, however, propose that hydrogen bonded in a mono-H configuration at the surface of small, anisotropic and highly compressed (i.e., opposite surfaces only $\simeq$ 3 Å apart) microvoids will experience a dielectric screening similar to that in the bulk.[85] It will consequently vibrate at 2000 cm^{-1}, similar to isolated mono Si-H bonds embedded in the bulk. Small clusters of hydrogen bonded in a mono-H configuration at such compressed microvoids will then contribute to the broad proton NMR component.[103] Preliminary proton NMR measurements indeed indicate that annealing of rf sputtered films, including those prepared under conditions in which long-range H motion is suppresed, results in a sharp reduction of the narrow component following annealing.[104] It is therefore suspected that the microvoid-related deep traps are indeed mono Si:H configurations at microvoid surfaces. This scenario suggests that rearrangement of Si-Si bonds adjacent to a bonded hydrogen, which is

apparently interrupted in the presence of microvoids, may be necessary for H motion.

V. RESULTS ON UNDOPED a-Ge:H

A. Introductory Comments

Hydrogen diffusion and desorption in a-Si:H have been extensively studied.[61,62,63,86,95,97,105,106] The motivation for these studies has been the suspicion that H motion is involved in metastable defect generation and annealing processes. Although a-Ge:H is a closely related system to a-Si:H, only preliminary studies of H diffusion and desorption in a-Ge:H have been reported.[106,107] We studied hydrogen diffusion and desorption in a variety of rf sputter-deposited a-Ge:H films and compared the results to the behavior of a-Si:H.

The results on a-Si:H in the last chapter show that H diffusion is significantly slower at low H content. At $C_H \sim 2$ at.%, α was clearly observed to decrease with temperature, although its behavior did deviate from eq. 1.3. Experiment also showed that long-range H motion is suppressed as the microvoid density exceeds a critical value.[63] It is consequently suspected that there are two types of Si-bonded H sites in a-Si:H: A set of MT sites roughly exponentially distributed in energy, and deep monohydride sites on microvoid surfaces. The latter render the hydrogen essentially immobile at temperatures below 350 °C, and perhaps up to ~ 475 °C, where diffusion-limited desorption of bulk hydrogen commences.[105]

As mentioned above, preliminary results on long-range H

motion and desorption in rf sp a-Ge:H have been reported.[106] In addition, Beyer et al.[107] performed measurements of H diffusion and desorption in gd a-Ge:H filmes prepared under conditions similar to those of device-quality a-Si:H. Films of varying microstructure were obtained by varying the deposition temperature T_s in the 50 - 350 °C range. The calculated activation energy of H diffusion was $E_a \simeq 1.5$ eV, similar to values obtained in a-Si:H.[61-63,86,106] They also reported that hydrogen desorbed from films deposited at low T_s ($\leq$ 150 °C) below 200 °C, in spite of the absence of long-range H motion in the bulk of the film, as measured by SIMS.

Studying the behavior of H motion in a-Ge:H system is thus highly desirable. Both the similarity and difference when comparing with that in a-Si:H will offer insight to the defect dynamics and hopefully to the problem of metastability in general.

Since the films were deposited on polished Si wafers, the intensity of the GeH_2 scissors (bending) mode absorption at 780 cm^{-1} was much weaker than the interference fringes in the IR spectra, as shown in Fig. 3.9. It was thus impossible to determine the dihydride and trihydride content of the films.

In order to check the level of C, N, and O impurities in the films, the Auger spectra of some of the films was measured. Thus, sample 7 contained ~0.1 at.% C, but no measurable (i.e., less than ~0.05 at.%) amounts of N or O. On

the other hand, sample 1 contained ~0.7 at.% O, but no measurable amounts of C or N. The presence of C, N, or O could not be correlated with hydrogen diffusion as monitored by the deuterium SIMS profiles.

B. Results and Discussion

The behavior of θ as a function of annealing time t, at various temperatures, in four films which initially contained 5.0 - 9.5 at.% hydrogen, is shown in Figures 5.1 - 5.4. As clearly seen, the behavior of θ generally follows eq. 4.7. The values of α, θ_o, and T_o (see eq. 1.3) resulting from the linear best fit of $\log\theta(t)$ vs $\log t$ to the data in Figs. 5.1 - 5.4 are listed in Table 5.1. The initial Ge-bonded H content C_{Ho} and the content following annealing C_H are also listed. The reduction in C_H during annealing due to desorption is obvious. We note that except for evolution of H from SiH_2 and SiH_3 bonding configurations during the initial annealing step, none occurred in a-Si:H during consecutive annealing steps at temperatures below 360°C. The desorption of hydrogen from a-Ge:H during the annealing should obviously be taken into account in the analysis of the other results.

The values of α clearly do not show any dependence on T in the measured range. In other words, they do not appear to obey eq. 1.3. Equivalently, the values of T_o calculated from the experimental values of α and eq. 1.3 generally appear to

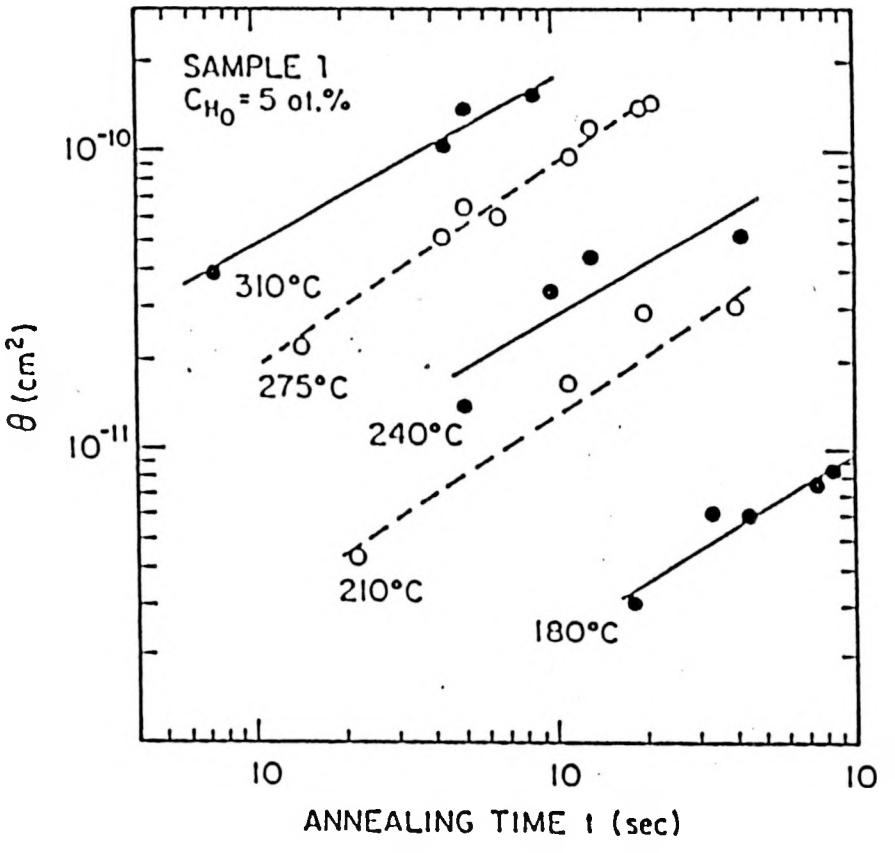

Fig. 5.1 The values of θ in sample 1, as a function of the annealing time t at 180 ≤ T ≤ 310 °C. While the as-deposited Ge-bonded H content of the film was 5.0 at.%, it gradually decreased to 2.8 at.% during progressive annealing steps (see Table 5.1)

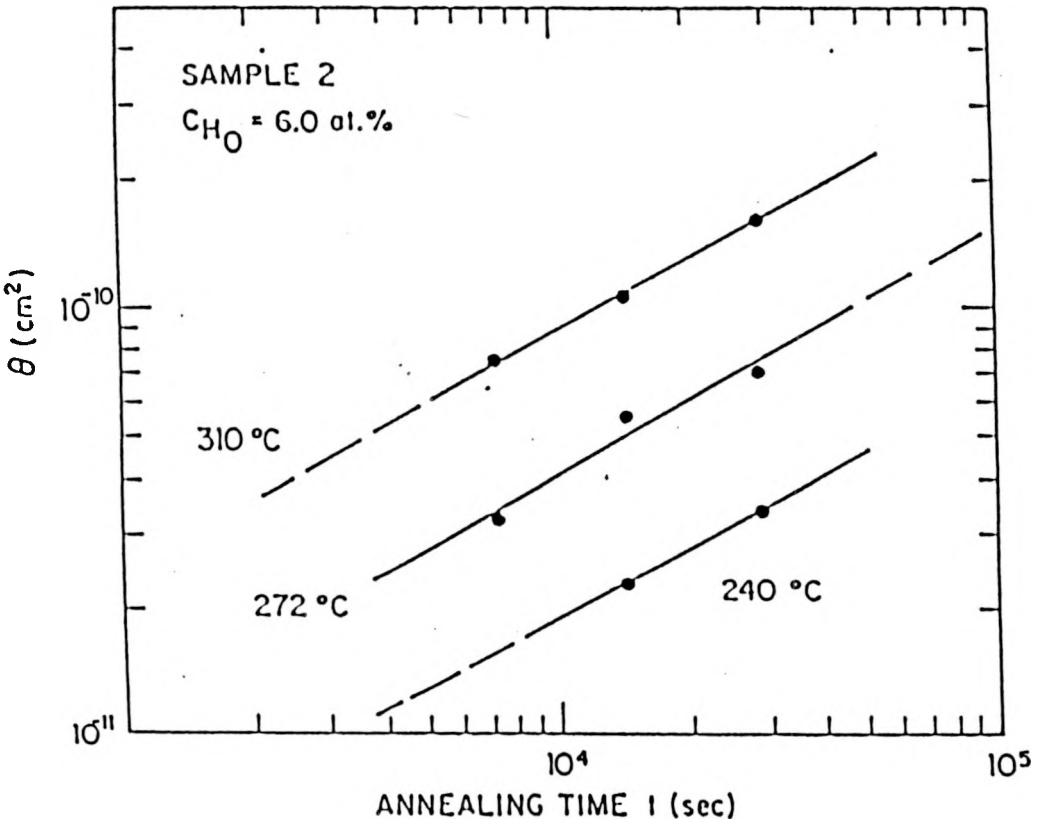

Fig. 5.2 The values of θ in sample 2, as a function of the annealing time t at $240 \leq T \leq 310$ °C. While the as-deposited Ge-bonded H content of the film was 6.0 at.%, it gradually decreased to 4.2 at.% during progressive annealing steps (see Table 5.1)

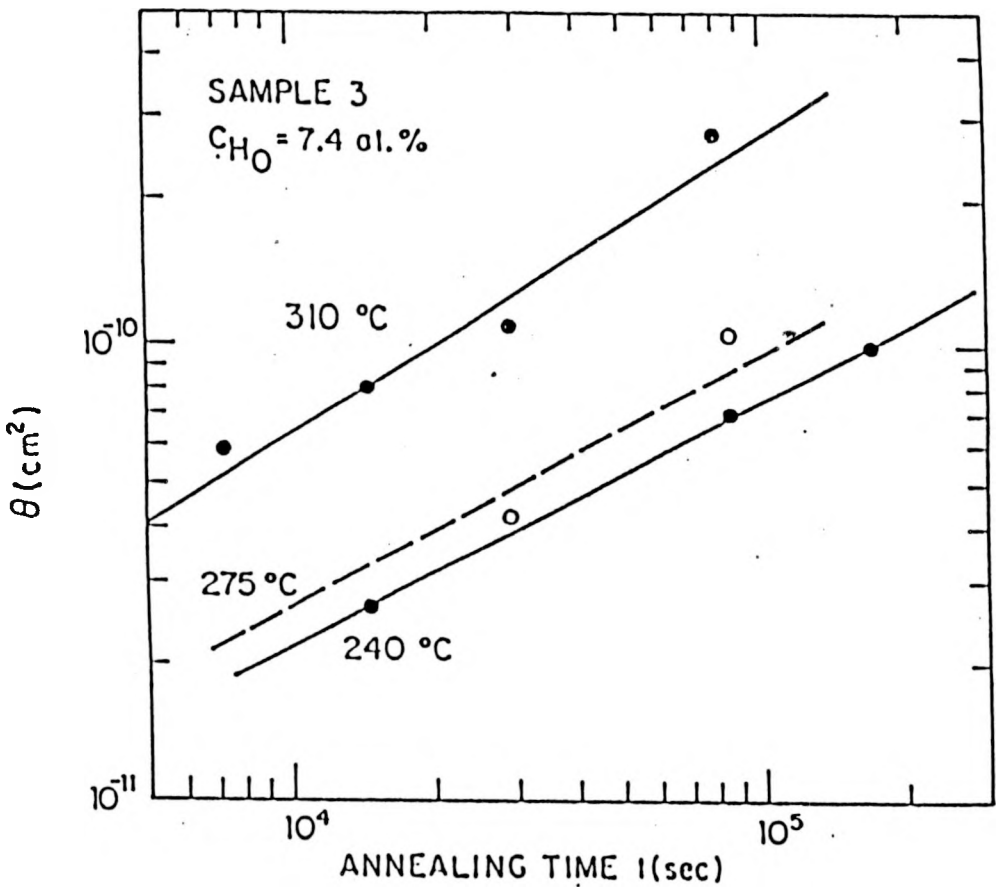

Fig. 5.3 The values of θ in sample 3, as a function of the annealing time t at 240 ≤ T ≤ 310 °C. While the as-deposited Ge-bonded H content of the film was 7.4 at.%, it gradually decreased to 3.2 at.% during progressive annealing steps (see Table 5.1)

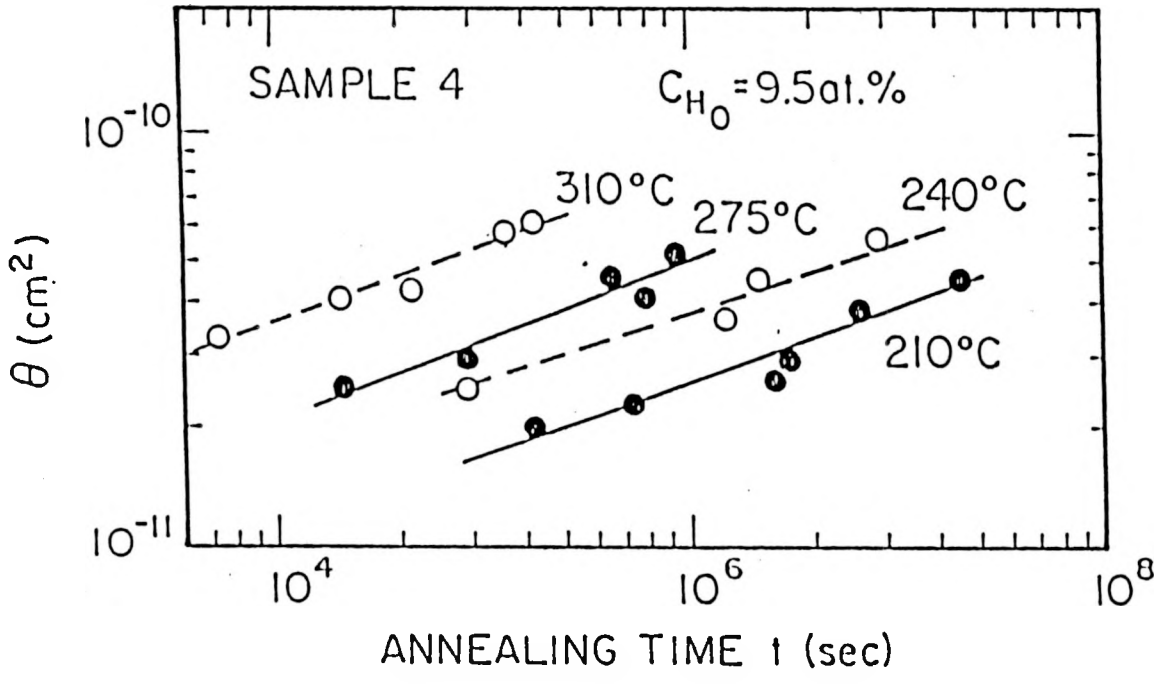

Fig. 5.4 The values of θ in sample 4, as a function of the annealing time t at 210 ≤ T ≤ 310 °C. While the as-deposited Ge-bonded H content of the film was 9.5 at.%, it gradually decreased to 3.5 at.% during progressive annealing steps (see Table 5.1)

Table 5.1 The values of the dispersion parameter α and prefactor θ_o resulting from fitting eq. 4.7 to the experimental values of θ shown in Figs. 5.2 - 5.5. The initial Ge-bonded H content C_{Ho} (±0.5 at.%), H content after annealing C_H (±0.5 at.%), and the value of the characteristic temperature T_o of the multiple trapping model (eq. 1.3) are also listed

Sample	C_{Ho} (at.%)	T(°C)	C_H (at.%)	α (±0.1)	θ_o (cm²)	T_o (K)
1	5.0	180	3.5 - 2.3	0.39	2.2×10^{-15}	740
		210	3.1 - 2.3	0.33	6.1×10^{-15}	720
		240	4.2 - 3.1	0.42	3.5×10^{-14}	885
		275	4.1 - 3.7	0.31	3.2×10^{-14}	794
		310	2.9	0.43	2.5×10^{-13}	1020
2	6.0	240	5.2 - 4.9	0.43	1.1×10^{-13}	900
		272	5.0 - 4.6	0.44	2.3×10^{-13}	970
		310	5.0	0.44	5.0×10^{-13}	1040
3	7.4	240	6.5 - 5.7	0.47	1.6×10^{-13}	970
		275[a]	7.0 - 6.2	(0.45)	(1.7×10^{-13})	
		310	6.5 - 3.2	0.36	1.8×10^{-13}	910
4	9.5	210	4.2	0.65	4.3×10^{-13}	1380
		240	4.9 - 4.1	0.68	9.0×10^{-13}	1600
		275	4.0 - 2.8	0.62	6.6×10^{-13}	1440
		310	3.5 - 3.0	0.65	1.4×10^{-12}	1670

[a] The values are listed in parenthesis since the line drawn in Fig. 5.4 was determined by interpolating the values of θ_{oo} at 240 °C and 310 °C and the two points measured at 275 °C.

increase with T rather than remain constant. This deviation from eq. 1.3 is most striking in sample 1 (Fig. 5.1), in which measurements were performed over the widest temperature range (180 - 310 °C). In analyzing this behavior, one may initially suspect that the decrease in C_H affects the observed values of α. Indeed, a diffusion constant that decreases with C_{Ho} or C_H (as in a-Si:H)[86] would then yield an α which is greater than at constant C_H. Yet $D(t_L)$ is similar among samples 1, 2, and 3 (see Table 5.2 and below). It is therefore believed that a different scenario is responsible for the temperature dependence of α (see below).

With the exception of sample 4, α does not exhibit a dependence on C_H either (see Table 5.1). Its value is considerably higher (~ 0.65), however, in that sample, which contained 9.5 at.% hydrogen when deposited, only 4.9 at.% or less during annealing. In a-Si:H, the initial desorption primarily involves hydrogen from SiH_2 and SiH_3 configurations,[108] which are usually associated with microvoids.[63,84,108] It is thus suspected that the microvoid content of sample 4 was considerable, and largely responsible for the high value of α. This conjecture is in excellent agreement with the existing results on a-Si:H, where microvoids have indeed shown to contribute to a large value of α.[63,97] In light of the temperature independence of α in all of the samples studied in this work, it is believed that their

Table 5.2 The values of the diffusion constant $D(t_L)$ for 900 $\leq L \leq$ 2000 Å, as determined from the values of θ shown in Figs. 5.2 - 5.5 and eqs. 4.7, 4.8 and 4.10

Sample	C_{Ho} (at.%)	T (°C)	C_H (at.%)	$D(t_L)$ (cm^2/s), L = 900 Å	1200 Å	1500 Å	2000Å
1	5.0	180	3.5-2.3	3.9×10^{-18}		2.1×10^{-18}	
		210	3.1-2.3	6.8×10^{-17}		4.2×10^{-17}	
		240	4.2-3.1	2.0×10^{-16}		9.9×10^{-17}	
		275	4.1-3.7	1.2×10^{-15}		7.8×10^{-16}	
		310	2.9	5.3×10^{-15}		2.4×10^{-15}	
2	6.0	240	5.2-4.9		6.2×10^{-16}	4.3×10^{-16}	2.7×10^{-16}
		272	5.0-4.6		2.5×10^{-15}	1.8×10^{-15}	1.1×10^{-15}
		310	5.0		9.6×10^{-15}	6.8×10^{-15}	4.3×10^{-15}
3	7.4	240	6.5-5.7		7.2×10^{-16}	5.0×10^{-16}	2.9×10^{-16}
		275	7.0-6.2		1.2×10^{-15}	7.9×10^{-16}	5.0×10^{-16}
		310	6.5-3.2		5.6×10^{-15}	4.1×10^{-15}	3.1×10^{-15}
4	9.5	210	4.2	1.4×10^{-16}		2.3×10^{-17}	
		240	4.9-4.1	4.5×10^{-16}		5.0×10^{-17}	
		275	4.0-2.8	8.4×10^{-16}		1.5×10^{-16}	
		310	3.5-3.0	3.7×10^{-15}		5.5×10^{-16}	

role is even more dominant in a-Ge:H. The subtle but important differences between monohydride sites on microvoid surfaces of the two networks are discussed later in this chapter.

The values of $D(t_L)$, for diffusion length L from 900 to 2000 Å, determined from Figs. 5.1 - 5.4 and eqs. 4.4 and 4.10, are listed in Table 5.2. As mentioned above, $D(t_L)$ does not exhibit a clear dependence on C_{Ho} or C_H among samples 1, 2, and 3. In contrast, it does decrease with C_H in a-Si:H.[86,109] For L = 900 Å, the values of $D(t_L)$ in sample 4 are similar to those of the other samples; the values of L = 1500 Å at 275 and 310°C, on the other hand, are distinctly lower than those of the other samples. This behavior obviously results from the strong dependence of $D(t_L)$ on L, i.e., due to the large value of α, in turn believed to result from an increased micvoid content.

The activation energies and prefactors, determined from the linear best fit of the values of $\log D(t_L)$ plotted vs 1/T (see eq. 4.11) are listed in Table 5.3. The values of E_a are clearly independent of L, again in contrast to the behavior expected from the MT model. The observed behavior is a direct mathematical result of the lack of dependence of α on T.

Since $\alpha > 0$ and E_a is independent of L, the decreasing value of $D(t_L)$ with increasing L is due to a decreasing prefactor D_o. The values of $E_a(L)$ and $D_o(L)$ therefore do not

Table 5.3 The activation energy E_a (±0.1 eV) and prefactor D_o for H diffusion lengths $900 \leq L \leq 2000$ Å, as determined from Table 5.2 and linear best fits of $\ln[D(t_L)]$ vs $1/T$. Note that E_a is essentially independent of L.

Sample	C_{H_o} (at.%)	L (Å)	E_a (eV)	D_o (cm^2/s)
1	5.0	900	1.21	1.7×10^{-4}
		1500	1.19	6.3×10^{-5}
2	6.0	1200	1.00	4.7×10^{-6}
		1500	1.01	3.7×10^{-6}
		2000	1.02	2.6×10^{-6}
3	7.4	1200	0.74	1.2×10^{-8}
		1500	0.76	1.2×10^{-8}
		2000	0.86	6.2×10^{-8}
4	9.5	900	0.75	9.7×10^{-9}
		1500	0.77	2.2×10^{-9}

obey the Meyer-Neldel relation (MNR; eqs 4.14 and 5.1 below) as a function of L within a given sample. This is obviously another manifestation of the inapplicability of the MT model to the experimental results. As clearly seen from the results on sample 1, 2, and 3, listed in Tables 5.1 and 5.3, however, E_a and D_o both decrease with increasing C_{Ho} or C_H. A similar trend has been observed in a-Si:H.[86] In contrast to the analysis of the results described above, this behavior is consistent with the MT model:[63,64,86] The average site visited by diffusing hydrogen is shallower the higher the H content. Due to the other inconsistencies with the MT model mentioned above, however, it is suspected that this agreement is fortuitous. The issue raised by Kirchheim and Huang[91] thus appears to be particularly appropriate to a-Ge:H (see below).

The correlation between the values of E_a and D_o among the different samples listed in Table 5.3 is obvious. Figure 5.5 shows the MNR

$$D_o = A_{oo}\exp(E_a/kT_o') \qquad 5.1$$

of D_o vs E_a. The values of T_o' and A_{oo} resulting from the linear best fit of E_a and D_o listed in Table 5.3 to eq. 5.1 are 530 K and 5.5×10^{-16} cm^2/s, respectively. Eqs. 1.2-1.4, 4.10, 4.11 and 4.14, however, predict that the value of T_o' resulting from eq. 5.3 should be equal to that calculated from eq. 1.3.

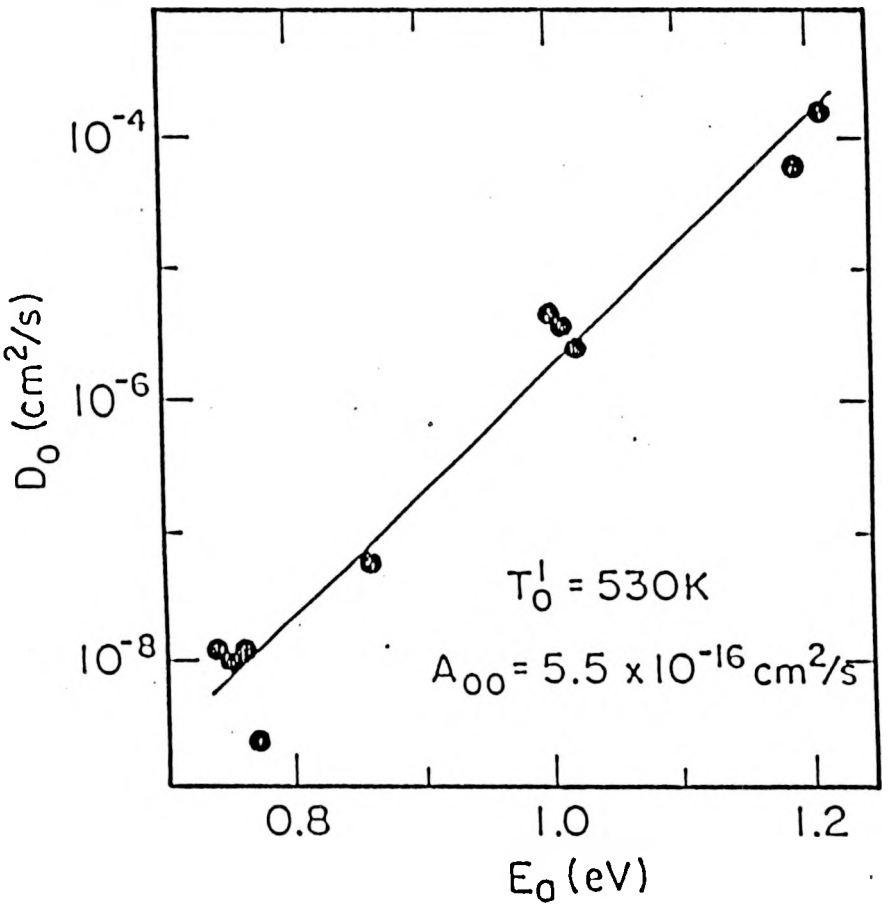

Fig. 5.5 The Meyer-Neldel relation between the activation energy E_a for diffusion at constant diffusion length and the prefactor D_o

Yet the value of T_o' resulting from Fig. 5.2 is significantly lower than any of the values calculated from eq. 1.3 and listed in Table 5.1. As discussed in similar cases in a-Si:H,[86] while microvoids which trap H and D contribute to the value of α, and consequently T_o, they would have little effect on E_a and D_o (for constant L) and the resulting T_o'. The difference between the values of T_o listed in Table 5.1 and T_o' is another manifestation of the inapplicability of the MT model to a-Ge:H.

Eqs. 1.2-1.4, 4.10, 4.11 and 4.14 also indicate that the value of D_{oo} calculated from the results and eq. 1.2 would equal the prefactor A_{oo} in the MNR. The experimental results, however, do not enable the independent determination of D_{oo} and ω. The overall significance of the MNR in this case is thus questionable, and may result from the nature of the Arrhenius relation and the limited measurement range.[91] The value of T_o' $\approx$ 530 K, which is roughly the average measurement temperature, supports this suspicion.

The results on two other films, 5 and 6, are also noteworthy. Their initial Ge-bonded H-content was 3.1 and 3.6 at.%, respectively. Although C_H decreased during annealing (to 0.9 at.% in sample 5 after 2 hrs at 310°C) no smearing of the deuterium profiles was observed. This behavior is in sharp contrast to rf sputtered a-Si:H of low (~2 at.%) C_{Ho},[86] where no decrease in the H content was observed up to 400°C,

the SIMS profiles demonstrated bulk diffusion at T ≥ 330°C, and α essentially vanished at T ≥ 360°C. It is believed that in these a-Ge:H films, hydrogen diffuses to the nearest microvoid surface, and recombines at that surface to form molecular H_2. If the microvoid is isolated, the molecule will remain trapped in it; if it is connected, the molecule will probably escape from the film. This scenario then implies that the microvoid content in a-Ge:H of low C_{Ho} is considerably higher than in a-Si:H of similar content. An alternative picture involving molecular recombination in the bulk of the film appears highly improbable. Such a process would result in a decreasing mean free path for molecular recombination with increasing C_H. The SIMS profiles in all annealed a-Ge:H should then remain sharp.

The striking results are: Among samples 1, 2, and 3, (i) $\alpha \simeq 0.38 \pm 0.08$ is independent of T (from 180°C to 310°C), C_{Ho} (from 5.0 to 7.4 at.%), and C_H (from ~ 3 - 6 at.%); (ii) E_a is lower than in a-Si:H and decreases with increasing C_H. (iii) Sample 4, suspected to contain a considerably higher microvoid content, yielded a significantly higher value of α ($\simeq 0.65$). (iv) Other samples, of low C_{Ho}, exhibited hydrogen desorption even as the deuterium SIMS profiles remained as sharp as in the unannealed film. (v) A Meyer-Neldel relation (MNR; eqs. 4.11, 4.14, and Fig. 5.5) similar to that found in a-Si:H[86,106] was observed , but with lower values of T_o' and A_{oo}. Yet it is

observed only among different samples, and not as a function of the diffusion distance L in any given sample. Since the value of T_o' is approximately equal to the average measurement temperature, the relation is suspected to be insignificant in this system.

As mentioned above, the results of similar studies in the a-Si:H,[63,86,106] indicated the presence of two major H sites: (i) Bulk monohydride Si-bonded sites and (ii) monohydride sites on (either large or compact) microvoid surfaces. Hydrogen in dihydride and trihydride configurations is well known to recombine to molecular H_2 and evolve rapidly (< 1 hr) from the film at ~300 °C.[106] The bulk monohydride sites are suspected to be distributed in a roughly exponential distribution, with energies in the range of 1.3 - 2.2 eV, qualitatively describable by the MT model.[86] The mono-H sites on microvoid surfaces, on the other hand, are believed to be deeper, essentially rendering the H atoms immobile below ~ 360 °C and perhaps up to ~ 475 °C. This picture accounts for the microvoid-induced suppression of the long-range H diffusion in a-Si:H. An additional important observation, however, is that the total Si-bonded H content remains unchanged (beyond the initial annealing step, which releases the hydrogen in dihydride configuration) during annealing above ~ 275 °C.[63,86] It therefore appears that the monohydride H atoms at the microvoid surfaces do not recombine to form molecular H_2 below

~ 360 °C, and the cross section for this recombination remains small up to ~ 475 °C. In contrast to a-Si:H, the deuterium SIMS profiles of a-Ge:H initially containing 3.6 at.% Ge-bonded H or less remains sharp, but C_H decreases during annealing, to, e.g., 0.9 at.% after 2 hrs at 310 °C It is therefore believed that a-Ge:H of low C_{Ho} has a considerably higher microvoid content than a-Si:H of similar C_{Ho}; as in a-Si:H, H in bulk sites diffusing to the nearest microvoid cannot reenter the bulk. It can, however, desorb out. The details of the desorption process are not clear. We speculate that it may involve recombination of a surface Ge-bonded H atom and an interstitial H arriving from the bulk. In addition, neighboring Ge-bonded H atoms on the surface may also recombine. The latter mechanism is believed to be essentially absent in a-Si:H.[63] The barrier for desorption, regardless of its nature, appears to be significantly shallower than in a-Si:H.

As mention above, the absence of any observed long-range motion in films initially containing 3.1 and 3.6 at.% hydrogen essentially rules out a process involving molecular recombination in the bulk of the film. Since the rate of encounters between H atoms in the bulk should obviously increase with their content, such a process should result in sharp SIMS profiles in all of the annealed a-Ge:H films studied in this work.

The behavior of α may now be addressed in relation to microvoids and the multiple trapping (MT) model. Table 5.1 clearly shows that among sample 1, 2, and 3, $\alpha \simeq 0.38 \pm 0.08$ is independent of C_{Ho}, C_H and T in the ranges mentioned above. Its value, though, is considerably higher in sample 4, which exhibitted the greatest initial reduction in H content, from ~9.5 at.% to less than 5.0 at.%. This initial desorption is probably due primarily to hydrogen from dihydride and trihydride configurations, usually associated with microvoids. It is thus suspected that sample 4 also had the highest microvoid content. The conclusion that α is largely determined by the microvoid content is then in excellent agreement with the numerous reports on a-Si:H.[63,86,95,97,106] In a-Si:H of low C_{Ho} (~ 2 at.%),[86,106] however, α strongly decreased with increasing temperature. It was therefore concluded that in that system, α was also determined by MT among bulk sites roughly exponentially distributed in energy. Yet no such dependence of α on T has been observed in any a-Ge:H. We therefore suspect that the MT model is less relevant to a-Ge:H than to a-Si:H.

As noted above, E_a decreases with increasing C_{Ho} or C_H among samples 1, 2, and 3. Since α is essentially equal in these samples, and independent of temperature, it is believed that the microvoid content is also similar among these films. We therefore suspect that the decreasing E_a reflects some

distribution of activation energies among bulk sites. This distribution, though, is suspected to be quite different from an exponential: The latter would result in a strong temperature dependent α and a MNR between $E_a(L)$ and $D_o(L)$.

VI. THE PERCOLATION MODEL

As we have discussed, amorphous systems are very complicated due to the metastable nature of the samples resulting from the preparation processes. Thus, more than one mechanism may exist to govern the physical processes. In the following, we briefly discuss the transport phenomena in disordered systems from a geometric point of view. A possible explanation for our anomalous diffusion is percolation theory, since percolation and fractal lattices have proven to be reasonable models for disordered systems in many cases. We have carried out computer simulations and obtained preliminary results on this subject. Because the limitation on the sizes of the lattice, more averaging time is needed to make the calculation statistically convincing. In the following we briefly discuss the model in a qualitatively manner, based on well established results.

Evidence exists that amorphous films have structures which have self-similar characteristics.[111] The origin of this morphology is suggested to be the natural clustering which occurs due to the random process of ballistic aggregation.[112] It has been noted that sputter-deposited films could exhibit large-scale structure which affect the physical properties of the film when prepared under low mobility condition. In the "coarsening" stage, the surface

morphology is characterized by columns separated by grooves. As the film thickness increases with time, the basic characteristic features of the surface morphology are retained but the typical length scale of the columns, $\xi(t)$, increases with time. Roy and Messier[113] found that for the rf deposition of SiC films under various conditions, $\xi(t) \sim t^p$, with $p \approx 0.73$. C. Tang et al.[111] have calculated p for a range of random and self-similar starting surface, and found that p indeed reaches a universal value 3/4.

Computer simulations have been carried out for transport phenomena, and in particular, particle diffusion. Using random walk theory in uniform Euclidean systems, the mean-square displacement of a random walker, $\langle R^2(t) \rangle$, is proportional to the time t, $\langle R^2(t) \rangle \propto t$. This is just Fick's law, since the diffusion constant $D \propto \langle R^2(t) \rangle / t$. However, in disordered systems, this law is not valid in general. Rather, the diffusion law becomes anomalous:[114,115]

$$\langle R^2(t) \rangle \sim t^{2/d_w} \qquad 6.1$$

with $d_w > 2$.

The percolation model is closer to the systems we studied. For simplicity, instead of the more probable diamond structure, we describe the site percolation model on a square lattice. A fraction p of the sites are randomly occupied and

a fraction 1 - p are empty. Nearest-neighbour occupied sites form connected clusters, which may relate to the formation of micvoids. When p increases, the average size of the clusters increases. There exists a critical concentration p_c = 0.593[116] below which only finite clusters exist and above which a large ('infinite') cluster is formed. Obviously, below and above p_c, the size of the clusters is different, and the physical phenomena involved may have distinctive natures. For instance, the bulk conductivity σ approaches zero as p decreases below the percolation threshold. The diffusivity D is related to σ as $D = \sigma(kT/ne^2)$ where n is the charge density, and hence will approach zero as well. The percolation transition at p_c is described by the probability P_∞ that a site in the lattice belongs to the infinite cluster. Above p_c, P_∞ increases with p as[117]

$$P_\infty \sim (p - p_c)^{\mu}, \qquad 6.2$$

whereas below p_c, $P_\infty = 0$. The diameter of the clusters below p_c is characterized by the correlation length ξ, which is defined as the mean distance between two sites belonging to the same cluster. When p approaches p_c, ξ diverges as

$$\xi \sim (p_c - p)^{-\nu}. \qquad 6.3$$

The exponents μ and ν are universal constants and depend only on dimensionality.

Since the probability of being on clusters with sizes that are equal to or greater than ξ behaves as $|p - p_c|^{\mu}$, both above and below p_c, further calculations give the following relations for the diffusion constants:[117]

(a) for $p > p_c$ and $R(t) \geq \xi$, $D \sim (p - p_c)^{\kappa-\mu}$; 6.4

(b) for $p < p_c$ and $t \rightarrow \infty$, $D \sim t^{-1} |p - p_c|^{-2\nu}$; and 6.5

(c) for $R(t) \leq \xi$, $D \sim t^{2/dw-1}$. 6.6

where κ is a constant.

There are three characteristic regimes for diffusion on percolation clusters. For $p > p_c$ the infinite cluster is homogeneous, and diffusion is regular. For $p < p_c$, the largest clusters are typically of a finite linear size $\xi(p)$, and

$\langle R^2(t) \rangle \sim \xi^2(p)$ when t tends to infinity, and the diffusion is suppressed. Anomalous diffusion takes place if $\langle R^2(t) \rangle \ll \xi^2(p)$, $D \sim t^{2/dw-1}$, with $d_w > 2$.

Clearly, percolation theory offers an explanation to the dispersive diffusion. Also, the value of $\langle R^2(t) \rangle$ decrerases with the decreasing p because the random walker has less sites

to walk on. Thus diffusion becomes slower in the low concentration network than in the ones with higher concentration. Comparing this result with the experiments, we may think that the time-dependent diffusion is due to the disordered percolating nature of the network. As the concentration of the sites becomes smaller and smaller, diffusion slows down and even ceases. Obviously, if trapping is considered in the percolation model, the diffusion behavior will become more complicated.[118] If we think that the microvoids act as trapping centers, a sufficient percentage of them may eventually suppress the particle motion.

Several questions remain unanswered. There are obviously at least two subnetworks, one for Si (Ge), and the other for H. This is reminiscent of the "hydrogen glass" model, where mobile bonded hydrogen can be considered to form a disordered matrix distinct from the amorphous silicon subnetwork.[61,119] From a geometric point of view, this factor basically does not change the dispersive diffusion behavior. But if the energy difference between the two subnetworks is considered, the outcome may be different. Another issue is the value of the percolation threshold p_c for the systems. Is there still a distinctive value of p_c in spite of the numerous configrations of the amorphous structures ? This is an important question since p_c is higher than the percentage of hydrogen in the samples. For the diamond structure, p_c is equal to 0.428 for

site percolation and 0.388 for bond percolation.[120] Another issue is the effect of the interaction between the particles on p_c. It is possible that due to the complexity of the network in structure as well as in the interaction between particles, the percolation threshold for these amorphous systems is no longer universal. The threshold for the amorphous structures may become "smeared" and vary with preparation conditions. Diffusion becomes slower below this "smeared" threshold and hence results in a time-dependent behavior. Also, in the amorphous case, H motion (hopping) will not be limited to the equal distance. All these factors need to be considered for the overall influence and behavior. Nevertheless, initial encouraging results warrant further investigations of the applicability of percolation theory to atomic transport in these disordered networks.

VII. SUMMARY

Long-range H motion and desorption in low hydrogen concentration undoped hydrogenated amorphous silicon (a-Si:H) and germanium (a-Ge:H) was studied by secondary ion mass spectrometry (SIMS) and IR absorption. SIMS monitors the deuterium depth profiles and, as a function of annealing, yields information on H motion, while IR determines the hydrogen density and bonding configuration. The dispersive diffusion is studied for varying H content C_H, diffusion length L, and microvoid content at temperatures $T \leq 400$ °C for a-Si:H and $T \leq 310$ °C for a-Ge:H, respectively. A power-law time-dependent diffusion constant $D(t) = D_{oo}(\omega t)^{-\alpha}$ was observed in both systems.

In a-Si:H, α generally deviates from the $1 - T/T_o$ dependence on the temperature T expected from the multiple trapping model. The "apparent" activation energy E_a and prefactor D_o, defined by the linear best-fit of $\ln D(t_L)$ vs $1/T$, strongly increase with L at low C_H. The Meyer-Neldel relation $D_o = A_{oo}\exp(E_a/T_o')$, where $A_{oo} \simeq 3.1\times10^{-14}$ cm^2/s and $T_o' \simeq 730$ K, holds for all $1.3 \leq E_a \leq 2.4$ eV and $2.5\times10^{-5} \leq D_o \leq 3100$ cm^2/s. At low C_H, the motion is suspected to be dominated by thermally activated detrapping out of sites distributed in energy, comparable to an exponential distribution of width $T_o' \simeq 730$ K. This is suspected from the behavior of α which is

generally a nonincreasing function of the temperature, and the strongly inhibited diffusion in films of low H content. Structural relaxation, defect generation, and deep sites associated with both large and compact microvoid surfaces are also suspected to affect hydrogen motion and consequently the value of α.

In a-Ge:H, α is essentially temperature independent, but decreases with decreasing H content. It is believed that as in a-Si:H, α is largely determined by the microvoid content. The role of bulk multiple trapping sites, though, is suspected to be less significant than in a-Si:H. The gradual decrease in C_H during annealing above 180 °C, not observed in a-Si:H, is believed to result from diffusion to the nearest microvoid surface and recombination to molecular H_2 at the surface. This phenomenon is particularly striking in low C_{Ho} samples, since the deuterium SIMS profiles remained sharp during annealing, which is in agreement with the observations of Beyer et al..[107] Since this behavior sharply contrasts that of a-Si:H of low C_{Ho}, it is suspected that the microvoid content of such a-Ge:H is significantly higher than in a-Si:H of similar C_{Ho}. The activation energy E_a ranges from 0.7 to 1.2 eV among the various films. The Meyer-Neldel relation is observed, with $A_{oo} \simeq 5.5 \times 10^{-16}$ cm^2/s and $T_o' \simeq 530$ K. These values are lower than the corresponging values in a-Si:H.

From the results of a-Si:H and a-Ge:H, it is evident that

microvoids play an important role in hydrogen motion. The mono Si-H bond sites on microvoid surfaces are apprantly deep H-trapping sites in a-Si:H. However, H desorbs from mono Ge-H bonds on microvoid surfaces in a-Ge:H at temperatures as low as 180 °C. Also evident is that hydrogen trapping sites are not simply distributed exponentially in energy. As the microvoid content increases, the deviation from the exponential distribution increases. The dispersive parameter α seems more sensitive to the microvoid content rather than to temperature.

We may have to accept the fact that more than one mechanism may be operating due to the system complexity. Therefore, more than one model may be needed to explain the experimental observations. One possible model is that of percolation, which shows that the diffusion on percolating clusters is anomalous.

REFERENCES

1. W. E. Spear and P. G. LeComber, Solid State Commun. **17**, 1193 (1975).

2. N. F. Mott, Phil. Mag. **19**, 835 (1969).

3. A. I. Gubanov, Sov. Phys. Solid State **3**, 1694 (1962).

4. D. E. Carlson and C. R. Wronski, Appl. Phys. Lett. **28**, 671 (1976).

5. H. Okamoto, Y. Nitta, T. Yamaguchi and Y. Hamakawa, Sol. Energy Mater., **2**, 313 (1980).

6. S. Tsuda, N. Nakamura, Y. Nakashima, H. Tarui and Y. Kuwano, Jpn. J. Appl. Phys., **21** (Suppl. 22) 251 (1982).

7. K. Nozawa, Y. Yamaguchi, J. Hanna, and I. Shimizu, J. of Non-Cryst. Solids **59&60**, 533 (1983).

8. A. H. Mahan, D. L. Williamson, and A. Madan, Appl. Phys. Lett. **44**, 220 (1984).

9. W. Paul, D. K. Paul, B. von Roedern, J. Blake, and S. Oguz, Phys. Rev. Lett. **46**, 1016 (1981).

10. A. Morimoto, T. Miura, M. Kumeda, and T. Shimizu, Jpn. J. Appl. Phys. **20**, **L** 833 (1981).

11. B. von Roedern, D. K. Paul, J. Blake, R. W. Collins, G. Moddel, and W. Paul, Phys. Rev. B **25**, 7678 (1982).

12. K. Tsuji and S. Minomura, J. Phys. **42**, C4-233 (1981).

13. A. J. Leadbetter, A. A. M. Rashid, R. M. Richardson, A. F. Wright and J. C. Knights, Solid State Commun. **33**, 973 (1980).

14. J. C. Knights, Jpn. Appl. Phys. **18**, (Suppl. 1) 101 (1979).

15. G. Lucovsky, R. J. Nemanich and J. C. Knights, Phys. Rev. B **19**, 2064 (1979).

16. J. A. Reimer, J. Phys. **42**, C4-715 (1981).

17. T. Ishidate, K. Inoue, K. Tsuji ans S. Minomura, Solid State Commun. **42**, 197 (1982).

18. T. Shimizu, K. Nakazawa, M. Kumeda and S. Ueda, Physica **117B/118B**, 926 (1983).

19. S. C. Moss and J. F. Graczky, Phys. Rev. Lett. **23**, 1167 (1969).

20. R. J. Temkin, W. Paul, and G. A. N. Connell, Adv. Phys. **22**, 581 (1973).

21. D. E. Polk, J. Non. Cryst. Solids **5**, 365 (1971).

22. N. F. Mott, and E. A. Davis, Electronic Processes in Non Crystalline Materials, (Clarendon Press, Oxford, 1979).

23. N. F. Mott, Electrons in Disordered System, Adv. Phy. **26**, 49 (1967).

24. J. D. Joannopoulos and G. Lucovsky, eds., The Physics of Hydrogenated Amorphous SIlicon, Vol. II (Springer-Verlag, New York, 1984).

25. D. Adler, Phys. Rev. Lett. **41**, 1755 (1978).

26. D. C. Allen and J. D. Joanopolous, Phys. Rev. Lett. **44**, 43, (1980).

27. D. K. Biegelsen and M. Stutzmann, Phys. Rev. B **33** 1880 (1986).

28. Y. Bar-Yam and J. D. Joannopoulos, J. Electron. Mater. **14**, 261 (1985).

29. S. T. Pantelides, Phys. Rev. Lett. **57**, 2979 (1986).

30. S. T. Pantelides, Phys. Rev. Lett. **58**, 1344 (1987).

31. M. Stutzmann and D. K. Biegelsen, Phys. Rev. Lett. **60**, 1682 (1988).

32. J. H. Stathis and S. T. Pantelides, Phys. Rev. B **37**, 6579 (1988).

33. H. Yokomichi, I. Hirabayashi, and K. Morigaki, Solid State Commun. **61**, 697 (1987).

34. M. Stutzmann and D. K. Biegelsen, Phys. Rev. B **40**, 9834 (1989).

35. P. A. Fedders, and A. E. Carlson, Phys. Rev. B **37**, 8506 (1988).

36. N. Ishii and T. Shimizu, Jpn. J. Appl. Phys. Pt. 2 **27**, L1800 (1988).

37. R. Biswas, Gary S. Grest, and C. M. Soukoulis, Phys. Rev. B **36**, 7437 (1987).

38. S. T. Pantelides, Phys. Rev. B **36**, 3479 (1987).

39. P.C. Kelires and J. Tersoff, Phys. Rev. Lett **61**, 562, (1988).

40. J. R. Pawlik and W. Paul, Proc. of the 7th Int. Conf. on Amorphous and Liquid Semiconductors, Edinburg 1977, P. 334.

41. T. D. Moustakas, D. A. Anderson, and W. Paul, Solid State Commun. **23**, 155 (1977).

42. G. D. Cody, T. Tiedje, B. Abeles, B. Brooks, and Y. Goldstein, Phys. Rev. Rev. **47**, 1480 (1981).

43. R. E. Viturro, and K. Weiser, Philos. Mag. **53**, 93 (1986).

44. D. L. Staebler and C. R. Wronski, Appl. Phys. Lett. **31**, 292 (1977).

45. J. Pankove and J. E. Berkeyheiser, Appl. Phys. Lett. **37**, 705 (1980).

46. H. Dersch, J. Stuke, and J. Beichler, Appl. Phys. Lett. **38**, 456 (1981).

47. M. Stutzmann, W. B. Jackson, and C. C. Tsai, Appl. Phys. Lett. **45**, 1075 (1984).

48. J. D. Cohen, D. V. Lang, J. P. Harbison, and A. M. Sergent, Sol. Cells, **9**, 119 (1983).

49. N. M. Amer, A. Skumanich, and J. B. Jackson, Physica B&C **117-118 B+C**, pt.2 897 (1983).

50. D. L. Staebler , R. S. Crandall and R. Williams, Appl. Phys. Lett. **39**, 733 (1981).

51. M. Stutzmann, D. K. Biegelsen, and R. A. Street, Phys. Rev. B. **35**, 5666, (1987).

52. R. Street, D. K. Biegelsen and J. Stuke, Philos. Mag. B **40**, 451 (1979).

53. W. M. Pontuschka, W. E. Carlos, P. C. Taylor and R. W. Griffith, Phys. Rev. B. **25**, 4362 (1985).

54. R. A. Street, Phys. Rev. Lett. **49**, 1187 (1982).

55. S. Guha, J. Yang, W. Czubatyj, S. J. Hudgens and M. Hack, Appl. Phys. Lett, **42**, 588 (1983).

56. G. Nakamura, K. Sato, and Y. Yukimoto, Solar Cells **9**, 75 (1983).

57. D. Adler, J Phys. (Paris) **42**, C4-3 (1981).

58. D. Adler, Solar Cells **9**, 133 (1983).

59. M. Stutzmann, W. B. Jackson and C. C. Tsai, Phys. Rev. B **32**, 23 (1985).

60. W. B. Jackson, in Proceedings of the Korea Science and Engineering Foundation/U.S. National Science Foundation Joint Seminar: The Physics of Semiconductor Material and Applications, edited by C. Lee and W. Paul (Korea Science and Engineering, Seoul, 1987), p. 47.

61. R. A. Street, C. C. Tsai, J. Kakalios, and W. B. Jackson, Phil.Mag. B **56**, 305 (1987).

62. J. Kakalios, R. A. Street, and W. B. Jackson, Phys. Rev. Lett. **59**, 1037 (1987).

63. J. Shinar, R. Shinar, S. Mitra, and J. Y. Kim, Phys. Rev. Lett. **62**, 2001 (1989).

64. W. B. Jackson, Phys. Rev. B **38**, 3595 (1988).

65. W. B. Jackson, Phys. Rev. B **41**, 1059 (1990).

66. W. B. Jackson and M. D. Moyer, Phys. Rev. B **36**, 6217, (1987).

67. W. E. Spear and P. G. LeComber, in The physics of Hydrogenated Amorphous Silicon I, edited by J. D. Joannopouslos and G. Lucovsky (Springer-Verlag, NY, 1984), Chap. 3.

68. D. J. Leopold, P. A. Fedders, R. E. Norberg, J. B. Boyce and J. C. Knights, Phys. Rev. B **31**, 5642 (1985).

69. D. A. Anderson, G. Moddel, M. A. Paesler, and W. Paul, J. Vac. Sci. Technol. **16**, 902 (1979).

70. H. S. Wu, Ph.D. Dissertation, Iowa State University, (1988).

71. T. D. Moustakas, J. Electronic Mat. **8**, 391 (1979).

72. T. D. Moustakas, T. Tiedje, and W. A. Lanford, in Tetrahedrally Bonded Amorphous Semiconductors, edited by R. A. Street, D. K. Biegelson, and K. C. Knights, AIP Conference Proceedings **73**, 20 (1981).

73. M. H. Brodsky, D. Kaplan, and J. F. Ziegler, Appl. Phys. Lett. **21**, 305 (1972).

74. M. Albers, Ph.D. Dissertation, Iowa State University, (1987).

75. J. Tauc, R. Grigorovicci, and A. Vancu, in Amorphous and Liquid Semiconductors, edited by J. Tauc (Plenum, New York, 1974).

76. F. Urbach, Phys. Rev. **92**, 1324 (1953).

77. R. A. Street, J. C. Knights and D. K. Biegelson, Phys. Rev. B **18**, 1880 (1978).

78. C. P. Poole, Jr., in Electron Spin Resonance, 2nd Ed. (John Wiley & Sons, New York, 1983), p. 409.

79. C. P. Poole, Jr., in Electron Spin Resonance, 2dn Ed. (John Wiley & Sons, New York, 1983), p. 406.

80. M. H. Brodsky, C. Cardona, and J. J. Cuomo, Phys. Rev. B, **16**, 3556, (1977).

81. H. R. Shanks, C. J. Fang, L. Ley, M. Cardona, F. J. Demond, and S. Kablitzer, Phys. Status Solidi (b), **100**, 43 (1980).

82. Y. Catherine and G. Turban, Thin Solid Films, **70**, 101 (1980).

83. C. J. Fang, K. J. Gruntz, L. Ley, M. Cardona, F. J. Demond, G. Muller, and S. Kalbitzer, J. Non-Cryst. Solids **35 & 36**, 255 (1980).

84. M. Cardona, Phys. Status Solidi (b) **118**, 463 (1983).

85. A. H. Mahan, D. L. Williamson, B. P. Nelson, and R. S. Crandall, Phys. Rev. B **40**, 12024 (1989).

86. J. Shinar, R. Shinar, X.-L. Wu, S. Mitra, and R. F. Girvan, Phys. Rev. B **43**, 1631 (1991).

87. H. Wagner and W. Beyer, Solid State Commun. **48**, 585 (1983).

88. G. Lucovsky, S. S. Chao, J. Yang, J. E. Tyler, R.C. Ross, and W. Czubatyj, Phys. Rev. B **31**, 2190 (1985).

89. D. G. Welkie, Secondary Ion Mass Spectrometry, SIMS V, A. Benninghoven et al., Eds., Springer, Berlin (1986) page 296.

90. J. Crank, The Mathematics of Diffusion (Clarendon, Oxford, England, 1975), Chap.2.

91. R. Kirchheim and X. Y. Huang, Phys. Status Solidi B **144**, 253 (1987).

92. R. Biswas, I. Kwon, A. M. Bouchard, C. M. Soukoulis, and G. S. Grest, Phys. Rev. B **39**, 5101 (1989).

93. W. B. Jackson, C. C. Tsai, and R. Thompson, Phys. Rev. Lett. **64**, 56 (1990).

94. D. E. Carlson and C. W. Magee, Appl. Phys. Lett. **33**, 81 (1978).

95. S. Mitra, R. Shinar, and J. Shinar, Phys. Rev. B **42**, 6746 (1990).

96. S. Roorda, S. Doorn, W. C. Sinke, P. M. L. O. Scholte and E. van Loenen, Phys. Rev. Lett. **62**, 1880 (1989).

97. X.-M. Tang, J. Weber, Y. Baer, and F. Finger, Phys. Rev. B **41**, 7945 (1990).

98. J. C. Dyre, J. Phys. C **19**, 5655 (1986).

99. X.-M. Tang, J. Weber, Y. Baer, and F. Finger, Solid State Commun **74**, 174 (1990).

100. X.-M. Tang, J. Weber, Y. Baer, and F. Finger, Phys. Rev. B **42**, 7277 (1990).

101. H. Fritzsche and X.-M. Deng, Bull. Am. Phys, Soc. **35**, 349 (1990); X.-M. Deng (unpublished).

102. W.-L. Shao, J. Shinar, B. C. Gerstein, F. Li, and J. S. Lannin, Phys. Rev. B **41**, 9491 (1990).

103. M. A. Petrich, K. K. Gleason, and J. A. Reimer, Phys. Rev. B **36**, 9722 (1987); J. A. Reimer and M. A. Petrich, in Amorphous Silicon and Related Materials, Edited by H. Fritzsche (World Scientific, Singapore, 1988), p. 3, and reference therein.

104. M. Zhang, E. J. VanderHeiden, P. C. Taylor, R. Shinar, S. Mitra, and J. Shinar, Amorphous Silicon Technology - 1990, (Mater. Res. Soc. Symp. Proc. **192**, 657 (1990).)

105. W. Beyer, in Tetrahedrally Bonded Amorphous Semiconductors, edited by D. Adler and H. Fritzsche (Plenum Press, New York, 1985), p. 129.

106. R. Shinar, X.-L. Wu, S. Mitra, and J. Shinar, in Amorphous Silicon Technology - 1990, edited by P. C. Taylor, Y. Hamakawa, M. J. Thompson, A. Madan, and P. G. LeComber (Mat. Res. Soc. Symp. Proc. **192**, MAt. Res. Soc., Pittsburgh, PA, 1990), p. 677.

107. W. Beyer, J. Herion, H. Wagner, and U. Zastrow, in Amorphous Silicon Technology - 1990, edited by P. C. Taylor, Y. Hamakawa, M. J. Thompson, A. Madan, and P. G. LeComber (MAt. Res. Soc. Symp. Proc. **192**, Mat. Res. Soc., Pittsburgh, PA, 1990), p. 689.

108. X.-L. Wu, R. Shinar, and J. Shinar, Phys. Rev. B, accepted for publication.

109. M. J. Thompson, in The physics of Hydrogenated Amorphous Silicon, edited by J. D. Joannopoulos and G. Lucovsky, Springer-Verlag, New York, 1984, Chap. 4, and reference therein; M. L. Albers, J. Shinar, and H. R. Shanks, J. Appl. Phys. **64**, 1859 (1988), and references therein.

110. S. Mitra, Ph.D. Dissertation, Iowa State University, (1991).

111. C. Tang, S. Alexander, and R. Bruinsma, Phys. Rev. Lett. **64**, 772 (1990).

112. R. Messier and J. E. Yehoda, J. Appl. Phys. **58**, 3739 (1985).

113. R. A. Roy and R. Messier, Mat. Res. Soc. Symp. Proc. **38**, 363 (1985).

114. I. Webman, Phys. Rev. Lett. **47**, 1497 (1981).

115. Y. Green, A. Aharony, and S. Alexander, Phys. Rev. Lett. **50**, 77 (1983).

116. R. M. Ziff and B. Sapoval, J. Phys. A, **19**, L1169 (1987).

117. S. Havlin and D. Ben-Avraham, Adv. Phys. **36**, 696 (1987).

118. R. B. Pandey, Phys. Rev. B **30**, 489 (1984).

119. R. A. Street, J. Kakalios, and T. M. Hayes, Phys. Rev. B. **34**, 3030, (1986).

120. D. Stauffer, Phys. Reports **54**, 1 (1979).

ACKNOWLEDGMENTS

I would like to thank my research adviser, Dr. Joseph Shinar, for his guidance, encouragement, and support throughout this work.

My full appreciation goes to Dr. Ruth Shinar, for her collaborative work on SIMS and Auger analyses, as well as the valuable advice and discussion on matters related to this thesis.

I appreciate the friendship of Ms. Debra Peterson and family, Ms. Margaret Stanley and Prof. Dennis Wendell, who made life, especially holidays in Ames, enjoyable.

Finally, I would like to thank my parents for their support and encouragement through my school years. I am deeply indebted to my wife, Wendi Wang, for her patience, love and understanding through the years. Her persistent pursuing of academic excellence often inspires me in my research work. I also thank my daughter Victoria Dee, who brought so much joy and happiness to our life.

I also thank the physics department and Ames laboratory for making the facilities available. Ames laboratory is operated for the US Department of Energy by Iowa State University under contract no. W-7405-eng-82. This work was supported by the Director for Energy Research, Office of Basic Energy Science.